

Dissertation
submitted to the
Combined Faculties for the Natural Sciences and for Mathematics
of the Ruperto-Carola University of Heidelberg, Germany
for the degree of
Doctor of Natural Sciences

presented by

Diplom-Physicist: Andreas Van Overberghe
born in: Heidelberg, Germany
Oral examination: 01. February 2006

High Flux Neutron Imaging for highly dynamic and time resolved non-destructive testing

Referees: Prof. Dr. Hartmut Abele
Prof. Dr. Josef Bille

Zusammenfassung

Im Rahmen der hier beschriebenen Arbeit wurde eine Anlage für Neutronenradiographie und -tomographie, NEUTROGRAPH, am INSTITUT LAUE-LANGEVIN (ILL) weiterentwickelt, Experimente durchgeführt und neue Mess- und Auswertungsmethoden entwickelt. Die Besonderheit von NEUTROGRAPH ist seine konkurrenzlose Intensität bei gleichzeitig moderater Kollimation. Diese Eigenschaften ermöglichen es, dynamische Prozesse mit einer exzellenten zeitlichen Auflösung zu untersuchen und dicke und stark absorbierende Materialien zu durchdringen. Ganz neue Anwendungsbereiche aus Wissenschaft und Ingenieurwesen konnten dabei erschlossen werden. Zu nennen sind Untersuchungen an Wärmetauschern und Motoren, Flugzeugbauteilen, Fossilien und historischem Kulturgut.

Abstract

This thesis describes the development of a facility for neutron radiography and tomography, NEUTROGRAPH, at the INSTITUT LAUE-LANGEVIN (ILL), the carrying out of experiments and the development of new measurement and evaluation methods. The special feature of NEUTROGRAPH is its outstanding intensity together with a moderate collimation. These properties allow the investigation of dynamic processes with an excellent time resolution and the transmittance through strongly absorbing and bulky materials. A totally new spectrum of scientific and engineering applications could be developed. Among the experiments are investigations of heat exchangers and combustion engines, parts from aircrafts, fossils and historical heritage.

Contents

Contents	iii
List of Figures	vii
1 Introduction	1
2 Neutron Imaging - Overview	3
2.1 Principle of Neutron Imaging	3
2.1.1 Radiography	3
2.1.2 Tomography	6
2.2 Neutron Imaging Complementing X-ray Techniques	7
3 The ILL - Tomography Station Neutrograph	9
3.1 The H9 - Beam Line	10
3.2 Beam Properties	12
3.2.1 Diameter and Profile	13
3.2.2 Flux	14
3.2.3 Divergence	15
3.2.4 Energy Spectrum	19
3.3 Casemate	19
3.3.1 Sample Environment	20
3.3.2 Collimators	23
3.3.3 Radiation Protection	23
3.3.4 Safety Installations	25
3.4 Detector System	26
3.4.1 Scintillator	27
3.4.2 Camera	28

3.4.3	Detector Housing and Optics	29
4	Data Evaluation	31
4.1	Image Normalization	31
4.2	Statistical and Readout Errors	31
4.3	Systematic Errors	33
4.3.1	Scintillator Degradation	33
4.3.2	Correction of Scintillator Degradation	36
4.3.3	Intensity Fluctuations	40
4.3.4	Camera Fluctuations	41
5	Measuring Techniques	45
5.1	Dynamic Radiography	45
5.2	Stroboscopic Radiography (Periodic Processes)	46
5.3	Dynamic Tomography	46
5.3.1	Principle	46
5.3.2	Application in Two-Phase Flows	47
5.3.3	Further Improvements	52
6	Experiment Highlights	53
6.1	Combustion Processes	53
6.1.1	First Calculations	54
6.1.2	Injector Nozzle	56
6.1.3	Petrol Engine	61
6.1.4	Diesel Engine	66
6.1.5	Contrast agents	71
6.1.6	Why was the fuel not detected?	73
6.1.7	Conclusion	75
6.2	Dynamic Radiography - More Experiments	77
6.2.1	Car engine	77
6.2.2	Minichannel Heat Exchanger	79
6.2.3	$^3\text{He}/^4\text{He}$ phase transition	83
6.3	Static Tomography - More Experiments	84
6.3.1	Antarctic Fossils	84

7 Conclusion and Outlook	87
Bibliography	I
Acknowledgements	V
Declaration	VII

List of Figures

2.1	Parallel beam.	4
2.2	Fan beam: distortions due to the sample thickness	4
2.3	Cone beam: distortions due to the sample thickness	4
2.4	Principle of tomography.	7
2.5	Attenuation cross section as a function of mass. (source [Gild03])	8
3.1	Top-ranking neutron imaging facilities: The diagram shows the capture flux as a function of the beam collimation. For cold neutrons, the real flux is up to a factor 3 smaller. The curved lines represent constant values of the neutron flux per solid angle. [ANLW], [NEUTRA], [HMI], [Antares]	10
3.2	Overview over ILL beam lines: This figure depicts "level C" of the reactor and the neighboring guide halls. The yellow circle in the middle represents the reactor core, surrounded by the heavy water tank, which contains also the cold (blue) and hot (red) sources. The beam tubes and neutron guides distribute the neutrons to the instruments inside the reactor hall (big circle) and the guide halls.	11
3.3	Set-up of NEUTROGRAPH at H9.	12
3.4	Beam Profile	13
3.5	Gold foil measurement 2002: 16 gold foils are positioned all over the beam profile (left) and irradiated for 10 min. The neutron flux is calculated from the gamma ray intensity of the decay (right).	15
3.6	Gold foil measurement 2005: 17 gold foils are positioned all over the beam profile and the results combined with an image of the profile.	16
3.7	Comparison of the results from the gold foil activation and a radiographic image acquired with a scintillator-CCD system. The results are in good agreement. . .	16
3.8	Beam divergence	17
3.9	Pinhole camera: Each small image is at the position where it was recorded. The images of the source are displayed as seen by the detector, which means they are rotated by 180 degrees (camera obscura).	18

3.10	Pinhole camera: Magnification of the image in the yellow box. The image is rotated by 180°	18
3.11	New casemate: The casemate has been extended in length by 800 mm and in height by 400 mm. (Drawing I. Sutton, Bureau d'Etudes, ILL)	21
3.12	Draft of the primary shutter system with projected revolver: The revolver contains an empty beam tube for normal operation, one beam tube containing the collimators and a third beam tube for future installations. (Drawing F. Fihman, Bureau d'Etudes, ILL)	24
4.1	Several scintillator samples	34
4.2	Scintillator degradation	35
4.3	fit of decay curve	35
4.4	fit of decay curve	37
4.5	Friction stir weld: left: Normalized image without correction. right: Normalized image after 5 iterations.	39
4.6	Transmission values extracted from one row	39
4.7	Fluctuations of beam intensity	40
4.8	Stability of beam profile	41
4.9	Intensity fluctuations in dark images: the displayed values are mean values of the whole chip	42
4.10	Intensity fluctuations in dark images	43
4.11	Intensity fluctuations in dark images	43
5.1	Set-up of experiment on dynamic tomography: A bundle of small aluminum tubes with a two-phase flow of water and air running through it.	48
5.2	Tomography with stepwise rotation: 40 sec acquisition time, 180 projections. . .	49
5.3	Tomography with stepwise rotation: 40 sec acquisition time, 180 projections. . .	50
5.4	Tomography with continuous rotation: 9 sec acquisition time, 180 projections. .	50
5.5	Tomography with continuous rotation: 9 sec acquisition time, 180 projections. .	51
6.1	Common Rail Diesel Injector	56
6.2	Experimental Set-Up	57
6.3	Diesel injection at 6 different time steps: The grey values are rescaled to a small band of about 1.5%	59
6.4	Diesel injection at 4 different time steps	61
6.5	Power generator with carburetor engine	63

6.6	Radiographs of carburetor engine at different time steps [ms]: 0 ms : ignition, 5-10 ms : expansion, 15-20 ms : ejection, 25-30 ms : refilling, 35-0 ms : compression	64
6.7	The grey values in the white boxes were integrated and compared	65
6.8	Integrated grey values from the boxes shown in Fig. 6.7	65
6.9	Power generator with diesel engine	67
6.10	Radiographs of diesel engine at different time steps:	67
6.11	Modified set-up:	69
6.12	Image normalization	69
6.13	Variances of grey values along a line (graph from [Eng04])	71
6.14	left : image acquired at the beginning of the experiment. right : image from the end of the experiment	72
6.15	Sediments inside the combustion chamber	72
6.16	BMW car engine: The engine was driven externally by an electric motor with 1000 rpm.	77
6.17	BMW car engine: The engine was driven externally by an electric motor with 1000 rpm.	78
6.18	Flow apparatus	80
6.19	Temperature variations for the center thermocouple at various flow rates: a) $1.5\text{ kg/m}^2\text{ s}$ - superheated gas with intermittent liquid slugs; b) $6.0\text{ kg/m}^2\text{ s}$ - saturated boiling with intermittent liquid superheat; c) $15.4\text{ kg/m}^2\text{ s}$ - liquid superheat with intermittent boiling; d) $21.4\text{ kg/m}^2\text{ s}$ - both liquid superheat and saturated boiling.	81
6.20	Images from the instants marked with circles in Fig. 6.19b: slow fill followed by rapid vaporization.	82
6.21	Images corresponding to the square in Fig. 6.19d: steady boiling.	82
6.22	Capillaries in a cryostat	83
6.23	Fossil of a monkey-puzzle tree inside a rock sample	85
6.24	Branch of a contemporary monkey-puzzle tree	85

1. Introduction

NEUTROGRAPH is a neutron radiography and tomography facility at the Institut Laue-Langevin (ILL) in Grenoble. It features the most intense beam of thermal neutrons in world that has at the same time a large cross section of $220 \times 220 \text{ mm}^2$ and a good maximum collimation of $L/D \approx 150$. With these properties NEUTROGRAPH is leading in the domain of time resolution and is specialized on:

- High-speed or realtime radiography with a time resolution of 1 ms and frame rates of $f_{realized} = 154 \text{ Hz}$ and $f_{projected} = 1000 \text{ Hz}$.
- Highly time resolving stroboscopic radiography of periodic processes. Very weak attenuation signals can be visualized with a time resolution of $100 \mu\text{s}$.
- Dynamic tomography of processes on a seconds time scale.
- High contrast tomography of strongly attenuating samples.

In order to position NEUTROGRAPH also in the domain of spatial resolution among the top-ranking instruments, the installation of an optional set of soller collimators with a projected divergence of $L/D = 660$ is in preparation. The instrument properties and the properties of the neutron's interaction with matter makes NEUTROGRAPH a powerful tool for nondestructive testing in the following fields of research:

- automotive industry: injection nozzles, combustion engines
- energy engineering: two-phase flows and boiling liquids in channel systems (fuel cells, heat exchanger)
- construction industry and geology: liquid diffusion in porous media
- materials sciences: welds, material defects
- archaeology: fossils, artifacts and cultural assets

In the framework of this thesis, NEUTROGRAPH was put into operation and the instrument properties were investigated. The detection system, the sample environment and the instrument infrastructure were continuously improved in order to optimize the experiment results and to make the work on the experiments more flexible. New measurement procedures and a correction algorithm for the degradation of the detector were developed.

Chapter 2 gives a short introduction to the basics of neutron imaging techniques and a comparison with X-ray methods. Chapter 3 describes the instrument properties and features. The measurement errors are analyzed in chapter 4 and a new algorithm for the correction of the scintillator degradation is presented. In chapter 5 the measuring methods are outlined and in chapter 6 we present some experiment highlights.

2. Neutron Imaging - Overview

This chapter is meant to give a short introduction to the basics of neutron imaging techniques. The basic concept and formulas are presented and the difference to X-ray techniques described. More details can be found elsewhere [Schill99], [Schneid01], [Her80], [Ferg03], [Gild03].

2.1 Principle of Neutron Imaging

2.1.1 Radiography

Neutron radiography and tomography work in the same way as X-ray imaging techniques but exploit a neutron beam instead. Neutrons are transmitted through a sample and detected by a two-dimensional position sensitive detector, which is orientated perpendicular to the beam axis. This detector acquires a grey level image, representing the neutron transmittance through the sample.

A couple of beam geometries with different advantages and disadvantages can be used. Normally the geometry is determined by the nature of the beam source. With neutrons normally a parallel beam is used (Fig. 2.1). This geometry maps the object 1:1 onto the detector. Distortions are virtually absent.

X-ray sources produce either a fan beam (Fig. 2.2) or a cone beam (Fig. 2.3). In the case of a fan beam the object must be scanned perpendicular to the plane which contains the fan beam. This is a big disadvantage, because dynamic processes which are on the same time scale as the time needed for the scanning can not be investigated.

A cone beam has the same ability of imaging a sample onto a two-dimensional detector as a parallel beam it has. It's geometry can be exploited to magnify the image by choosing appropriate distances from the source to the sample and from the sample to the detector. In this way the effective resolution can even exceed the detector resolution. But it implies also the disadvantage of distortions in three-dimensional objects. Since the magnification depends on the ratio of the distances, planes perpendicular to the beam axis seem to be larger the closer they are to the source (Fig. 2.3).

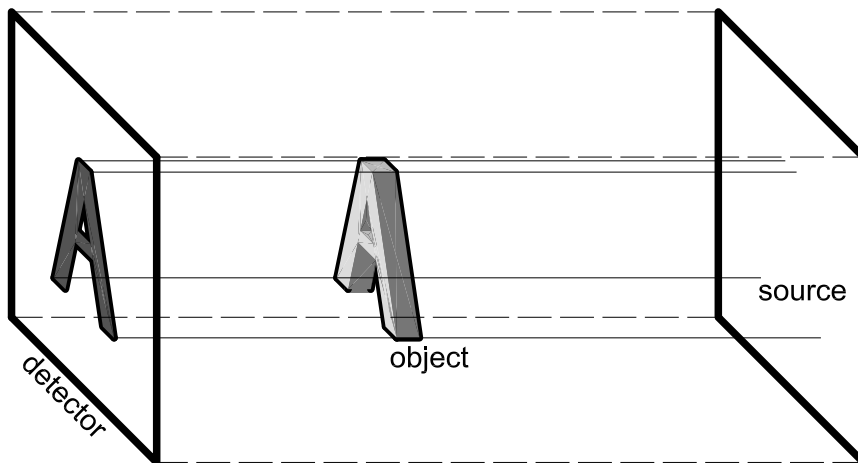


Figure 2.1: *Parallel beam.*

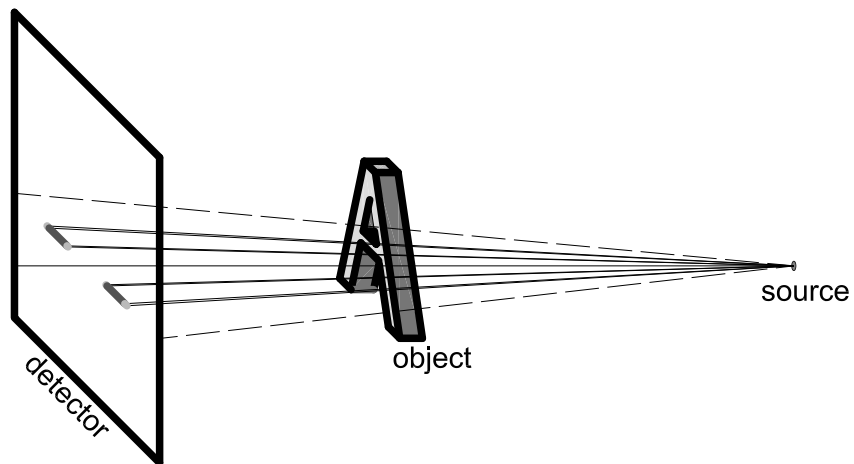


Figure 2.2: *Fan beam: distortions due to the sample thickness*

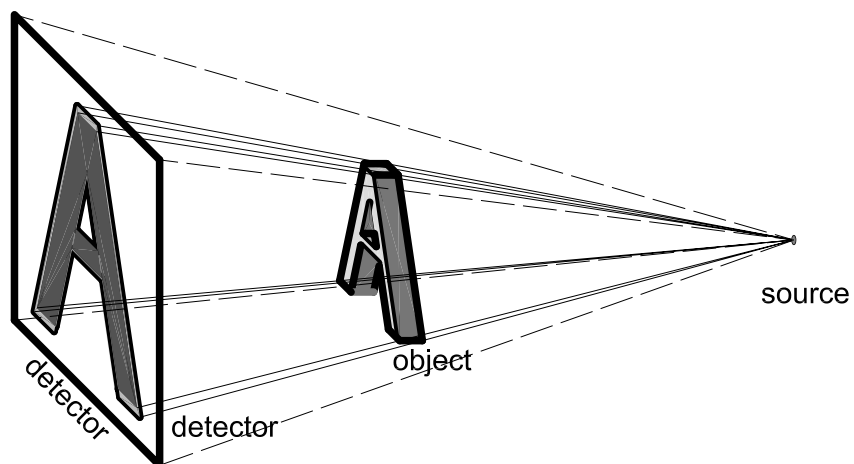


Figure 2.3: *Cone beam: distortions due to the sample thickness*

As mentioned above, the recorded image represents the transmittance through the sample which corresponds to a map of beam attenuation integrated along the paths through the object, if the incident beam intensity is known. The attenuation is due to the interaction of the incident rays with matter. Since the properties of the interaction with matter differ extremely for neutrons and X-rays, both methods provide complementing information (chapter 2.2).

Carrying no electrical charge, neutrons interact predominantly with the nuclei by strong interaction. The interaction of the neutron's magnetic dipole with matter could be used to investigate magnetic structures. The tensorial nature of this interaction makes a three-dimensional investigation very complex and could be the subject of an other thesis. However, in standard applications the magnetic dipole can be neglected and will not be regarded in this thesis. The strong interaction leads to both absorption of the neutron in a nucleus and to scattering. While absorption leads to a real attenuation of the beam, scattering is only a deflection of the neutrons flight path. A scattered neutron can hit the detector at any other position and result in a certain background, which can be neglected in many cases. At a given position on the detector, the beam attenuation is described by

$$I = I_0 \exp\left(-\int_S \mu(\vec{x}) ds\right) \quad (2.1)$$

with I_0 and I as incident and transmitted beam intensities, S the path of transmittance through the sample and $\mu(\vec{x})$ the local attenuation coefficient, which is a material property. This coefficient is given by

$$\mu(\vec{x}) = \sigma_t \frac{\rho(\vec{x}) N_A}{M_{mol}} \quad \text{or} \quad \mu(\vec{x}) = \sum_i \sigma_{t,i} \frac{\rho_i(\vec{x}) N_A}{M_{mol,i}} \quad (2.2)$$

respectively, if the sample material is a composition of several elements. σ_t is the material's total cross section for neutrons, ρ it's density, N_A the Avogadro's number and M_{mol} the molar mass. The total cross section σ_t is the combination of the scattering cross section σ_s and the absorption cross section σ_a :

$$\sigma_t = \sigma_s + k_n \sigma_a \quad (2.3)$$

The factor k_n depends on the neutron energy and equals one for thermal neutrons. In (2.3) the scattering, which includes both coherent and incoherent scattering, is considered to be independent from the neutron energy, which is not totally true. Especially for neutrons with wavelengths larger than the Bragg cutoff the scattering cross section drops for many materials. However, for thermal and fast neutrons it can be considered to be constant. As the neutron

radiography station described in this thesis exploits a thermal neutron beam, energy dependence of the scattering cross section will not be regarded.

The absorption cross section depends on the energy over the whole spectrum. For cold and thermal energies, the behavior of the factor k_n can be approximated for most materials by the relation

$$k_n = \frac{v_0}{v}, \quad (2.4)$$

where v is the neutron's velocity and $v_0 = 2200 \text{ m s}^{-1}$ [Hug57]. For epithermal and fast neutrons the behavior does not follow such a simple law. Especially at resonances the absorption cross section varies by several orders of magnitude for only a sharp energy band. e.g. resonances of Gadolinium and Cadmium lie in the thermal spectrum and makes them good absorbers.

The energy dependence of the attenuation cross section can be exploited to distinguish between different materials and to increase contrast. Radiographs can be taken at different energies and then be compared. This method is very effective around Bragg cutoffs and resonances.

2.1.2 Tomography

Tomography is the extension of radiography from two dimensions to three. It always follows the same principle: radiographs are acquired from many different directions and a three-dimensional data set is reconstructed from this. There are several acquisition methods. In medicine a small source-detector system rotates around the fixed patient. In neutron tomography or at large synchrotron radiation facilities the sources can not be moved. They stay at the same place and the sample is rotated instead (Fig. 2.4).

For the reconstruction of a three-dimensional model several algorithms exist, which are described, e.g., in [Her80]. At NEUTROGRAPH we use a filtered back projection. Was the tomography done with a parallel beam geometry, already the raw data can be split up in independent slices perpendicular to the rotational axis according to the single lines of the detector. This is very helpful for parallel computation of many slices or for a quick preview of only one slice in order to see, which optional filters in the reconstruction are best suited for the given problem. For most reconstruction algorithms, a rotation of 2π is needed. In the case of a parallel beam a rotation of π is sufficient, because each projection $\varphi + \pi$ is identical to the projection φ except that it is flipped.

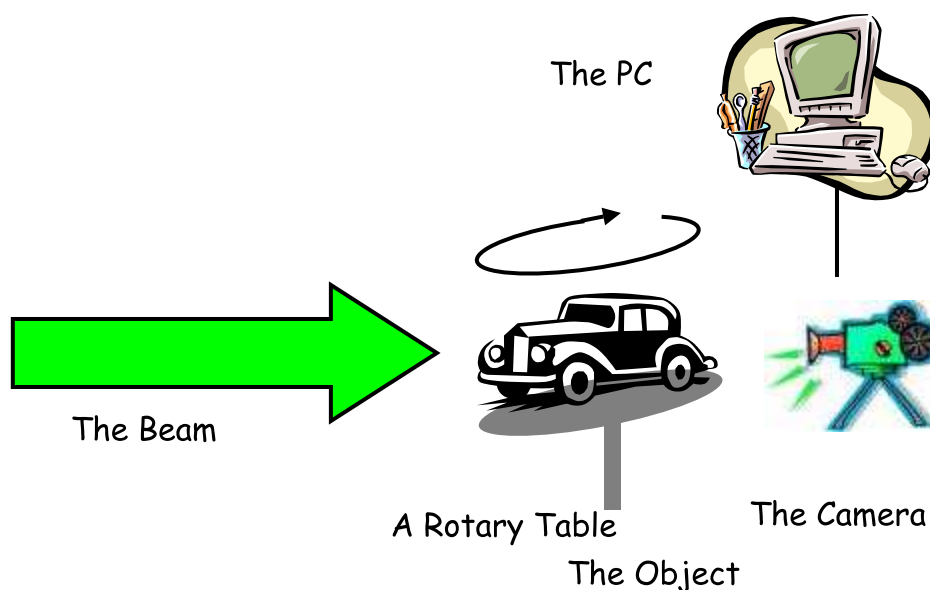


Figure 2.4: Principle of tomography.

2.2 Neutron Imaging Complementing X-ray Techniques

Compared to X-ray radiography, neutron imaging is a young discipline and less known. Why should a new technique be introduced while an other already exists and which provides even better spatial resolution? The reason is the different interaction of neutrons and X-rays with matter. X-rays interact electromagnetically with the atom's electrons. The heavier the element the higher the electron number density and with it the absorption. Fig. 2.5 shows the attenuation cross sections for X-rays and neutrons as a function of the mass.

Neutrons instead interact with the nuclei by strong interaction. The cross sections for scattering and absorption depend on the nucleus' structure and may differ even for isotopes of one element by many orders of magnitude. The values depicted in Fig. 2.5 are those from the natural abundance of the isotopes.

For a good differentiation of two elements/isotopes, the cross sections must differ significantly. For X-rays this is only true for elements with a significant difference in mass and not for isotopes. Often neutrons can differentiate even between neighboring elements and isotopes (chapter 6.2.3). Neutrons and X-rays can be applied to totally different applications. They are not competing but complementing each other.

One important field for neutron imaging techniques is the visualization of hydrogen containing compounds in porous metal or stone matrices.

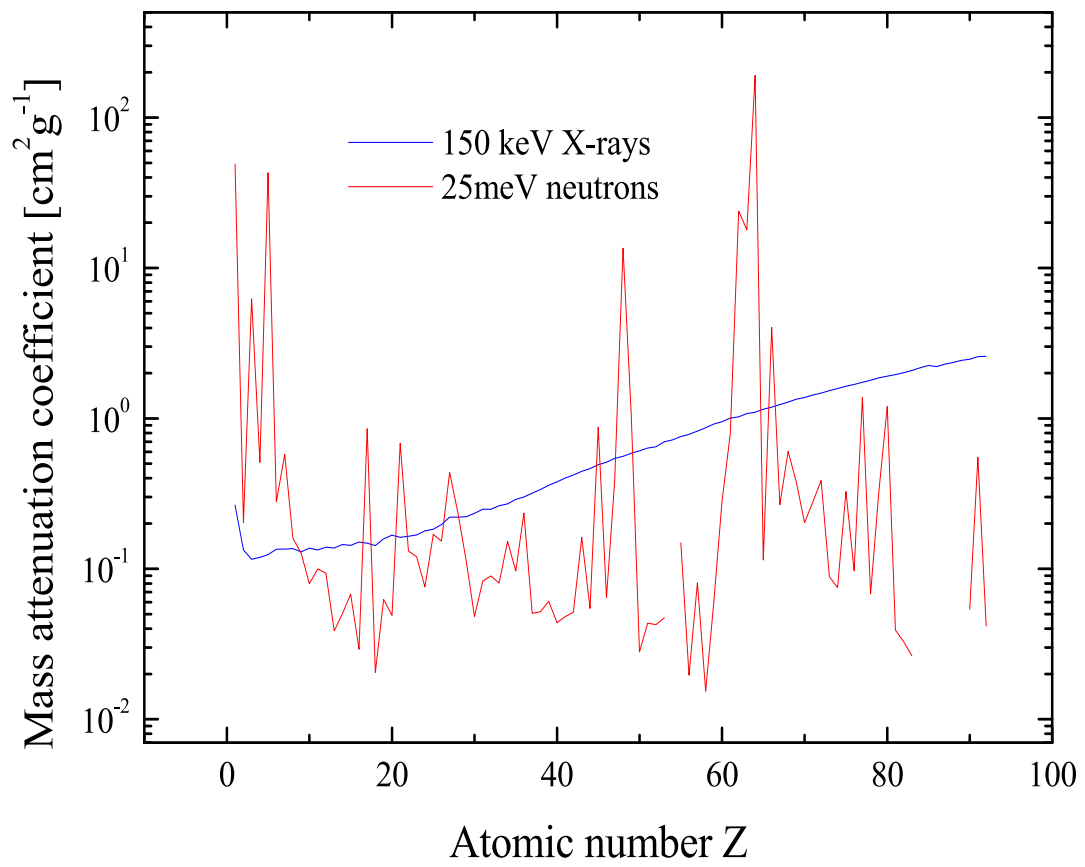


Figure 2.5: Attenuation cross section as a function of mass. (source [Gild03])

3. The ILL - Tomography Station Neutrograph

NEUTROGRAPH is located at the world's most intense thermal neutron beam of large cross section and good collimation. With the high intensity it is dedicated for highly time resolving neutron imaging or the detection of small material variances with high contrast. With the installation of new collimators, which is scheduled for 2006, NEUTROGRAPH can run optionally in high spatial resolution mode.

Fig. 3.1 compares NEUTROGRAPH'S flux and collimation properties with other top-ranking neutron imaging facilities. The curved lines represent constant values for the neutron flux per solid angle and can be interpreted as a measure for the quality of the neutron source. Many facilities vary the combination of flux and collimation by the choice of the diameter of a diaphragm, which is installed far upstream in the beam. All the combinations lie more or less perfectly on such a curve. The instruments at PSI and TUM demonstrate this behavior. For the projected ILL option this is not true, because the higher collimation is realized with soller collimators, where additional flux is lost.

Fig. 3.1 makes also a difference between thermal and cold neutron sources. As the value for the flux is normally the so called capture flux and the cross section for neutron capture in gold increases for cold neutrons, for cold neutrons the real flux is typically by a factor of up to 3 lower than the capture flux.

This chapter deals with all the properties of the neutron beam and the detector system and gives a description of the experimental zone and the sample environment.

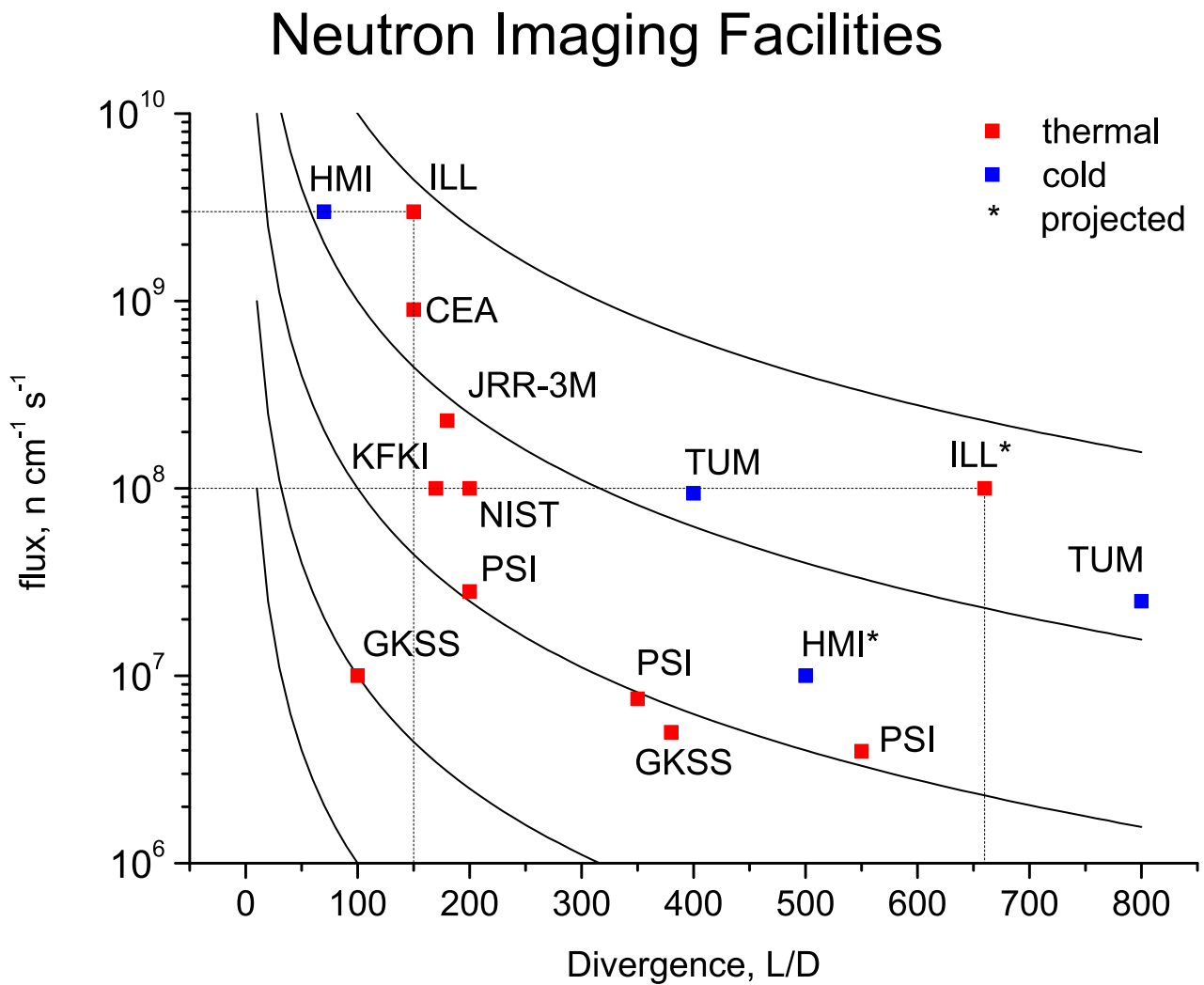


Figure 3.1: Top-ranking neutron imaging facilities: The diagram shows the capture flux as function of the beam collimation. For cold neutrons, the real flux is up to a factor 3 smaller. The curved lines represent constant values of the neutron flux per solid angle. [ANLW], [NEUTRA], [HMI], [Antares]

3.1 The H9 - Beam Line

NEUTROGRAPH is located at the ILL's H9 beam line, the world's most intense thermal neutron beam of large cross section and good collimation. NEUTROGRAPH shares this beam with "Lohengrin", a mass spectrometer for fission products. Fig. 3.2 gives an overview over all beam lines and instruments at the ILL.

The beam line is a simple flight tube, which penetrates the concrete and light water shielding and reaches into the heavy water tank close to the reactor core (Fig. 3.3). Neutrons are scattered and moderated in the heavy water and can be described as a free gas. Those neutrons which are by accident scattered into the right direction, fly inside the tube out of the reactor pool.

For the experiments at Lohengrin, target materials are moved on a cart inside the tube close to the "nose", where the tube begins. Here, where the neutron density is extremely high, the neutrons induce the fission of target nuclei and the electrically charged fission products fly through the tube out of the reactor. Several meters later, these charged particles enter the field of a magnetic dipole, which guides them to the right out of the tubes axis. Directly behind the magnet, a curved plate capacitor bends the particle beam upwards to a germanium detector. This combination of a magnetic and electric field is the classical arrangement of a mass spectrometer and allows also in this case a precise measurement of the mass to charge ratio of the fission products. The magnetic field does not affect the neutrons (the interaction with the magnetic moment can be neglected for imaging purposes) and they fly straight forward. Lohengrin was installed in the first days of ILL and for many years it exploited the H9 beam line alone. During all this time, the high potential neutron beam was not further exploited but was stopped in a beam dump, until the idea of a neutron imaging facility was realized. For this purpose the beam dump was replaced by the huge primary shutter, which can move to the side to give the neutron beam way to enter the experimental zone inside the new secondary casemate. Here the neutrons penetrate the sample and hit the detector behind it.

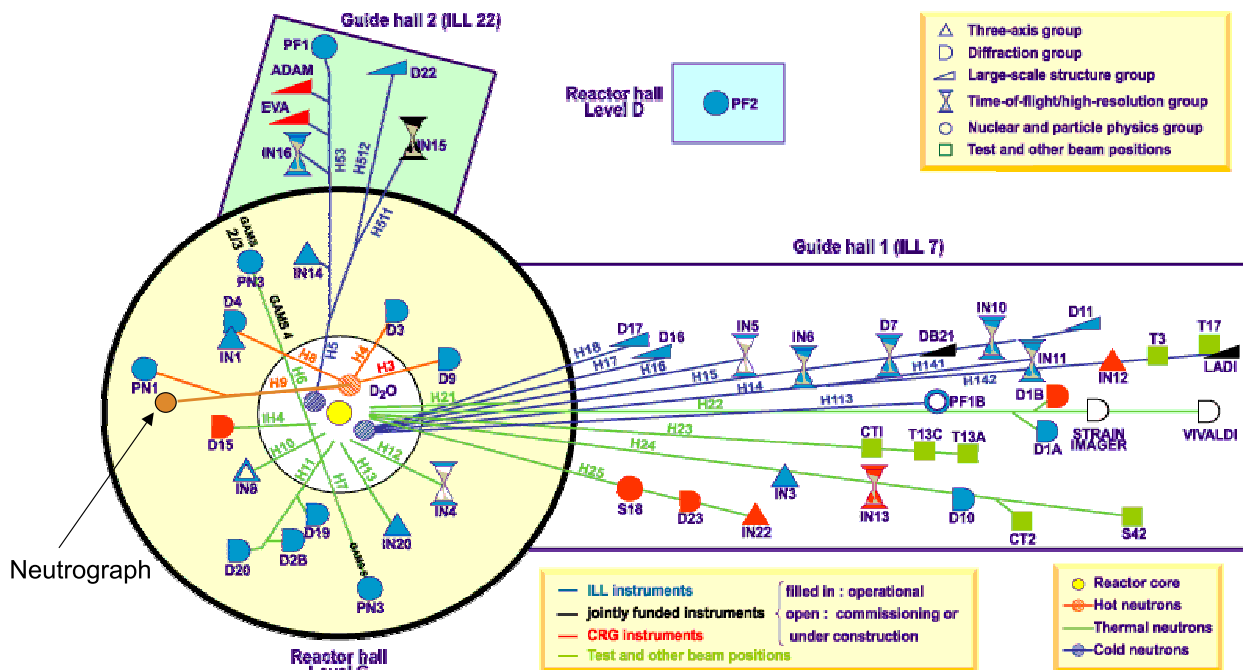


Figure 3.2: Overview over ILL beam lines: This figure depicts "level C" of the reactor and the neighboring guide halls. The yellow circle in the middle represents the reactor core, surrounded by the heavy water tank, which contains also the cold (blue) and hot (red) sources. The beam tubes and neutron guides distribute the neutrons to the instruments inside the reactor hall (big circle) and the guide halls.

Though the beam line is not especially dedicated for neutron imaging and though several installations inside the tube, in particular the target cart, alter the beam, the properties of NEUTROGRAPH are little affected and experiments can run at Lohengrin and the NEUTROGRAPH at the same time. The only thing to ensure is that nothing changes at Lohengrin during one experimental run at the NEUTROGRAPH.

3.2 Beam Properties

Several beam properties are of importance and have to be considered when setting up a neutron imaging facility: divergence, neutron flux, beam diameter and profile and the energy spectrum. The following sections discuss the properties of the H9 beam line, how they were measured and some measures which were taken in order to improve these properties.

During the reactor shutdown in the winter 2004/2005, the beam tube was replaced by a new

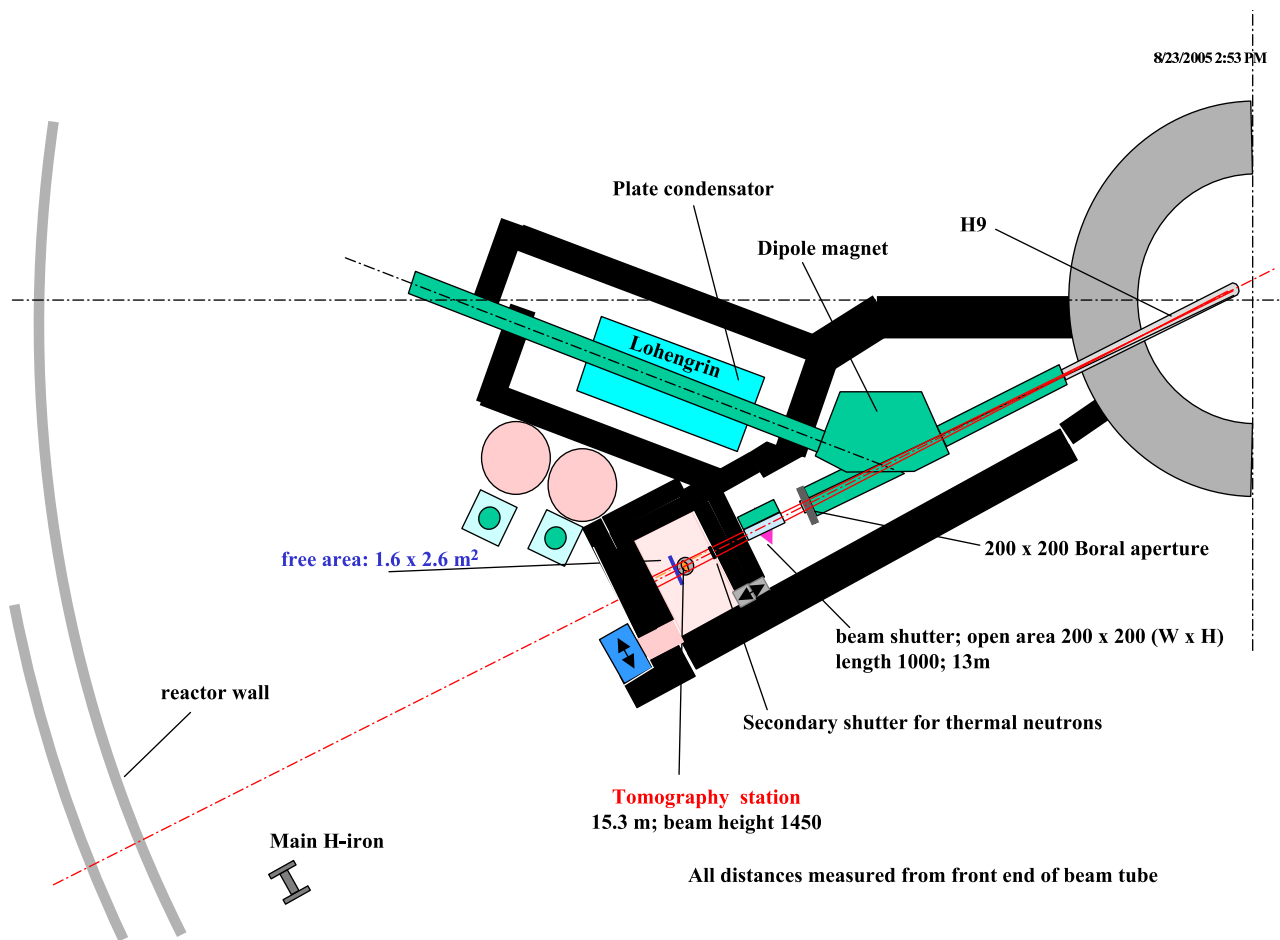


Figure 3.3: Set-up of NEUTROGRAPH at H9.

one to prevent material fatigue. Therefore the measurement of the beam properties from the year 2002 were repeated in 2005. Since the geometry remained the same, only little changes were expected. A comparison of the measurements proof that this is true.

3.2.1 Diameter and Profile

Neutron imaging mostly exploits parallel beams. It is obvious that large diameters are preferable in order to image the sample object at once. If the object is larger than the beam, it can still be scanned by moving the object transversal to the beam. The pictures taken at several positions of the object are recombined later. However, this is possible only with static objects and not for the investigation of dynamic processes. Due to the beam tube's geometry, the neutron beam of NEUTROGRAPH has a cross section of $220 \times 220 \text{ mm}^2$.

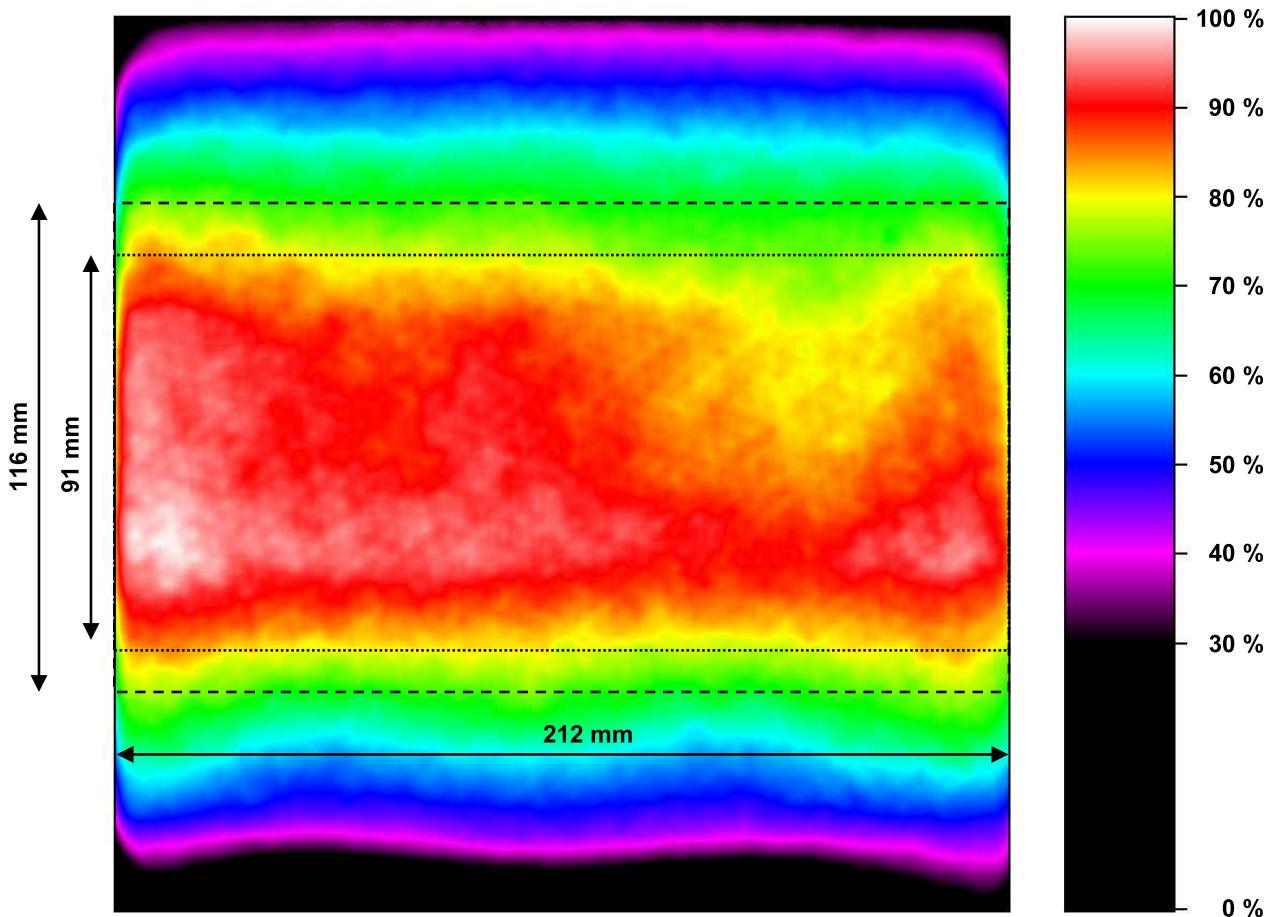


Figure 3.4: *Beam Profile*

The ideal beam profile would be an absolute homogeneous intensity distribution. As such a beam does not exist, the inhomogeneities have to be normalized out. However the inhom-

geneity must not be too large. The exposure time depends on the intensity of the beam and the statistics needed (chapter 4.2). It is always adjusted to the lowest intensity to fulfill the statistics at this point, while it is overfulfilled at the other points. This could easily mean that the detector is saturated at the bright points or, if the exposure time is reduced and several images integrated instead, that the detector works in a non-ideal range at the dark points and further noise is obtained. There is no exact value or threshold which inhomogeneity can be accepted. It depends largely on the application. As a rule of thumb, 20% to 30% of deviation can easily be handled.

Fig. 3.4 shows the beam profile of NEUTROGRAPH. The area with a homogeneity within 20 % measures about $91 \times 212 \text{ mm}^2$, the area of 30 % measures about $116 \times 212 \text{ mm}^2$. The beam profile depends on the position of a collimator, which is installed upstream in front of Lohengrin's dipole magnet. It is meant to shield the magnet against too much activation and influences the beam profile vertically. For every target change at Lohengrin this collimator is opened and reset to its normal position. There is no way to find always exactly the same position. Typically a target change takes place once a week while experiments at NEUTROGRAPH never took longer than a day. As long as the collimator position is constant during one experiment at NEUTROGRAPH, there is no problem connected to it.

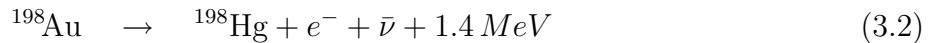
3.2.2 Flux

The neutron flux is essential for the time resolution of the instrument. As in photographic applications, the brightness of the source determines the exposure time. One can express this also in terms of neutron and photon statistics (chapter 4.2).

The beam intensity was measured by the activation of 16 (17 respectively) gold foils. During the irradiation of 8 – 10 *min* the following reaction takes place:



The ^{198}Au nuclei decay with a half life time of about 2.5 days:



From the γ -ray intensity the neutron capture flux was calculated. This technique has a relative error of typically 10 %. The activation depends on the neutrons' energy spectrum. However, since the biggest part of the neutrons is thermal, the measured capture flux can be assumed to be equal to the real flux. Fig. 3.5 shows the geometry and the results from the measurement in the year 2002. The beam profile represented by the light and dark grey areas is a simple

interpolation of the measurement points. In Fig. 3.6 the results from the year 2005 are displayed in combination with a real image of the beam profile. This was useful to find a relation between the beam intensity and the grey values acquired by the camera and to determine the maximum intensity.

Comparing the results from the years 2002 and 2005 we find a loss in beam intensity. In 2002 it was 3.2×10^9 , in 2005 only $2.7 \times 10^9 n cm^{-2} s^{-1}$ were found. It might be equal within the error of 10% or it could be a real effect due to the new beam tube, which was installed in winter 2004/2005. Most likely it is due to the influence of Lohengrin's collimator at the dipole magnet (chapter 3.2.1). It was measured that the position of the collimator does not only influence the beam profile but also the intensity by about 50%.

3.2.3 Divergence

The spatial resolution of an image depends not only on the detector resolution but also strongly on the beam divergence. For neutron imaging mostly parallel beams are exploited. The parallel beam, without any optical device in between, maps an image of the object onto the detector. Any non-parallel part of the beam causes an error in this mapping, it causes a blurring of the image. To gain the maximum spatial resolution, the divergence must be as small as possible.

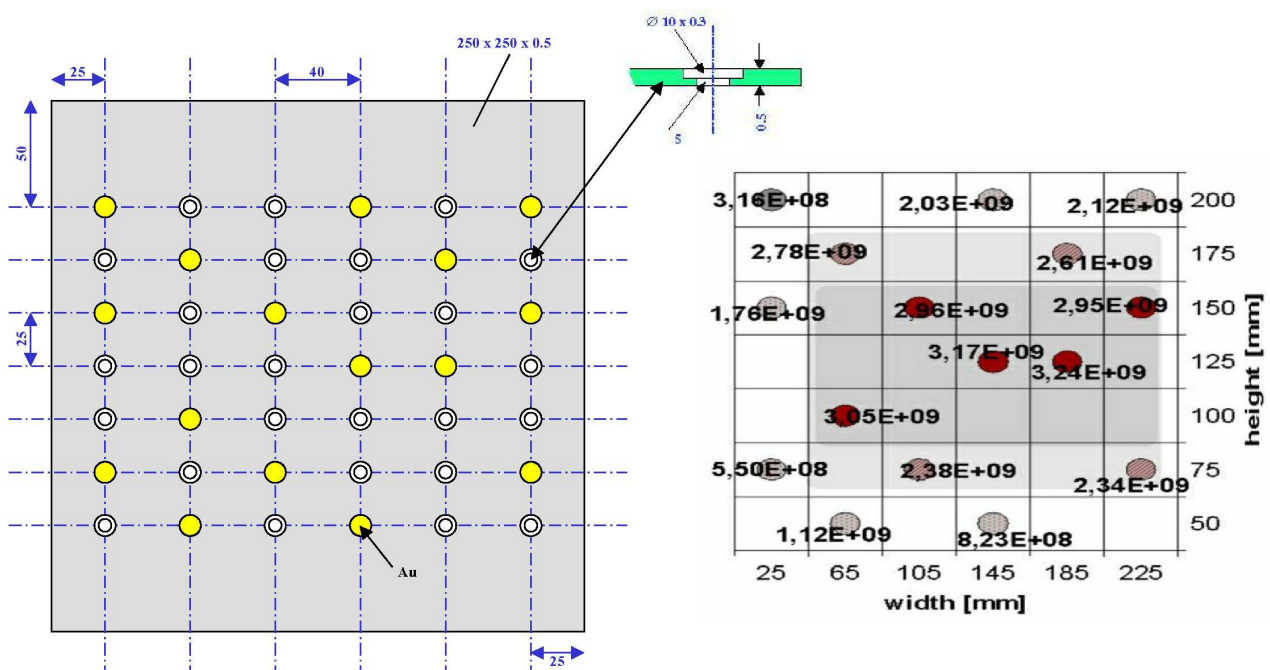


Figure 3.5: Gold foil measurement 2002: 16 gold foils are positioned all over the beam profile (left) and irradiated for 10 min. The neutron flux is calculated from the gamma ray intensity of the decay (right).

3 The ILL - Tomography Station Neutrograph

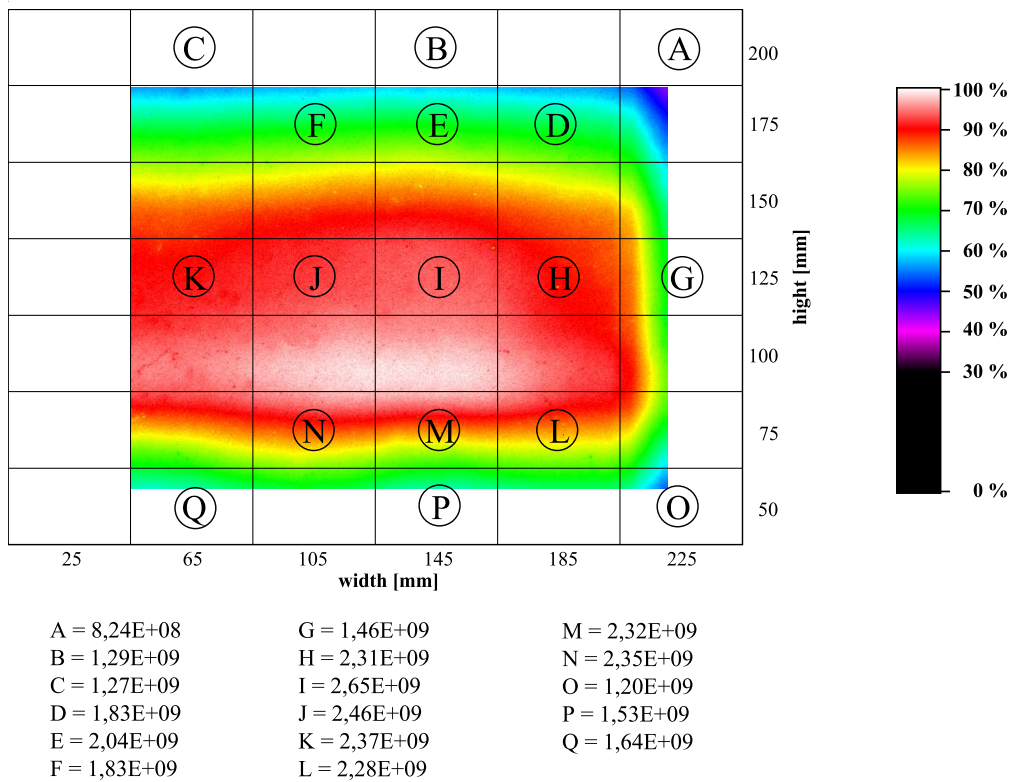


Figure 3.6: Gold foil measurement 2005: 17 gold foils are positioned all over the beam profile and the results combined with an image of the profile.

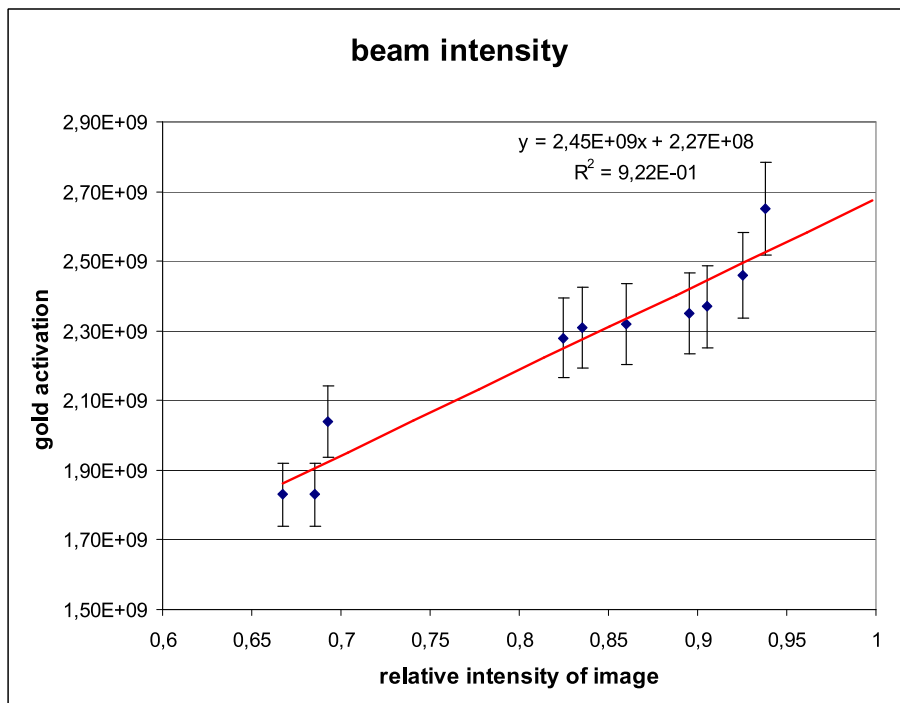


Figure 3.7: Comparison of the results from the gold foil activation and a radiographic image acquired with a scintillator-CCD system. The results are in good agreement.

The most common way to describe the divergence is the ratio L/D (pronounce: l over d). L is the distance between the light or beam source and a sample, D describes the diameter of the source (Fig. 3.8). In the same way L describes the distance between a point like object and the detector whereas D represents the diameter of the blurred image of this point. In this case one uses normally small letters.

In the case of NEUTROGRAPH, the divergence is the result of the the beam tube's geometry only and the devices installed for Lohengrin. Now there are no additional collimators installed since they would cause a drop of beam intensity, but NEUTROGRAPH is dedicated for high intensity neutron imaging. However, we are preparing the installation of optional collimators, to be able to run NEUTROGRAPH in either a high time resolution or a high spatial resolution mode (chapter 3.3.2).

From the geometry of the beam tube, the divergence was initially estimated to be $L/D = 150$. It was measured in 2002 with the Kobayashi method [Kob90] to $L/D_{horiz} = 155$ and $L/D_{vert} = 160$, which corresponds to 6.5 mrad [Ferg03].

In 2005 the measurement was repeated not with the Kobayashi method but by imaging the source with a pinhole camera. A cadmium plate with a small pinhole of about 0.5 mm diameter was installed in front of the detector in a distance of 1780 mm . This set-up produced an image which is rotated by 180° (camera obscura). The pinhole was moved to different positions and the images acquired. Fig. 3.9 shows all the images from the different positions in one image. Fig. 3.10 displays a magnification of the image in the yellow box.

The bright square in the middle is the image of the source. With it's dimension of $12.5 \times 12.5 \text{ mm}^2$ and the distance of 1780 mm in between the pinhole and the detector, one calculates $L/D_{horiz} = L/D_{vert} = 142$ and $L/D_{diagonal} = 101$. The divergence depends on the azimuth angle. Furthermore there are regions on the left and the right which serve as neutron sources of lower intensity. The neutrons originating from these regions do not travel in a direct line

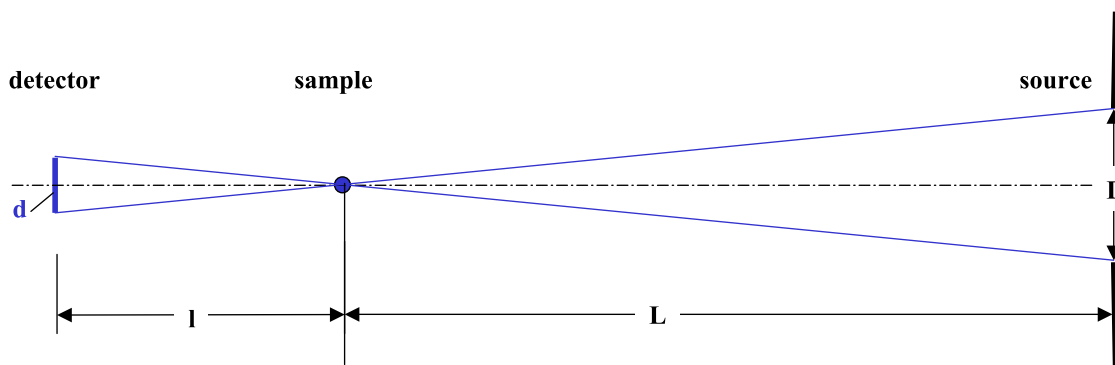


Figure 3.8: *Beam divergence*

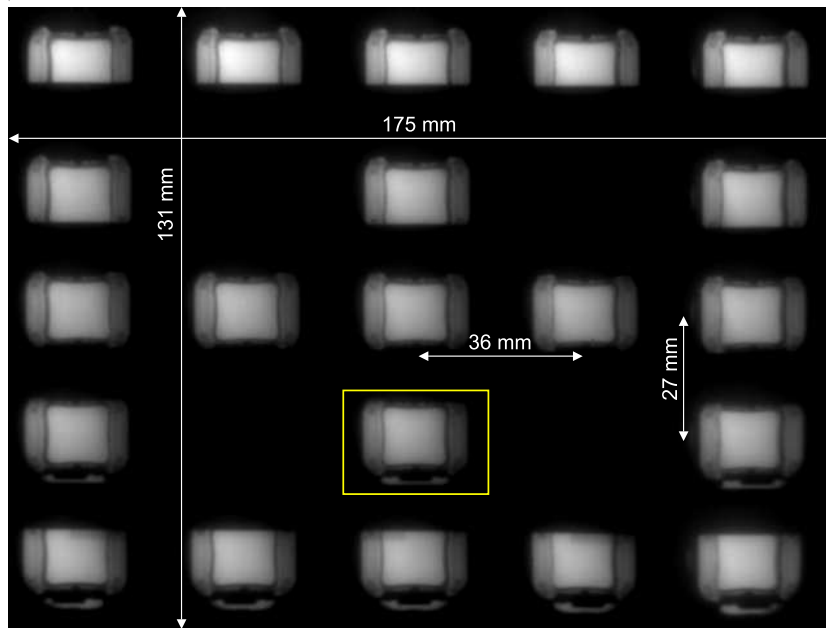


Figure 3.9: Pinhole camera: Each small image is at the position where it was recorded. The images of the source are displayed as seen by the detector, which means they are rotated by 180 degrees (camera obscura).

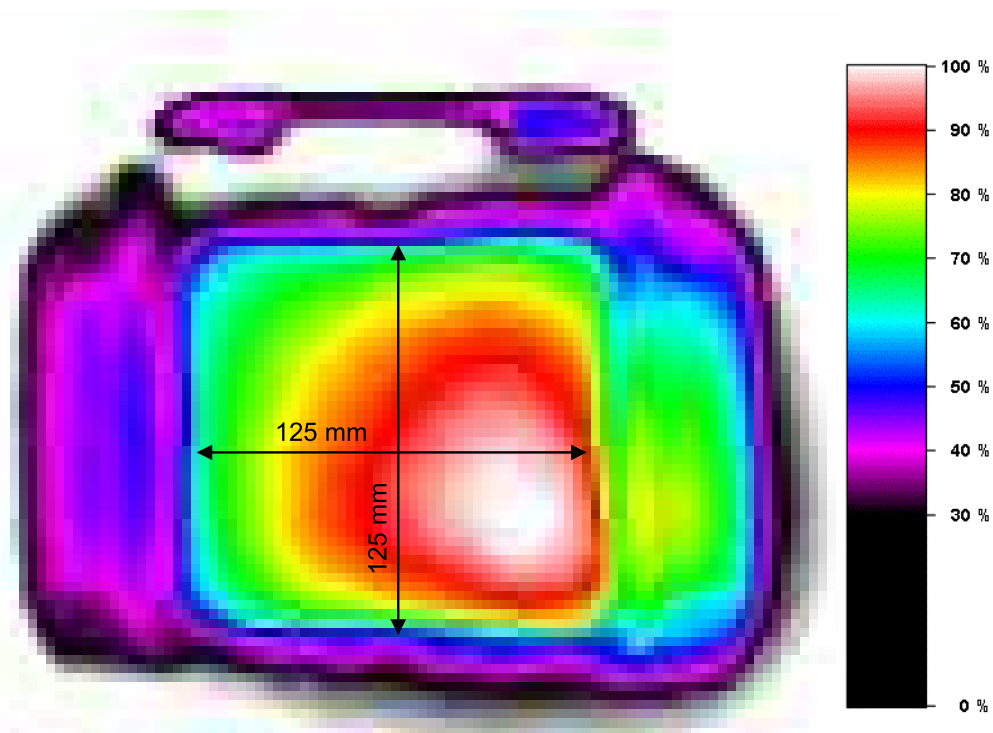


Figure 3.10: Pinhole camera: Magnification of the image in the yellow box. The image is rotated by 180°.

but are scattered at some installations from Lohengrin. Their contribution to the neutron beam increases the horizontal divergence. A further effect can be seen in Fig. 3.9: from outer positions the source is not completely visible which has an influence on the beam divergence. The divergence depends not only on the azimuth angle but also on the position.

If we compare the measurement from 2002 with the considerations on the images from the pinhole camera, the results do not fit together. Even though the beam tube was replaced, the geometry can be assumed to be the same as before. More probably the difference comes from the measuring method itself. In 2002, the measurement was done with a Kobayashi device [Ferg03]. For this method the beam divergence is assumed to be the same at all positions, which is not true.

It is recommended to repeat the measurement with a slightly different method. The base is the Kobayashi method as the standard method in neutron radiography for the determination of beam divergences. But instead of regarding holes of different diameters at different positions, only one single hole should be regarded at different distances between hole and detector. In this case the results originate from only one position and not from many others. This method can be repeated at other positions all over the beam or could be done at many positions at the same time. This would result in a detailed map of local values of the beam divergence.

3.2.4 Energy Spectrum

The precise energy spectrum has not been measured at the sample position of NEUTROGRAPH, however it is fairly known from simulations and spectrum measurements in the reactor pool at the position, where the beam tube extracts the neutrons. Since the tube represents a simple flight path, there is no reason why the energy spectrum should change from the tube's beginning to its end, as it happens inside neutron guides.

The energy spectrum of the H9 beam line is a so called thermalized spectrum, which is typically found in heavy water moderators in a short distance to the reactor core. This spectrum has a broad energy distribution with the maximum corresponding to the temperature of the moderator, in the case of ILL approximately $300K$ and therefore it is thermal. It follows approximately a Maxwell-Boltzmann function, but has a higher contribution from epithermal and fast neutrons. As a rule of thumb, 10% of the neutrons are epithermal and 1% are fast neutrons.

3.3 Casemate

The casemate is a radiation shielding around the beam line and the experimental zone. It is built out of blocks of heavy concrete and therefore it looks like a bunker or just a casemate.

For the replacement of the beam tube during the reactor shutdown in the winter 2004/2005, the casemate was removed and rebuilt later. We used this work as an opportunity to apply some modifications and to enlarge the casemate.

The casemate is divided into two sections (Fig. 3.3). The primary casemate is the one which surrounds the beam tube and the Lohengrin magnet. It exists since the first days of Lohengrin. Safe for a security shutter in the wall of the reactor pool, there is no other system to close the beam. During normal operation this security shutter never closes so that the beam is open for all the 50 days of one reactor cycle and activates the material inside the casemate. The radiation becomes very high and the interior classified as red zone with the reactor running or orange zone during a shut down. For this reason the casemate must stay closed and opened only in case of emergency.

The secondary casemate confines the experimental zone and was specially built for NEUTROGRAPH. This casemate is accessible under the conditions described in section 3.3.3. In the following the word casemate represents always this secondary casemate unless it is explicitly described as primary.

With a length of approximately 1700 *mm* the casemate quickly turned out to be too small for several experiments. Also the height of 2495 *mm* was not sufficient. When the casemate was rebuilt in 2005, it was extended by 800 *mm* and the height was increased by additional 400 *mm* (Fig. 3.11).

The casemate features now an experimental zone of

- 5.8 *m*² area
- 2.9 *m* height

3.3.1 Sample Environment

At NEUTROGRAPH, objects with dimensions from a few *mm* up to 1 *m* and with weights ranging from a few *mg* to about 1000 *kg* can be investigated. These objects need to be positioned horizontally and vertically in reference to the beam. In the case of tomographic imaging they are also rotated around a vertical axis.

We wanted the precision of the positioning to be higher than the detector's pixel size of about 100 μm . Linear and rotational stages are available which can handle even the heaviest objects with the recommended precision. However, these devices should not be exposed to strong vibrations which occur in the experiments on the combustion engines (chapter 6.1). The large spectrum of objects led to the idea of a flexible set-up with removable components. It consists

out of a lifting table for vertical alignment, two horizontal linear stages and two rotational stages of different sizes. The precision of positioning the object is:

- **vertical:** a few mm, new positioning devices with a precision of $10\ \mu\text{m}$ are projected
- **horizontal:** $10\ \mu\text{m}$ resolution, $20\ \mu\text{m}$ repeatability
- **rotation:** 0.0025° (0.0375°) per step

Vertical Axis

A lifting table is used as support which is adjustable in height [Will]. It can handle $300\ \text{kg}$ and lift them from $400\ \text{mm}$ to $1300\ \text{mm}$. With additional support from two steel rods, it also withstands the strong motor vibrations.

The table is placed on one layer of lead bricks for reasons explained in section 3.3.3. Though a system with a connection to rails at one wall of the casemate would be more stable, we preferred a stand alone system to be able to easily remove it in case a larger object should be investigated (e.g. a BMW car engine, chapter 6.2.1).

A ballscrew feed drive drives the table and an electric brake prevents the table from losing height. The table movement is controlled by two push buttons and can not be controlled precisely. It is used to align an object in the beam within a few millimeters. Once the position has been arrived, it must not be changed during a measurement. A T-groove plate on top of the table allows to easily install further components.

Horizontal Axis

For horizontal movement two linear stages are available [Isel]. Both are equipped with a ballscrew feed drive and are driven by a stepping motor. The resolution is $10\ \mu\text{m}$ per step and the repeatability of an absolute position is $20\ \mu\text{m}$. For the positioning of the samples the bigger one is used. It has a travel range of $800\ \text{mm}$ and can handle a load of $30\ \text{kg}$. The smaller one is only auxiliary. Its travel range is $250\ \text{mm}$ and it moves loads of up to $5\ \text{kg}$.

Rotational Axis

For tomography applications the rotation is realized by one of two rotational stages, which are both equipped with a stepper motor. For most experiments the bigger one is used [Isel], which has a resolution of 0.0375° per step and can handle $10\ \text{kg}$. The smaller rotational stage is from [Micos] and has a resolution of 0.0025° per step. It handles $500\ \text{g}$.

The horizontal as well as the axes of rotation are driven by two controller crates from `iselautomation` [Isel]. Self written software controls these crates and synchronizes them with the detector.

Diverse

To the sample environment belongs also a venting system which was installed for the motor experiments (chapter 6.1). To bring the exhaust gases from the combustion engines out of the casemate and the reactor hall, a tube has been installed inside the casemate and has been connected to the reactor venting system. A flexible metal tube was used to connect the engine directly to the venting system. 5 meters of metal tube were enough to cool the exhaust gases from a 6 kW engine sufficiently down before they entered the plastic tubing.

3.3.2 Collimators

For the year 2006 we plan the installation of an optional pair of soler collimators with a projected divergence of $L/D = 660$. The collimators consist of a stack of stainless steel plates of 0.076 mm thickness with small gaps of 0.75 mm in-between. The length of the plates is 500 mm. The plates are covered with ^{10}B and absorb all neutrons hitting one of the plate. Due to the paint the plate thickness increases to 0.126 mm. The collimators will be installed onto the primary shutter system (Fig. 3.12). A revolver at the side of the primary shutter contains three beam tubes: the first one is empty, the second one contains the collimators and the third one is for future installations. The revolver moves the tubes in and out of the beam.

The collimator plates create a pattern on the detector with intensity variances of 18 %. It would be better to place the collimators in a larger distance to the detector. However, this is not possible due to spatial restrictions. There are two reasons why we do not project a higher collimation. First there are technical restrictions in the fabrication. Second a higher collimation would cause a stronger pattern.

We calculated that the collimators will reduce the neutron flux by a factor of 30 down to $10^8 n cm^{-2} s^{-1}$, which is still an excellent value in combination with this collimation.

3.3.3 Radiation Protection

A good radiation shielding is mandatory at a high intensity instrument such as NEUTROGRAPH. The total flux of the neutron beam is about $10^{12} n s^{-1}$ and in addition to the neutrons a very intense beam of gamma rays emerges from the beam tube. Furthermore, the neutrons are

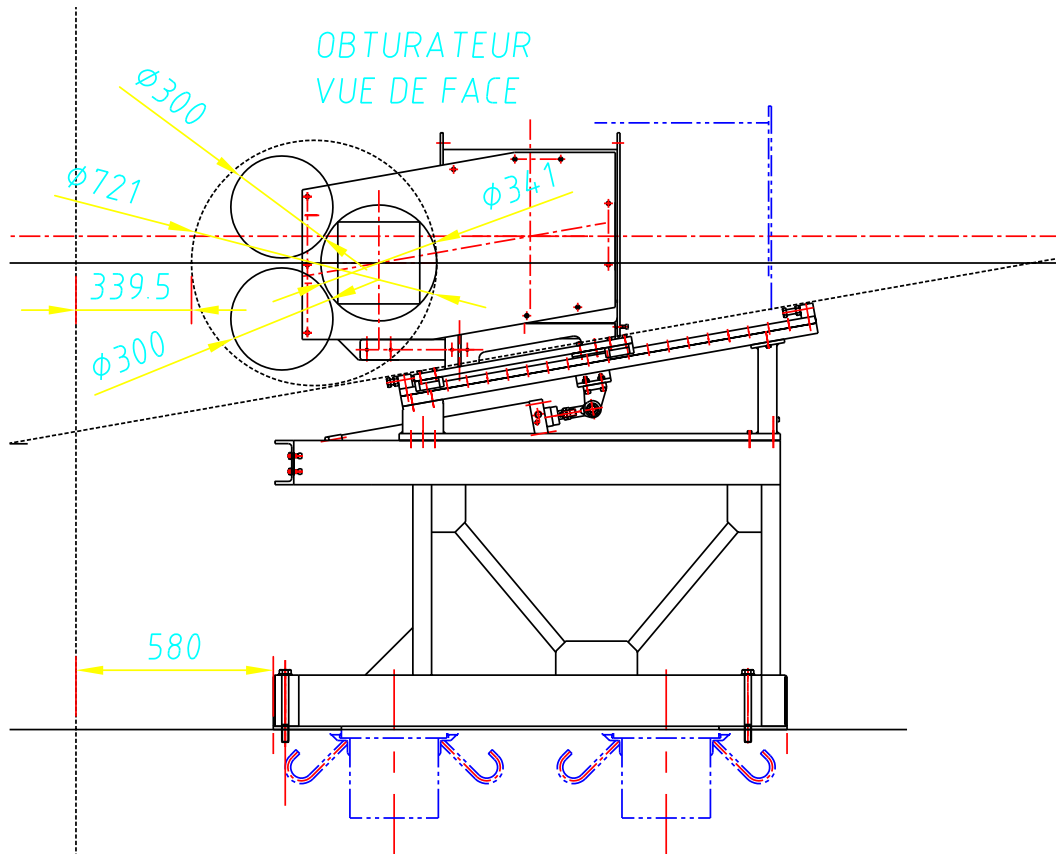


Figure 3.12: Draft of the primary shutter system with projected revolver: The revolver contains an empty beam tube for normal operation, one beam tube containing the collimators and a third beam tube for future installations. (Drawing F. Fihman, Bureau d'Etudes, ILL)

scattered in all directions by the sample, the detector or other objects in the beam and by neutron absorption in material, secondary γ -radiation is emitted into the whole solid angle. In a distance of one meter to the sample, the γ dose rate goes up to 0.1 Gy h^{-1} . Therefore a fully closed casemate as radiation shielding is necessary.

The casemate is made out of blocks of heavy concrete, a special mixture containing a big amount of metal. The metal inside the concrete increases the mass density of the material in order to increase the γ absorption coefficient. The wall which divides the primary from the secondary casemate as well as the opposing wall are of 1 m thickness, because they cross the beam axis. For the side walls and the roof 800 mm are sufficient.

The floor of the casemate is made out of conventional concrete of 1 m thickness. This type of concrete has minor radiation shielding properties. When materials are put into the beam which cause a prompt γ production (e.g. Cd and steel), the γ dose rate goes up to even 1 Gy h^{-1} . In these cases an additional layer of 100 mm of lead beneath those materials must be put in place to prevent a radiation problem on the floor beneath the casemate.

In order to lower the activation of the walls due to neutron absorption, the interior is clad with 5 mm thick B_4C containing rubber. At the back wall, a shield of 5 mm thick 6LiF plates stops the direct neutron beam. The advantage of 6Li over B is the higher neutron absorption efficiency and the fact that this process does not create γ rays, which could disturb the detector. Inside the primary casemate, directly in front of the feed through of the beam, a big shutter interrupts and opens the beam. This shutter consists out of a 100 mm thick iron plate followed by a block of heavy concrete of 1 m length. In its rest position the shutter is closed. In order to open the beam, a pneumatic system moves the shutter up on a ramp. In case of a failure of the pneumatics, the shutter moves down by gravity and closes the beam.

A secondary shutter is installed at the other side of the wall inside the secondary casemate. It opens and closes in about 2 seconds. Being made out of 50 mm of borated polyethylene, it absorbs most of the thermal and cold neutrons, but it does not provide any radio protection. This shutter was installed to quickly open and close the neutron beam in order to reduce the activation of the sample and the casemate equipment significantly in cases, where the exposure time is short compared to the opening and closing time of the primary shutter.

3.3.4 Safety Installations

For the safety of workers and experimentalists several systems have been installed.

To open the primary shutter, the door must be closed and locked. The key from the door lock is needed as authorization to open the beam, but it can be removed from the door lock only, when the door is locked. In this way it is not possible to open the beam while the door is still open. When the shutter has been opened and closed again, a γ detector measures the radiation level inside the casemate which is due to the activation of the materials. This detector is situated in a distance of about 1 m to the sample and it is connected to the shutter controller box outside the casemate. While the radiation is still high, the key can not be removed from the shutter controller box, which is needed to open the door. Only when the radiation drops beneath the threshold of $90 \mu Gy h^{-1}$, the controller box releases the key and the door can be opened.

For the case of an accident with persons involved, an emergency button is installed inside the casemate. This button activates an acoustical and optical alarm outside the casemate and informs the reactor control room. Two video surveillance cameras are installed inside the casemate and connected to monitors next to the shutter control at the casemate entrance. In this way the experiments can be monitored optically and acoustically from outside the casemate. In some experiments highly inflammable and even explosive materials are used (e.g. gasoline, pentane, hydrogen). In the case of an emergency these materials represent a special risk. When the radiation level inside the casemate is above the threshold, it is impossible to enter

the casemate to take counter measures. For this reason a fire extinguisher system was installed which can be activated manually from outside the casemate. It consists out of a big bottle of pressurized CO₂, which can fill the casemate and extinguish the fire in a short time. A warning above the casemate entrance informs people about the danger of asphyxiation.

3.4 Detector System

For the detection of neutrons, several detectors are available. They range from simple photographic films over imaging plates, ³He-counters to flat panels and scintillator-CCD-camera systems. They all differ extremely in their properties and are best suited for their specific application.

In neutron imaging, where an excellent spatial resolution is recommended, three types of detectors are used. The development of these detectors gave neutron imaging the decisive boost during the last decades.

Imaging Plates

Imaging plates provide an excellent spatial resolution and excellent image quality. Furthermore they are simple to use. However, bright neutron sources quickly overexpose them and they can not be used in applications where a series of images has to be acquired, e.g. for tomography or radiographic films.

Flat Panels

Flat panels are detectors consisting out of many pixels with a size down to 50 μm . Each pixel contains a conversion layer, where neutrons are converted into electrons, and the read-out electronics. After the exposure, the image is read out on a seconds time scale and directly accessible as digital data. Their advantages are the good spatial resolution and image quality as well as the capability of single neutron detection. On the other hand the neutron detection efficiency of about 15% is very low and they are overexposed in beams such as the one of NEUTROGRAPH.

Scintillator-CCD-Camera Systems

The third and mostly exploited detection technique is a system of a scintillation screen and a camera. In this case, the neutrons hit the scintillation screen after their transmission through the sample. The scintillator converts them into visible light, which creates an optical image of

the sample. A camera records the image and makes it available as digital data.

The advantages are the system's ability to create a series of images and its high flexibility. The system is modular and with the right selection of the single components, it can be adapted to a multitude of different applications. However, this system is not as simple to use as the other two detection techniques.

3.4.1 Scintillator

Scintillators exist in a big variety of different types. However, they all work with the basic principle. A conversion material captures the incoming neutrons and creates charged particles. These charges travel through a phosphor or an other scintillating material and produce light. Since NEUTROGRAPH exploits a thermal neutron beam, this section deals only with scintillators suited for this application.

The scintillators differ in the conversion material, the phosphor or other scintillating material, the mixture, their physical state and the thickness. These differences result in a big variety of detection efficiencies, light output per detected neutron, spectrum of the emitted light, spatial resolution, "afterglow" or time resolution, sensitivity for γ -rays and lifetime.

Conversion Material

The most common conversion materials are Gadolinium and Lithium-6. In the case of Gd, the neutron capture stimulates a prompt β -emission. The electrons then stimulate the light emission in the surrounding material. Gd-scintillators are sensitive for neutrons and X- and γ -rays as well. They are very common in medical applications and therefore produced in large numbers, which makes them cost effective. However, their sensitivity to photons does not allow to use them at a neutron facility with a high γ -background like NEUTROGRAPH.

Lithium containing scintillators are sensitive to photons too, but on a level which is by far lower than in Gd-scintillators. When a neutron hits a ${}^6\text{Li}$ nucleus, it stimulates the following reaction:



The two charged particles travel through the scintillator with the total kinetic energy of 4.5 MeV . By ionization, this kinetic energy converts into light emission.

Physical State

Scintillators are available as plates of plastic material, glass plates or as a liquid confined in a small gap between two glass plates. The glass and liquid scintillators normally are transparent

to their emitted light. Therefore it is very simple to increase the detection efficiency to nearly 100 % by enlarging the thickness. The problem is the decline of spatial resolution, in particular in detector systems with a short optical path. The information, on which ray the neutron has been detected, is lost. Furthermore, the light emission per detected neutron is by far lower than in a plastic scintillator, at least for the tested samples from AST.

Plastic scintillators for neutron detection are a homogeneous mixture of the conversion material and a phosphor. Often they are mounted onto an aluminum plate to make it more stable. The light spots created by a single neutron capture event have diameters of about 100 μm . The light efficiency is much higher. The kinetic energy of the charged particles is nearly completely converted into light, which means an isotropic emission of about 10^5 photons depending on the photon's wavelength.

The problem of this type of scintillator is the opacity for the own emitted light. Only the photons created inside a thin layer of a few μm thickness beneath the surface are not reabsorbed. Therefore it makes no sense to increase the thickness of the scintillator above 500 μm .

Though the small usable thickness of the scintillator does not allow to increase the detection efficiency up to nearly 100 %, the high density of the conversion material makes an efficiency of yet 30 % possible. On the other side, in addition to the higher light emission per detected neutron, the spatial resolution is of the size of the light spots and not as big as in a glass or liquid scintillator of increased thickness, because of the lack of a parallax.

Tested Scintillators

For NEUTROGRAPH, scintillators are used with a light emission in the green spectrum with a peak at 550 nm. This corresponds to the wavelength of the cameras' maximum sensitivity (3.4.2). The NDg screen from Applied Scintillation Technologies [AST] are mostly used. In tests their performance was compared with a GS20 6Li glass scintillator and recently developed screens from the NEUTRA-team [NEUTRA] at the Paul-Scherrer-Institut.

3.4.2 Camera

The choice of the right camera is very crucial for the quality of the instrument. At NEUTROGRAPH we use a Sencicam from PCO Computer Optics GmbH [PCO]. It features:

- **resolution:** 640×480 pixels
- **exposure times:** 100 *ns* - 1000 *s*
- **readout / frame rate:** 33 *ms* read out time, 30 *Hz* frame rate

- **dynamic:** 12 bits
- **modi:** sequential, simultaneous, on-chip integration
- **cooling:** cooling of the chip to -14°C
- **quantum efficiency:** 40 % @ 550 nm

3.4.3 Detector Housing and Optics

In a Scintillator-CCD system such as used at NEUTROGRAPH, the two components are installed in a certain distance. To prevent the measurement from being influenced by surrounding light sources, either the experimental zone must be completely dark or the scintillator, the CCD camera and the optical path in between must be encapsulated by a light tight box. Since for security and for practical reasons the experimental zone at NEUTROGRAPH is always illuminated, a detector housing has been built.

The actual detector housing has been designed by our former diploma student Arnd Gildemeister [Gild03]. It incorporates following features:

- Light tightness to prevent the measurement from being influenced by surrounding light sources.
- Built out of aluminum for a low interaction with neutrons and a short half life time.
- The detector housing incorporates two mirrors which deflect the optical path out of the neutron beam. This is important for an efficient radiation shielding of the camera. While at most neutron radiography facilities only one mirror is used, we decided to use at NEUTROGRAPH a pair of mirrors due to the high intensity of the neutron beam.
- The housing is a composition of three sections. The middle piece exists in three different lengths. The two end sections can be combined with each of the middle sections to form a detector housing with an optical path of 500, 700 and 1000 mm length. The angle can be varied in steps of $\pi/2$.
- The section of the housing which is exposed to the direct beam is built with a minimum of material in order to reduce neutron interaction and the creation of γ 's.
- For the same reason the first mirror is a special production. A standard Si waver forms the basis. A thin layer of aluminum, sputtered onto the surface of the waver, reflects a

3 The ILL - Tomography Station Neutrograph

broad band of visible light. To prevent a loss of the reflecting properties of the aluminum by oxidation, a thin layer of sapphire protects the aluminum from contact with air.

- The inner surfaces of the detector housing are black in order to minimize reflections and light diffusion.

4. Data Evaluation

4.1 Image Normalization

The aim of radiography is to create a two dimensional map of beam transmissions through an object, $\varphi = \frac{I}{I_0}$, where I_0 is the incident and I is the transmitted beam intensity. For the creation of these maps the acquired images have to be treated in the following way:

- All grey value representations in the images contain a certain offset which must be subtracted from each picture before further treatment. This is done by the subtraction of dark images, images which are acquired with no light exposure.
- Inhomogeneities of the beam profile and the scintillator must be normalized out by dividing every image by an open beam image, an image which was recorded with no object in the beam.

This results in the basic formula

$$\varphi = \frac{I}{I_0} = \frac{p - d}{o - d} \quad , \quad (4.1)$$

with p the image of the object, d the dark image and o the open beam image.

4.2 Statistical and Readout Errors

Neutron radiography is the acquisition of images created by neutrons via their conversion into charged particles, photons and electric charges. This long conversion chain is described by the equation

$$gv = I A t_{exp} q_{sc} \cdot n_{\gamma} L q_o q_{ccd} \cdot q_{a/d} \quad , \quad (4.2)$$

where gv is the grey value representation, I is the beam intensity, A the area viewed by one pixel and t_{exp} the exposure time. q_{sc} is the efficiency of the scintillator, n_{γ} the number of photons

created per detected neutron, L the fraction of photons which arrive at one pixel of the camera due to the geometry of the optical path and the camera lens and q_o is the reflectivity of the mirrors. Finally q_{ccd} is the detection efficiency of the camera and $q_{a/d}$ the conversion factor of created charges to grey values.

(4.2) can be rewritten as

$$gv = N_n \cdot n_e \cdot q_{a/d} \quad , \quad (4.3)$$

with N_n being the number of neutrons detected by the scintillator and n_e being the number of created charges per detected neutron, i.e. the number of detected photons per neutron. The detection of neutrons or photons respectively is a statistical process. N_n has the statistical relative error $r_N = 1/\sqrt{N_n}$. The detection of neutrons via the conversion of neutrons into photons increases the relative error. The number of created charges $N_e = N_n \cdot n_e$ has the statistical errors

$$\sigma_e = \sqrt{N_n} \sqrt{n_e + n_e^2} = \sigma_n \sqrt{n_e + n_e^2} \quad (4.4)$$

and

$$r_e = \frac{\sqrt{N_n} \sqrt{n_e + n_e^2}}{N_n n_e} = \frac{\sqrt{1 + \frac{1}{n_e}}}{\sqrt{N_n}} = r_N \cdot \sqrt{1 + \frac{1}{n_e}} \quad (4.5)$$

[Gild03]. The conversion of charges into grey values with the factor $q_{a/d}$, the readout of the image, has no statistical error. However, a constant error (readout noise) of $\sigma_{ro} = 13 \text{ charges}$ is related to this process. Using (4.3) the preliminary errors of the grey value are

$$r_{gv}^* = \sqrt{r_e^2 + r_{ro}^2} = \sqrt{\frac{q_{a/d}(1+n)}{gv} + \frac{\sigma_{ro}^2}{gv^2}} \quad (4.6)$$

and

$$\sigma_{gv}^* = r_{gv} \cdot gv = \sqrt{gv q_{a/d}(1+n) + \sigma_{ro}^2} \quad (4.7)$$

In (chapter 4.1) it is explained that in each image an offset has to be eliminated by subtracting a dark image. The dark image has the same readout error as the data image. We take this into account by multiplying σ_{ro} with the factor $\sqrt{2}$:

$$\sigma_{gv} = \sqrt{gv q_{a/d}(1+n) + 2\sigma_{ro}^2} \quad \text{and} \quad r_{gv} = \sqrt{\frac{q_{a/d}(1+n)}{gv} + \frac{2\sigma_{ro}^2}{gv^2}} \quad (4.8)$$

In bright images the first term dominates and the term due to the readout noise is neglectable. Then $r_{gv} = r_e$.

4.3 Systematic Errors

In addition to the statistical errors there are some systematic errors, which have to be minimized according to the requirements of the experiment. The systematic errors which occur at NEUTROGRAPH are the degradation of the scintillators, fluctuations of the beam intensity and fluctuations of the grey value representation in the images.

4.3.1 Scintillator Degradation

The high intensity of NEUTROGRAPH's neutron beam has not only advantageous. It turned out that the scintillators degrade very quickly when exposed to the high flux. They become brownish and they emit less light. The problem is not only the loss of light emission and with it the loss of statistics, but in particular the inhomogeneity of degradation due to the inhomogeneity of irradiation. When only a simple radiograph is acquired, the effects are completely eliminated with the normalization (chapter 4.1). The problems arise, where the experiment runs for a longer time and images from different time steps are integrated or compared.

In a collaboration with [NEUTRA] we investigated and compared the degradation of the NDg screens from [AST] and some screens developed at [NEUTRA]. All the tested scintillators work on the basis of ^6Li . There are also screens on the basis of Gd available. They were not used, because the Gd has a larger absorption cross section for γ -rays. The high γ -background at NEUTROGRAPH would disturb the measurements. The NDg screens from [AST] have different thicknesses. The screens from [NEUTRA] differ not only in thickness but also in the mixture relations Li:Binder. Small sample pieces were irradiated for 25 h (Fig. 4.1)).

1. NDg from [AST], 250 μm thickness
2. NDg from [AST], 500 μm thickness
3. V2 from [NEUTRA], 288 μm thickness, 1:1 (Li:Binder)
4. V5 from [NEUTRA], 299 μm thickness, 1:4 (Li:Binder)
5. V6 from [NEUTRA], 324 μm thickness, 1:2 (Li:Binder)

Fig. 4.2 shows the mean brightness in the regions of interest over time. One can see that the brightness depends on the thickness (compare 1. and 2.) and the concentration of Li (3. and 4.). One can see also that the brighter the scintillator at the beginning (the higher the amount of Li), the quicker the brightness declines. The decay follows an exponential function of the type

$$y = A_1 \cdot e^{-t/\tau_1} + A_2 \cdot e^{-t/\tau_2} + y_0 \quad (4.9)$$

This was verified for all the scintillators, but Fig. 4.3 shows only the curve from sample 2. According to the fit, for very long irradiations the brightness of the NDg declines to 33 % of its initial value. This has not been validated yet.

We also tested, if the degradation is caused only by neutrons or if γ -rays have a comparable effect on the scintillators. For this experiment we opened the primary shutter, but let the secondary shutter closed. With this set-up the full γ -beam hit the scintillator while the thermal and cold neutrons were blocked. Also a part of the epithermal and fast neutrons penetrated the secondary shutter. One half of the scintillator was shielded by 50 mm of lead and 50 mm of borated polyethylene. This reduced the γ -flux by approximately 10 %. After 21:26 hours of irradiation the brightness on the two sides of the scintillator differed by less than 1 %. This means that at NEUTROGRAPH the effect caused by γ -rays can be neglected compared to the one cause by neutrons.

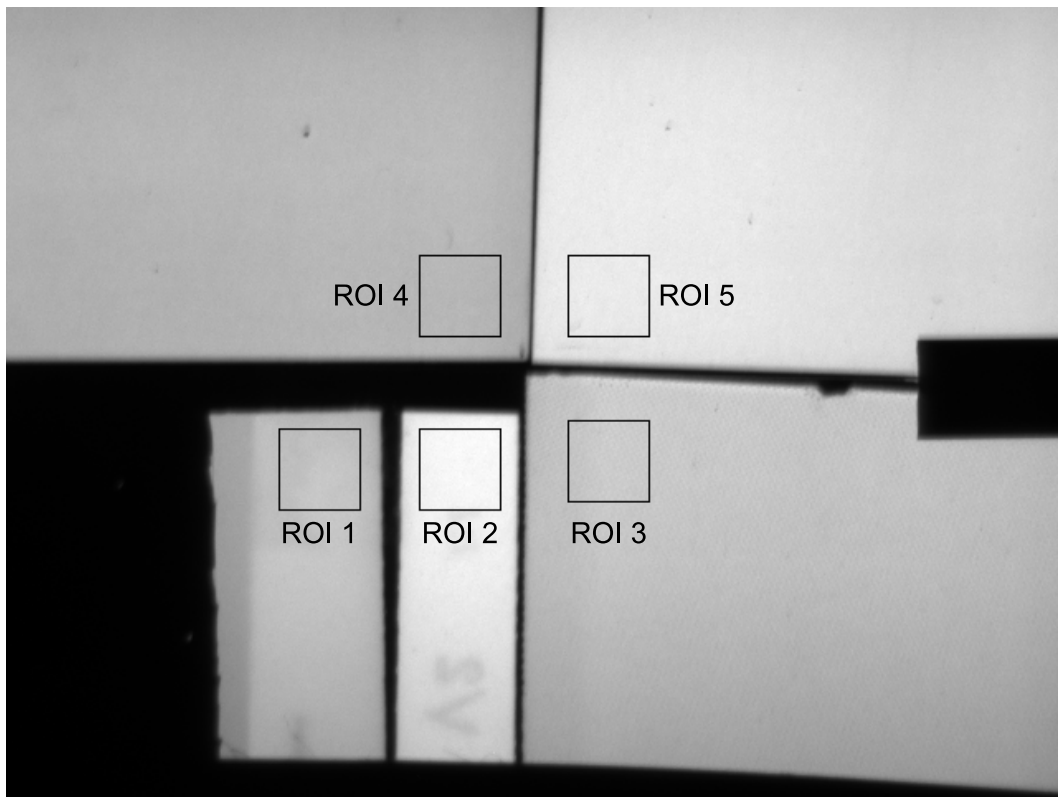


Figure 4.1: Several scintillator samples

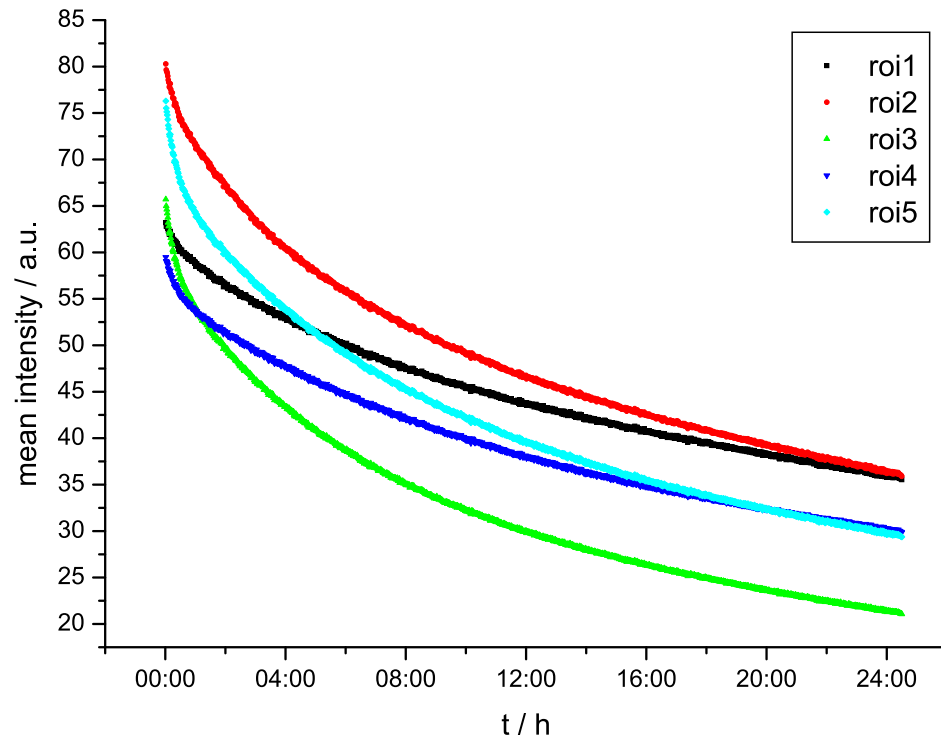


Figure 4.2: Scintillator degradation

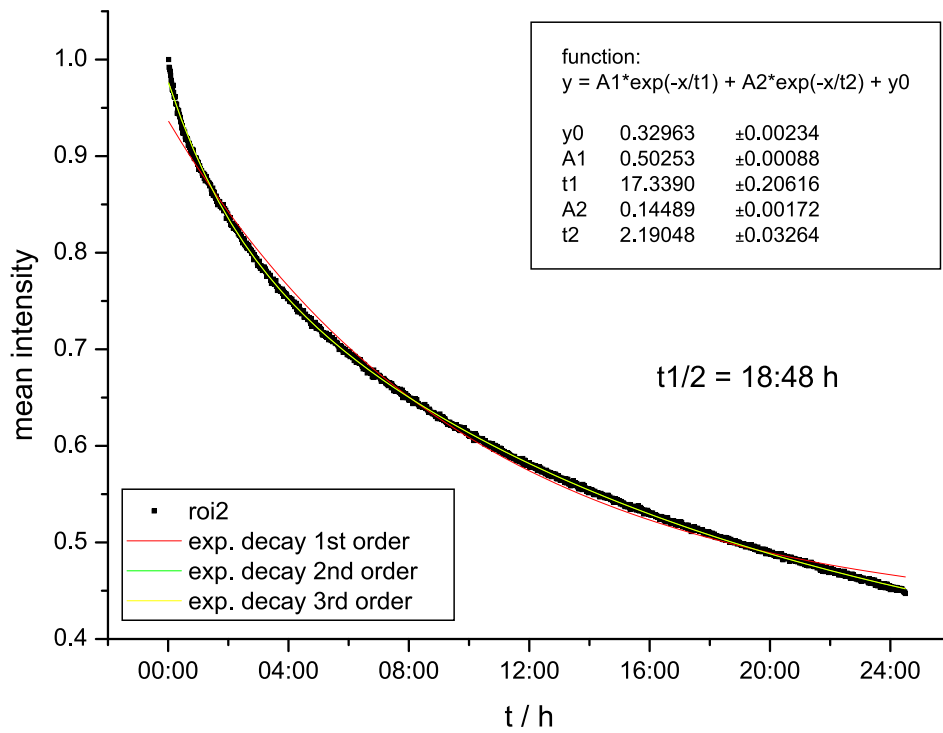


Figure 4.3: fit of decay curve

4.3.2 Correction of Scintillator Degradation

How can the effects of scintillator degradation be eliminated?

- Each image has to be normalized by an open beam image, which was acquired not too long before or after the data image.
- In radiographies on static objects, one acquires an open beam image at the beginning AND at the end of the experiment, o_b and o_e . Now for each time step of the experiment an individual open beam image can be calculated by interpolation in-between o_b and o_e . In case the experiment runs for hours, the precision can be increased by recording several open beam images during the measurement, if possible. This method works only if it can be assumed that the transmitted beam intensity is constant over time for each point on the detector.
- If either the object changes itself or if a static object is rotated for a tomography, the transmitted neutron flux is not constant over time. In this case the simple interpolation does not work. There are two possibilities for the correction:
 1. If possible, open beam images are acquired in short intervals during the measurement. In this way one can apply the simple interpolation method and keeps the errors small.
 2. There are experiments, where this method can not be applied (dynamic radiography or even dynamic tomography). For these cases an interpolation algorithm is needed, which takes the history of beam intensities into account.

New Correction Algorithm for Scintillator Degradation

For the problem of non-static objects the correction algorithm has to take the history of beam intensities into account. The history is saved in the image series \vec{p} . However, to know the neutron flux φ_t which hit the detector at a certain time, the acquired image has to be normalized by an unknown open beam image o_t . To calculate this open beam image, the normalized images are needed. Therefore the algorithm must calculate the open beam images and normalize the data images in iterations.

Ansatz: We assume the following measurement procedure:

1. acquisition of first open beam image o_b

2. acquisition of a series of n images $\vec{p} = [p_1, p_2, \dots, p_n]$
3. acquisition of last open beam image o_e

The data treatment aims on finding the normalized images

- $\vec{\varphi} = [\varphi_1, \varphi_2, \dots, \varphi_n]$ (corresponding to a map of the transmitted neutron flux) by normalizing \vec{p} with the open beam images
- $\vec{o} = [o_1, o_2, \dots, o_n]$, with $o_t = f(o_b, \varphi_1, \dots, \varphi_t)$ and $o_n = o_e$.

From (chapter 4.3.1) we know that an exponential function of 2nd order is the best fit for the decay curve. However, with only two conditions (4.12) and (4.13), it is somehow problematic to find the right parameters. It is much more easier with an exponential function of 1st order and the error is still small if the measuring time is not too long. Fig. 4.4 compares the fit function of 1st and 2nd order for a measuring time of 2h. So the decay is assumed to follow the function

$$f(t) = \frac{o_t}{o_b} = A \cdot e^{-t/\tau} + y_0 \quad (4.10)$$

Since the decay depends only on the history of the neutron flux, the exponent t/τ can be replaced by $\lambda \sum_{i=1}^t \varphi_i$ and (4.10) rewritten to

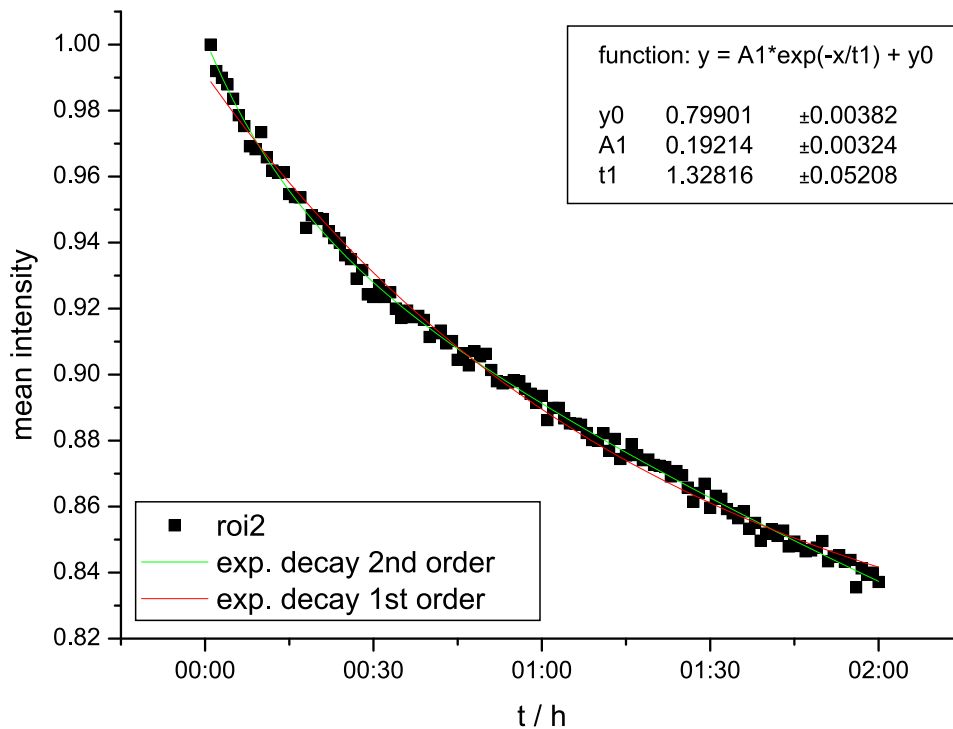


Figure 4.4: fit of decay curve

$$f(t) = \frac{o_t}{o_b} = A \cdot \exp(-\lambda \sum_{i=1}^t \varphi_i) + y_0 \quad (4.11)$$

Two conditions have to be fulfilled:

$$f(0) = A + y_0 = 1 \quad (4.12)$$

$$f(n) = \frac{o_n}{o_b} = \frac{o_e}{o_b} = A \cdot \exp(-\lambda \sum_{i=1}^n \varphi_i) + y_0 \quad (4.13)$$

With y_0 being known from Fig. 4.4, we calculate the two parameters A and λ from (4.12) and (4.13):

$$A = 1 - y_0 \quad (4.14)$$

$$\lambda = \frac{\ln A - \ln(o_n/o_b)}{\sum_{i=1}^n \varphi_i} \quad (4.15)$$

Now the function $f(t)$ is known save for the neutron flux history $\vec{\varphi}$. $\vec{\varphi}$ and \vec{o} have to be determined in iterations:

- **start:** $\vec{\varphi} = [1, 1, \dots, 1]$

- **iteration:**

1. $\lambda = \frac{\ln A - \ln(o_n/o_b)}{\sum_{i=1}^n \varphi_i}$
2. $\vec{o} = o_b \cdot [f(1), f(2), \dots, f(n)]$ (refer to (4.11))
3. $\varphi_t = p_t/o_t \quad \forall t \in [1, n]$

The algorithm has been tested on the tomography data of an aluminum plate of 100 *mm* width and 20 *mm* thickness. The plate was homogeneous save for a friction stir weld in the middle. Since the projected images changed a lot when the sample was rotating, the scintillator degradation depended strongly on the angle. When the images were normalized by an open beam image, which was calculated by a simple interpolation, the images featured a vertical stripe of brighter grey values (Fig. 4.5 left and Fig. 4.6 black profile), though the profile should be constant. When the iterative correction algorithm was applied, the result was much improved already after 5 iterations (Fig. 4.5 right and Fig. 4.6 red profile).

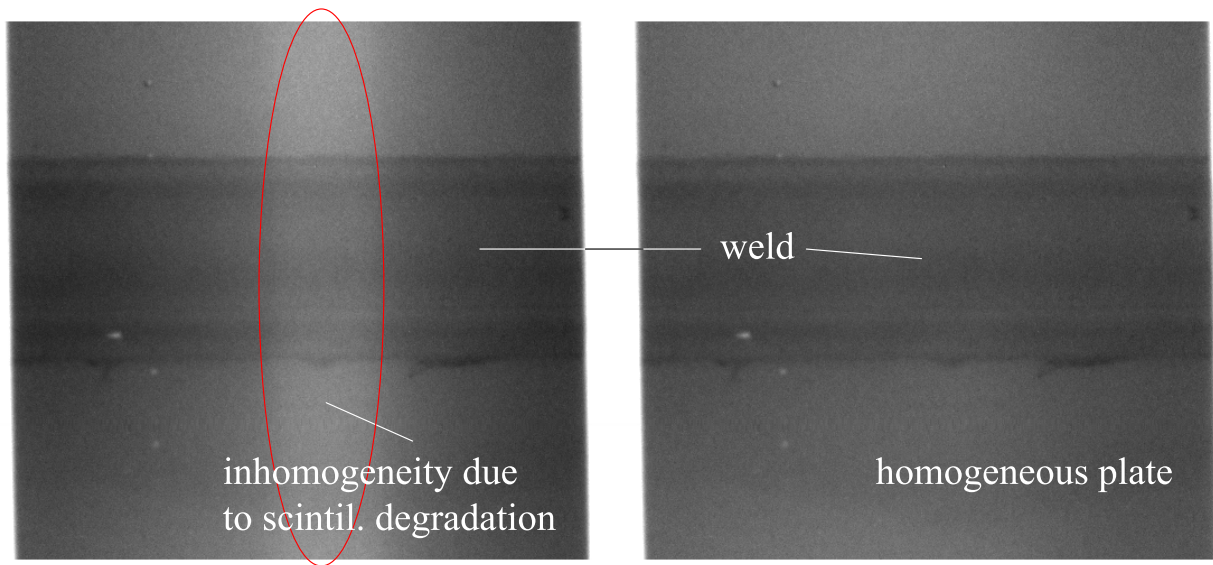


Figure 4.5: Friction stir weld: **left:** Normalized image without correction. **right:** Normalized image after 5 iterations.

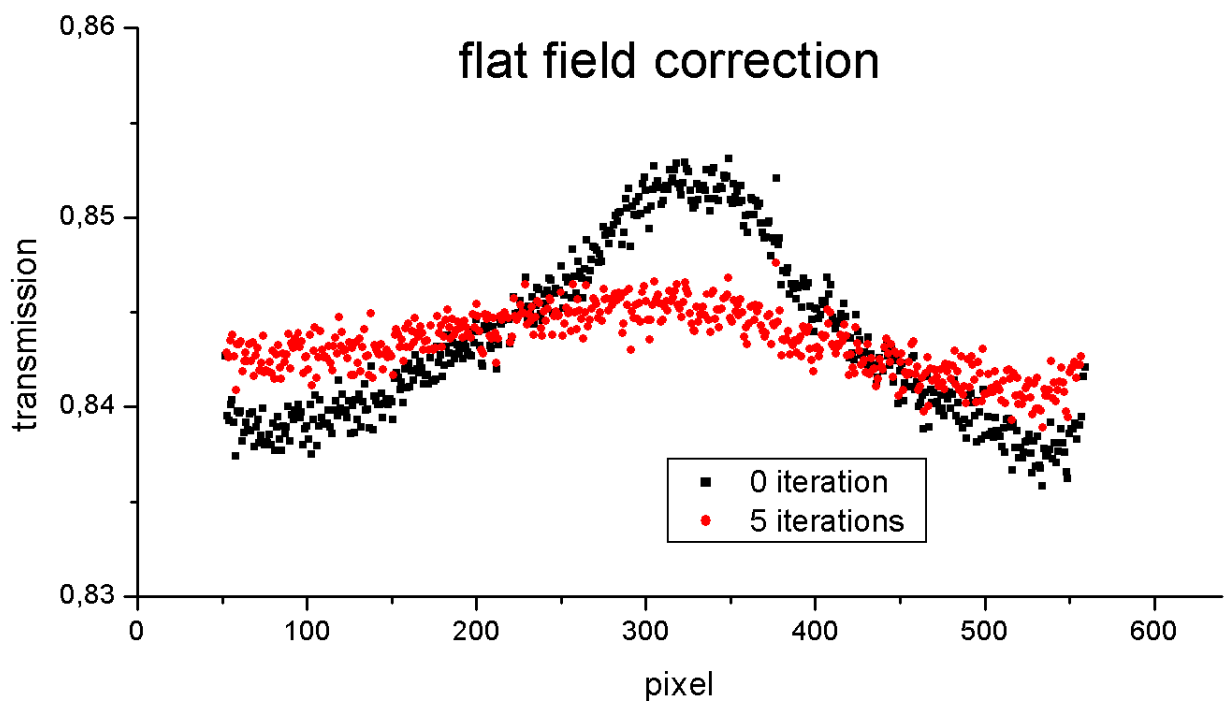


Figure 4.6: Transmission values extracted from one row

4.3.3 Intensity Fluctuations

The intensity of the neutron beam is not constant. There are some fluctuations due to the controlling of the chain reaction in reactor's fuel element. At NEUTROGRAPH there was no beam monitor installed because we did not want to disturb the beam profile. A measurement with the imaging detector contains additional errors due to an effect described in (chapter 4.3.4). Fig. 4.7 shows a typical measurement of the beam intensity with the imaging detector. It contains the fluctuations of the beam intensity and the image brightness. However with the properties of the camera error (chapter 4.3.4), one can estimate the beam fluctuations to at least 1%. From other instruments at ILL it is known that the fluctuations have a typical amplitude of 2%.

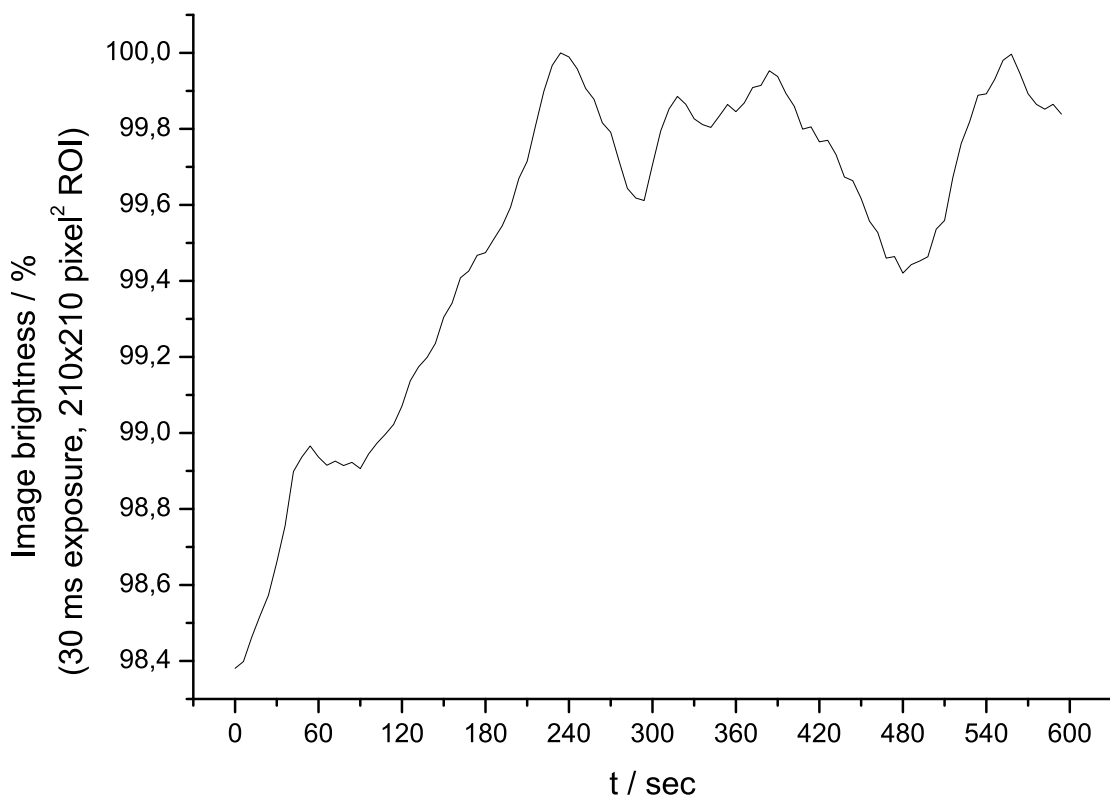


Figure 4.7: *Fluctuations of beam intensity*

For many experiments these fluctuations are not disturbing, as long as the fluctuations are homogeneous over the beam profile. If they are, they can be eliminated by rescaling the images in reference to a small area where the beam intensity is considered to be constant.

The homogeneity of the fluctuations was proofed in an experiment, where single images were acquired at different times. The images were divided into four quadrants and the mean intensity of each quadrant plotted (Fig. 4.8). Compared to the measurement error the fluctuations of

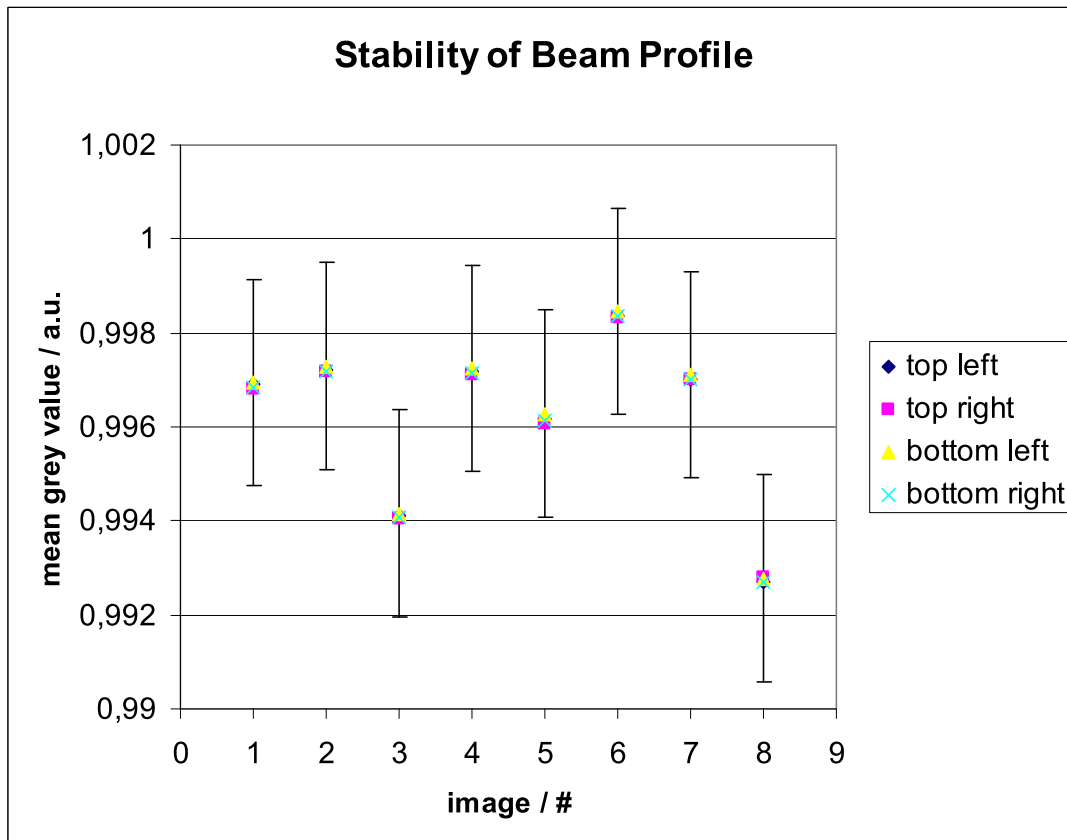


Figure 4.8: Stability of beam profile

all quadrants are identical.

In a few experiments (chapters 6.1.3 and 6.1.4) the method of rescaling the images in reference to an area of constant intensity is not possible because no such area exists. For these experiments an independent monitoring of the beam intensity is needed. A neutron counter working on the base of fission of uranium nuclei, which is highly efficient and made for high count rates, has been ordered and will be installed in 2006. This neutron counter has only very small dimensions and will therefore not disturb the image quality.

4.3.4 Camera Fluctuations

Also the conversion from detected light to its representation by grey values is not constant, which is a result of changing temperatures of the CCD chip. The chip cooling of the camera has a two-point-regulation. If the temperature reaches -15°C , the cooling is switched off, at -14°C the cooling restarts. The changing temperature results in a change of the grey value offset and is the same for all pixels and independent from the absolute grey value. In dark images the effect is relatively high and can be better investigated. Fig. 4.9, Fig. 4.10 and Fig.

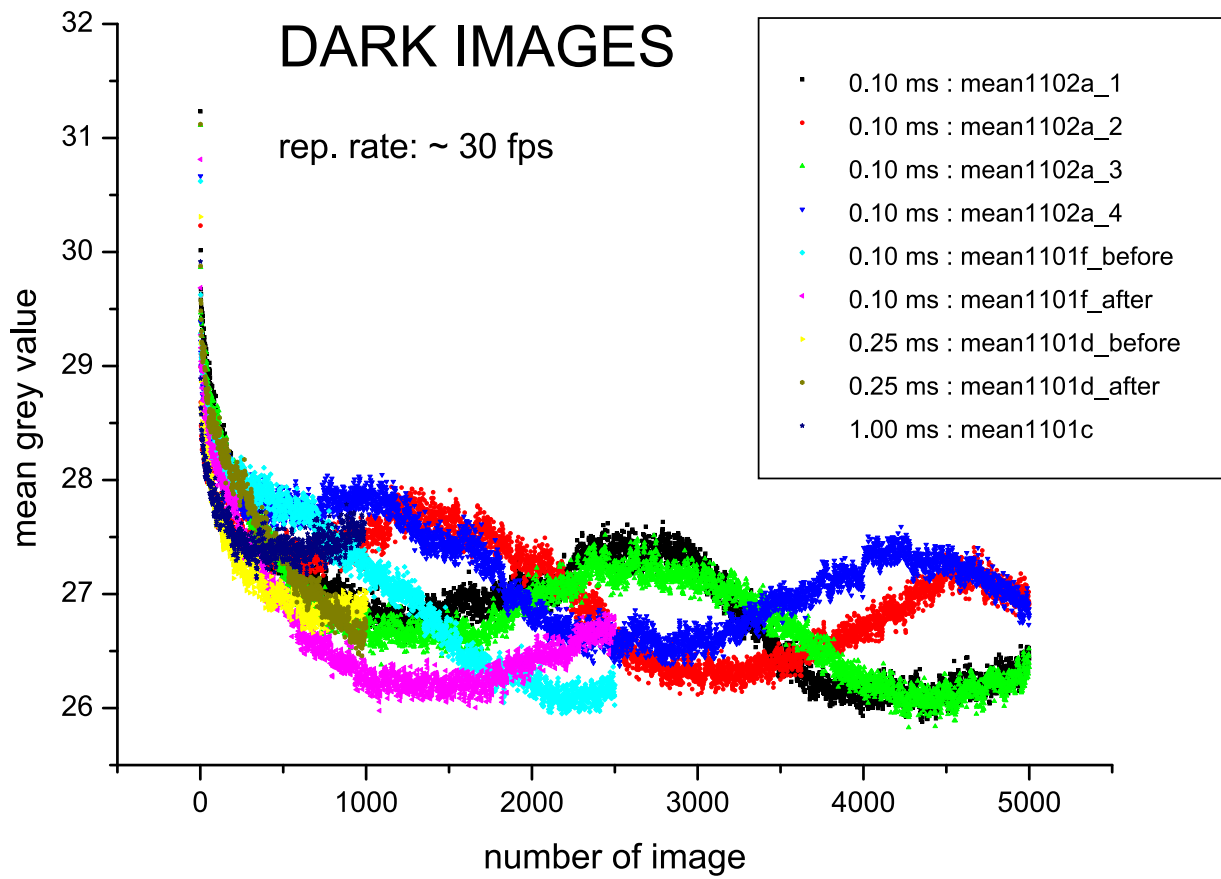


Figure 4.9: Intensity fluctuations in dark images: the displayed values are mean values of the whole chip

4.11 show the typical behavior. The grey value makes a sinus oscillation around a mean value. The frequency is independent from the exposure time (it depends only on the cooling cycle) and has a stable period of approximately 1 *min*. Also the amplitude is stable at approximately ± 0.7 *gv*. Fig. 4.9 and Fig. 4.11 show an additional effect: the first images of a series are often brighter than the following images. It is advisable not to use them.

In bright images the effect becomes relatively small ($1.4/3500 = 0.4\%$) and can be neglected. However, in experiments like the one on the diesel injection or the diesel engine (chapter 6.1.2 and 6.1.4), the acquired images are very dark. Here the effect can not be neglected. In the same way as the intensity fluctuations of the neutron beam, the cooling effect can be eliminated by referring to a small area of constant beam intensity. In some experiments this method can not be applied. For these cases it would be desirable to modify the cooling regulation in order to reduce the temperature tolerance and with it the amplitude of the fluctuations of brightness.

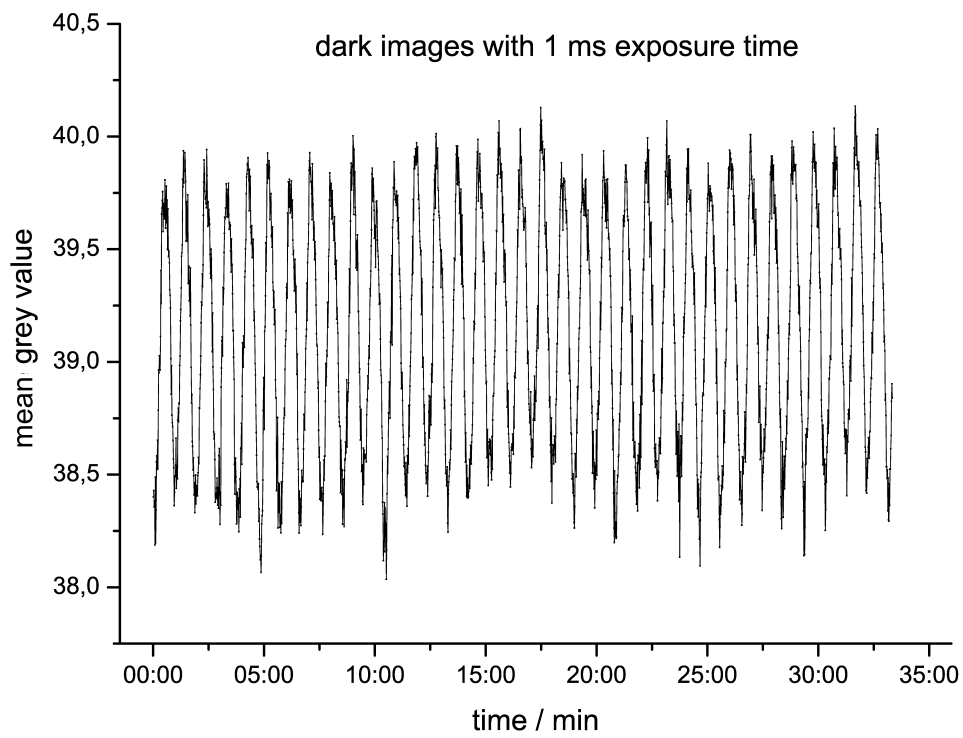


Figure 4.10: Intensity fluctuations in dark images

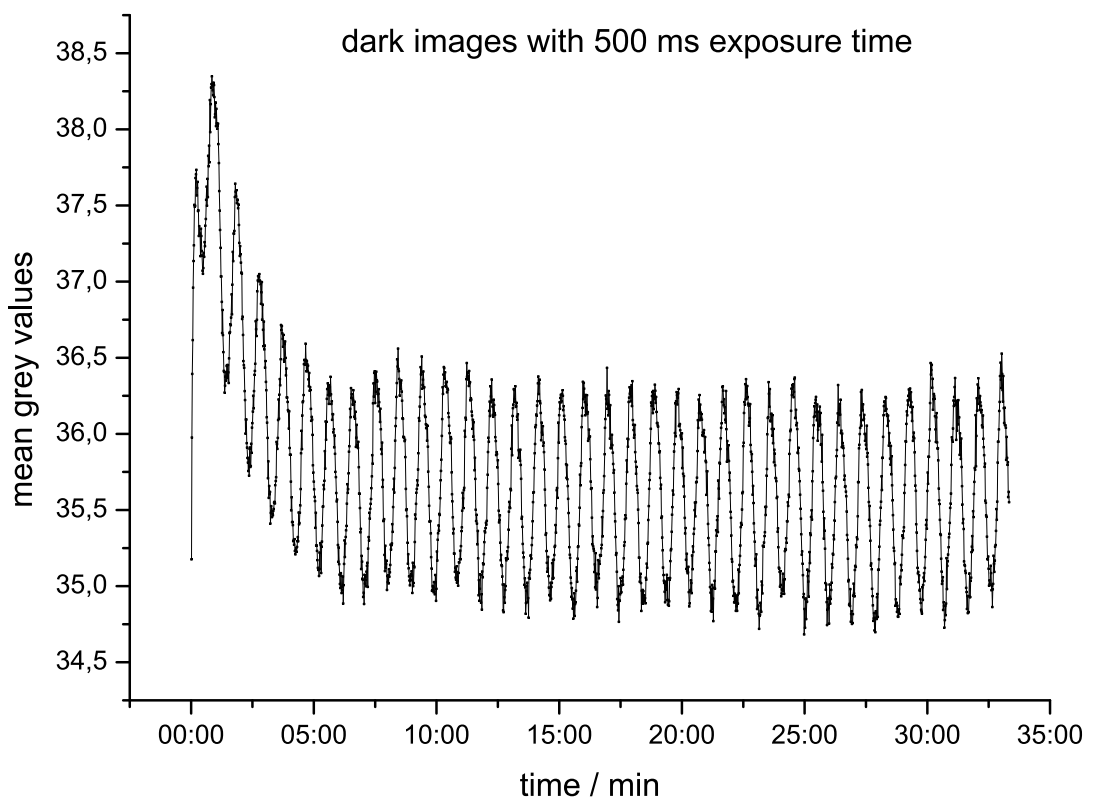


Figure 4.11: Intensity fluctuations in dark images

5. Measuring Techniques

The experiments carried out at NEUTROGRAPH differ very much in their set-up and the type of research that has to be done. For each of these experiments the measuring method has to be modified, but besides the classical radiography and tomography of static objects there are a few classes of advanced methods. This chapter gives presents an overview over these techniques.

5.1 Dynamic Radiography

Dynamic radiography is the recording of a 2D movie of a dynamic process. The time resolution is only restricted by the produced error due to statistics and the readout of the image (chapter 4.2). Depending on the requirements of the experiment time resolutions of less than 1 *ms* are realizable. Till now the best applied time resolution was 1 *ms* (100 μ s for stroboscopic radiography, chapter 5.2). A considerable restriction is the readout time, which reduces the fraction of time in which the investigated process is imaged. There are two options for the measurement procedure:

1. **sequential:** The exposer and the readout are carried out alternately. The frame rate $\nu = 1/(t_{exp} + t_{ro})$ and the fraction of the monitored time is $t_{exp}/(t_{exp} + t_{ro})$
2. **simultaneously:** The exposure and the readout are carried out at the same time. The maximum of the two values determines the frame rate, $\nu = 1/\max_t$ and the fraction of the monitored time is t_{exp}/\max_t . This is either 1 for $\max_t = t_{exp}$ or the ratio t_{exp}/t_{ro} .

If the measurement time is long enough for a significant degradation of the scintillator (chapter 4.3.1), the correction algorithm for open beam images has to be applied. In order to suppress the fluctuations of beam intensity and the camera (chapters 4.3.3 and 4.3.4), an area of homogeneous beam transmission has to be monitored and used as reference for rescaling the images. If this is not possible, an independent monitoring of the beam intensity and the camera cooling is needed.

5.2 Stroboscopic Radiography (Periodic Processes)

When a process is periodic, stroboscopic radiography can be applied. This means that from a certain phase of the process a large number of images can be acquired and integrated. This method increases the collected statistics and minimizes the error. An improvement of the signal to noise ratio (SNR) is realized and can be used either to enhance the contrast or to make a higher time resolution available. The best time resolution which was realized at NEUTROGRAPH was $100 \mu s$ (chapter 6.1.2). This is about the limit when NEUTROGRAPH'S standard scintillator (the NDg screen from [AST]) is used, because the light emission declines in only $85 \mu s$ down to 10%. With other scintillators with faster decay the time resolution can still be further enhanced.

If the experiment runs long enough to cause a degradation of the scintillator, the open beam images have to be corrected. In a few experiments data images and open beam images can be acquired alternatingly (chapters 6.1.2 and 6.1.4). This makes the correction of the open beam images unnecessary and is more precise. If this method can not be applied and if the open beam images must be interpolated, care has to be taken for the history of beam intensities (chapter 4.3.1):

In stroboscopic radiography the history of beam intensities is not represented by the recorded images. Typically a fast periodic process is investigated at a few time steps, which do not represent the complete cycle. If the period of the process is small compared to the time scale of the scintillator degradation,

5.3 Dynamic Tomography

5.3.1 Principle

Dynamic processes can be investigated not only by radiography in 2D but also in 3D by tomography. It is obvious that the time scales are different. In radiography the time resolution is identical with the exposure time. In tomography it is the time t_{tomo} , which is needed to record the projections from 0° to 180° . There are two possibilities to do the tomography:

1. **stepwise:** A stepping motor rotates the sample in single steps from the position of one projection to the next. Camera and stepping motor are synchronized, so that the camera records the images every time the motor is still. The advantage is the absence of a motion blur due to the rotation while the camera is recording an image. In contrast this method needs more time since the recording and the rotation are carried out alternatingly and because the motor has to accelerate and to decelerate for each step.

2. **continuous rotation:** Instead of a stepwise rotation the motor rotates the object continuously with a precisely known speed. The camera is not directly synchronized to the rotation but triggered by a frequency generator in order to ensure a constant recording frequency. In this case the rotation and the recording are carried out at the same time, which saves time. In contrast now the images are motion blurred due to the rotation of the object. This effect depends not only on the exposure time t_{exp} and the rotation frequency ν , but also on the distance r to the rotational axis. The effect of blurring $b = 2\pi \nu r$.

In both cases additional artifacts are created by the interplay of the motion in the sample and the reconstruction algorithm. These artifacts depend on the motion speed compared to the tomography acquisition time and the motion's direction in reference to the axis of rotation. Also the type of process which is investigated influences the artifacts.

5.3.2 Application in Two-Phase Flows

At NEUTROGRAPH we aim on the visualization of the creation of water and the two-phase flow of water and air in the supply channels of a fuel cell. Therefore we made a preliminary experiment of comparable type to learn about the method and the results which can be expected. First only two, later a bundle of small steel tubes with an inner diameter of 2 mm were mounted parallel to the axis of rotation (Fig. 5.1). They were all connected via flexible tubes and a two-phase flow of water and air was forced through the system.

Now several tomographies were done with different settings. Both methods, the stepwise and the continuous rotation, were tested and the parameters rotating speed, exposure time, velocity of the two-phase flow and the number of projections were varied. In order to do a tomography for more than one time step, the object was rotated by 520° . For the time step T the projections $[p_T, p_{T+180}]$ were used to reconstruct the data.

The following settings were applied:

experiment	mode	t_{tomo} [s]	t_{exp} [ms]	projections
1	<i>stepwise</i>	40	40	181
2	<i>continuous</i>	18	15	361
3	<i>continuous</i>	9	15	181
4	<i>continuous</i>	9	5	181
(*)5	<i>continuous</i>	9	15	181

(*) A bundle of 12 tubes instead of a pair

Every experiment was carried out with several differing velocities of the two-phase flow.

Fig. 5.3 - 5.5 show tomographies with different flow constants. In these experiments the motion of the fronts between the two phases cause the creation of helical artifacts. Due to the sample's rotation of 180°, the helices describe a rotation of 180°. The artifacts are very disturbing

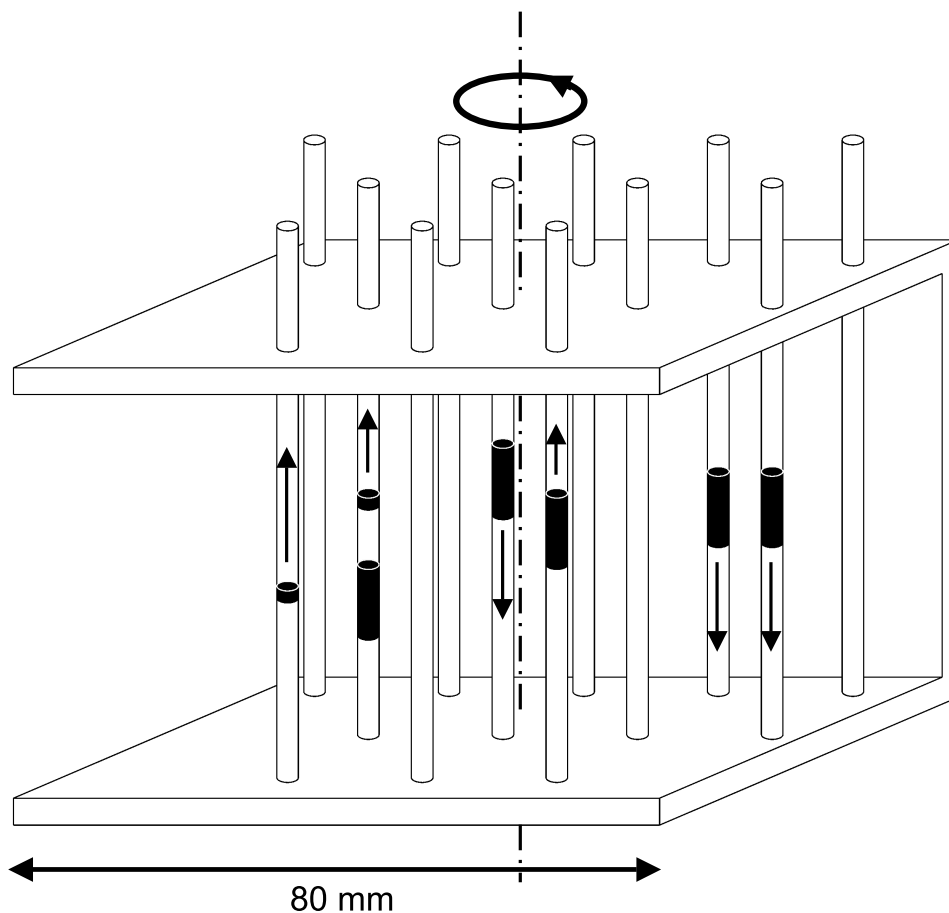


Figure 5.1: Set-up of experiment on dynamic tomography: A bundle of small aluminum tubes with a two-phase flow of water and air running through it.

in experiments where the shape of the object has to be known very precisely. In contrast, when only the phases in a two-phase flow shall be detected, the artifacts even contain helpful information about the process:

- In the reconstruction the length of the water sections equals the real length of the water sections plus the travel length of the phase fronts.
- The average value of the flow constant can be determined from the length of the helices and the acquisition time t_{tomo} . When the motion of the phase fronts is not constant, the speed can be determined from the helices' pitch for every moment within the acquisition period with a time resolution much better than t_{tomo} .
- From the orientation of the helices and the rotation of the sample one knows the direction of the motion. In our experiment, the sample rotated clockwise, which means that the vector of rotation pointed downwards. In Fig. it becomes clear that a motion parallel to the vector of rotation creates a right-handed helix, a motion antiparallel to the vector of rotation creates a left-handed helix.



Figure 5.2: Tomography with stepwise rotation: 40 sec acquisition time, 180 projections.

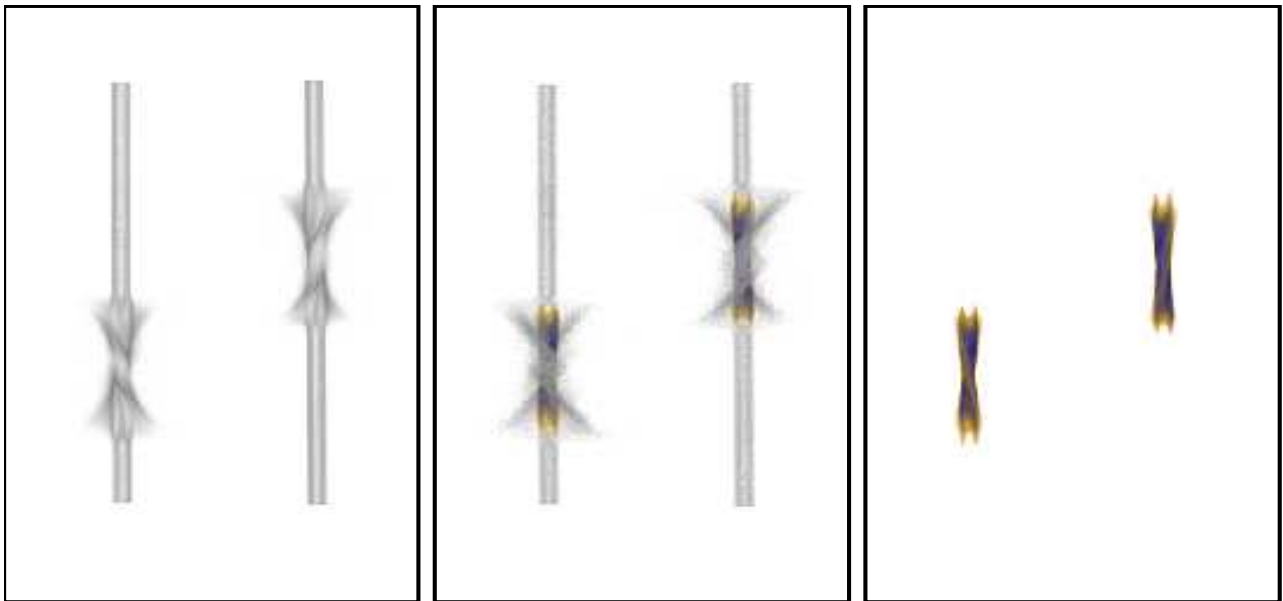


Figure 5.3: *Tomography with stepwise rotation: 40 sec acquisition time, 180 projections.*

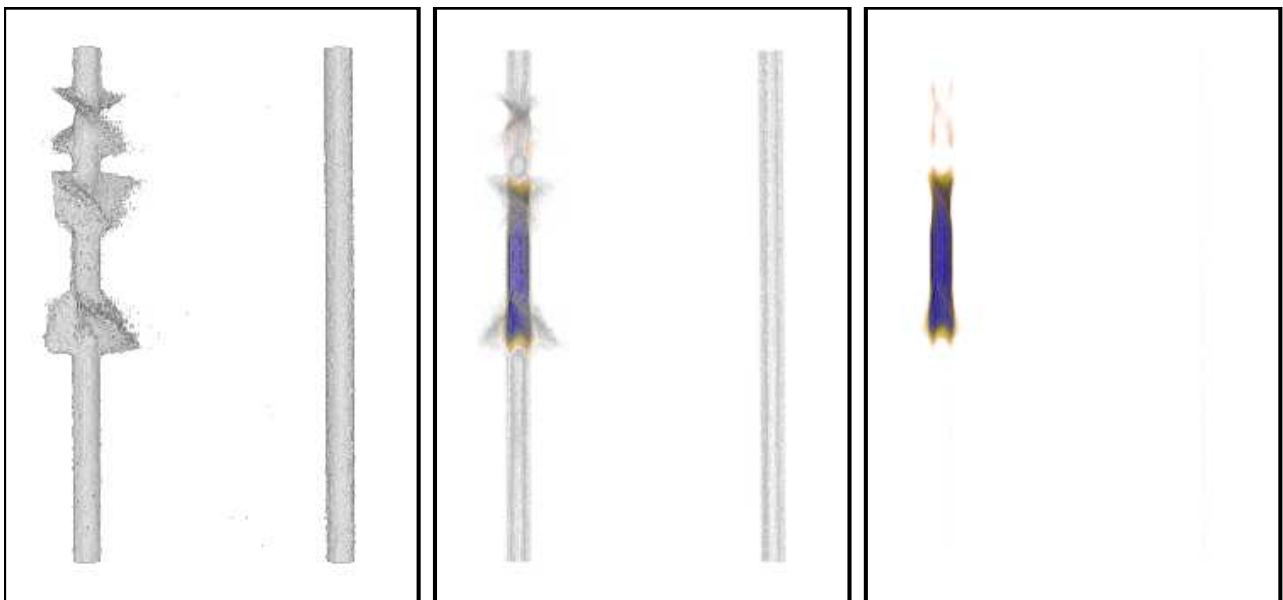


Figure 5.4: *Tomography with continuous rotation: 9 sec acquisition time, 180 projections.*

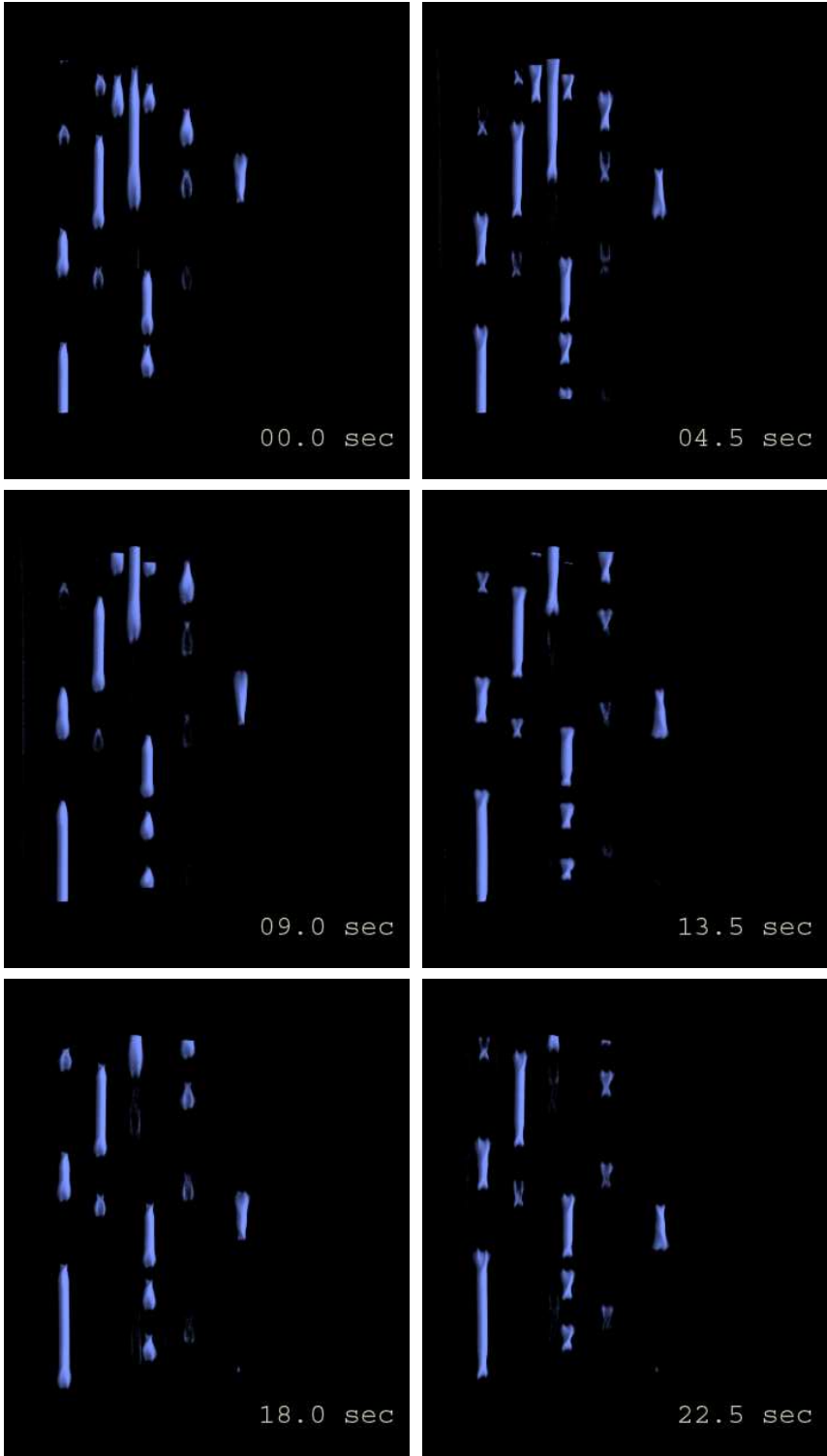


Figure 5.5: Tomography with continuous rotation: 9 sec acquisition time, 180 projections.

5.3.3 Further Improvements

In the experiments described in the previous section the fastest tomography was done in 9 seconds. With the actual existing hardware the limit for a tomography is 7.2 s, which is due to the speed limit of the rotational stage. Therefore we plan to acquire a new motor which can rotate the sample with a speed of 180° s^{-1} .

Further restrictions are the neutron statistics and the number of projections. The camera which was used for these experiments, a PCO Sensicam (chapter 3.4.2), has a readout time of 33 ms. The maximum frame rate is 30 Hz for exposure times less than 1 ms and decreases with increasing exposure times. Assuming a speed of rotation of 180° s^{-1} , only 30 projections could be recorded in the best case. With respect to the Nyquist condition

$$M \geq 2 \pi r_{max} \nu_{max} \quad , \quad (5.1)$$

where M is the minimum number of projections needed to resolve the spatial frequency ν_{max} at the maximum radius r_{max} [Schneid01], a number of 30 projections is much too small. Assuming a radius $r_{max} = 15 \text{ mm}$ and a spatial frequency $\nu_{max} = 2 \text{ mm}^{-1}$, a number of projections $M = 188$ is required. In the case of neutron statistics only a fraction of neutrons in the range of a few percent could be used.

The solution to these problems is a high-speed camera. There are cameras available with a frame rate of more than 1000 Hz at VGA resolution (640 x 480 pixels) and interframing times in the range of nanoseconds. With such a camera a tomography could be done in 1 s with up to 1000 projections and the exploitation of more than 99.9% of the neutrons. The following table compares the properties of such a tomography with the fastest ones from the previous section:

	with new hardw.	experim. 3	experim. 4
tomography acquisition time t_{tomo} [s]	1	9	9
number of projections	1000	181	181
exposure time t_{exp} [ms]	1	15	5
total exposure time [s]	1	2.715	0.905
smear ($^\circ$ per exposure)	0.18°	0.3°	0.1°

The line **smear** shows the angles, by which the sample is rotated during the acquisition of one projection. It tells something about the image quality of one projection.

6. Experiment Highlights

6.1 Combustion Processes

As it is well known, serious problems arise with the burning of fossil fuels in combustion engines: the sources become fewer and fewer and the concentration of the greenhouse gas CO_2 in the atmosphere rises dramatically. In addition the price for crude oil increased tremendously during the last few years, with bad effects on the world economy. Therefore it is obvious that there is a need for making the combustion process in engines more efficient in order to save fuel and money and to make fuel reserves longer lasting.

Since the invention of the petrol and diesel engines the technique of the internal combustion engine has extremely been improved and the efficiency went up. However this is far from being sufficient. But the development has reached a point where further progress can only be realized with high effort and new research techniques.

The crucial point for the efficiency of the combustion is the fuel density and distribution inside the combustion chamber and the size of the fuel droplets. This is true for both types of engines, motors with a carburetor or a direct injection. Today, also in petrol motors the direct injection plays a more and more important role since the fuel distribution can be better controlled by an injection. With a sophisticated interplay of the piston shape, the injection time and the injection geometry with the parameters pressure, nozzle shape and size, number and direction of jets and in the case of petrol engines the position of the spark plug, the combustion can be manipulated. Much is known about the optimal parameters. However the controlling of all these parameters is very difficult. A direct observation of the processes would be extremely helpful.

Several optical and laser spectroscopical methods have been developed in order to make the processes visible and they have become powerful tools. But they all lack the ability to investigate a standard and unmodified engine. For access to the combustion with visible methods windows have to be introduced into the cylinder wall or the piston with tremendous effects on the processes themselves. The different surfaces and heat transfer properties influence the combustion. Furthermore the investigations can only be done in a small period after the start

of the engine because the windows become quickly opaque. Also the motors must not run under load since the glass parts can not resist the higher thermomechanical strain. But the behavior of the combustion differs significantly under all these different conditions. Hence the obtained results are representative only for a small spectrum of conditions and are not the same as they would be for a standard engine.

The idea arose to complement the optical methods with time resolving neutron radiography. Neutrons should easily penetrate the motor and make the fuel density distribution visible. No glass windows would have to be introduced. Even though neutron radiography can not provide the same sharpness as optical images, neutron imaging could verify the validity of the results from optical methods for unmodified engines.

In order to develop the measurement methods, two different projects were carried out in parallel. One was the visualization of the fuel spray with a fuel injector in a simple aluminum container, the second one the investigation of running combustion engines.

6.1.1 First Calculations

The aim of the project is the visualization of the fuel's density distribution inside the combustion chamber. Even before NEUTROGRAPH was set up and details of the detector system were known, a calculation regarding neutron statistics should estimate the measuring time needed for the visualization of a 10% variance in the fuel's density distribution within a cube of 1 cm^3 . With μ being the macroscopic total attenuation cross section, the variation of μ inside a resolution volume dV calculates to

$$\frac{d\mu}{\mu} = \frac{1}{dx^2 \cdot \mu} \sqrt{\frac{e^{\mu \cdot D}}{\Phi \cdot t}} \quad , \quad (6.1)$$

where dx is the size of the resolution volume dV , D the thickness of the material, Φ the neutron flux and t the measuring time [Ferg03].

The following properties were assumed:

engine of 74 kW at 2500 rpm at half load

	petrol	diesel
fuel injection / cycle and cylinder:	50 mm^3	30 mm^3
volume of comb. chamber at max. compression:	43 cm^3	26 cm^3
diameter of combustion chamber:	8 cm	8 cm
H-content of fuel:	$3.2 \times 10^{22} \text{ cm}^{-3}$	$3.9 \times 10^{22} \text{ cm}^{-3}$
macrosc. tot. atten. cross section of liq. fuel:	5.5 cm^{-1}	6.6 cm^{-1}
attenuation of therm. n by homog. fuel distrib.:	4.5 %	5.9 %
attenuation of therm. n by motor block:	40 – 50 %	40 – 50 %

With all these properties, a flux $\Phi_{50\%} = 1.5 \times 10^9 n \text{ cm}^{-2} \text{ s}^{-1}$, $dx = 1 \text{ cm}$ and (6.1) solved for the exposure time t , one calculates:

$$t_{\text{petrol}} = 1.7 \text{ ms} \quad \text{and} \quad t_{\text{diesel}} = 1.2 \text{ ms} \quad (6.2)$$

It is clear that this exposure time is too long and stroboscopic imaging has to be applied in order to acquire an image which is not motion blurred. With l being the length of the piston stroke and ν the rotating speed, the velocity of the piston calculates to

$$v = \frac{d}{dt} \frac{l}{2} \sin(2\pi\nu t) = l\pi\nu \cos(2\pi\nu t) \quad , \quad (6.3)$$

where the maximum speed

$$v_{\text{max}} = l\pi\nu \quad . \quad (6.4)$$

Assuming a stroke $l = 80 \text{ mm}$ and a rotating speed $\nu = 41.7 \text{ Hz}$ (2500 rpm) and demanding that the motion blur s of the piston's movement does not exceed 1 mm , the requested exposure time is

$$t = \frac{v_{\text{max}}}{s} \approx 100 \mu\text{s} \quad . \quad (6.5)$$

To gain the requested neutron statistic, $n_{\text{petrol}} = 1640$ and $n_{\text{diesel}} = 1160$ respectively of single stroboscopic exposures have to be integrated. To detect a 10 % variance inside a cube of 1 m^3 , these values have to be multiplied by 10^4 .

6.1.2 Injector Nozzle

Motivation

The motivation for experiments on the fuel injector was to become experienced with the measurement techniques needed for experiments on a running combustion engine and to estimate, how much exposures should be taken for the visualization of the injection process. These tests with the injector nozzle were important, since a running combustion engine inside a reactor building is a bit delicate because of a certain danger of fire, the production of probably activated exhaust gases, the activation of the motor itself and the noise which was annoying to all experimentalists around NEUTROGRAPH. Therefore it was important to demonstrate the feasibility of this kind of experiment and to learn as much as possible in order to reduce the run time of the combustion engines.

Setup

The experiment was done in collaboration with J. Brunner [Antares]. For the experiments a common rail diesel injector from [BOSCH] was used (Fig. 6.1). The nozzle ejected a single jet. For security reasons a special test oil was used, which has the same viscosity as diesel, but an increased fire point. The exact composition of the test oil is not known, however the absorption cross section for neutrons was measured to be only 5% lower than the cross section of diesel [Eng04].

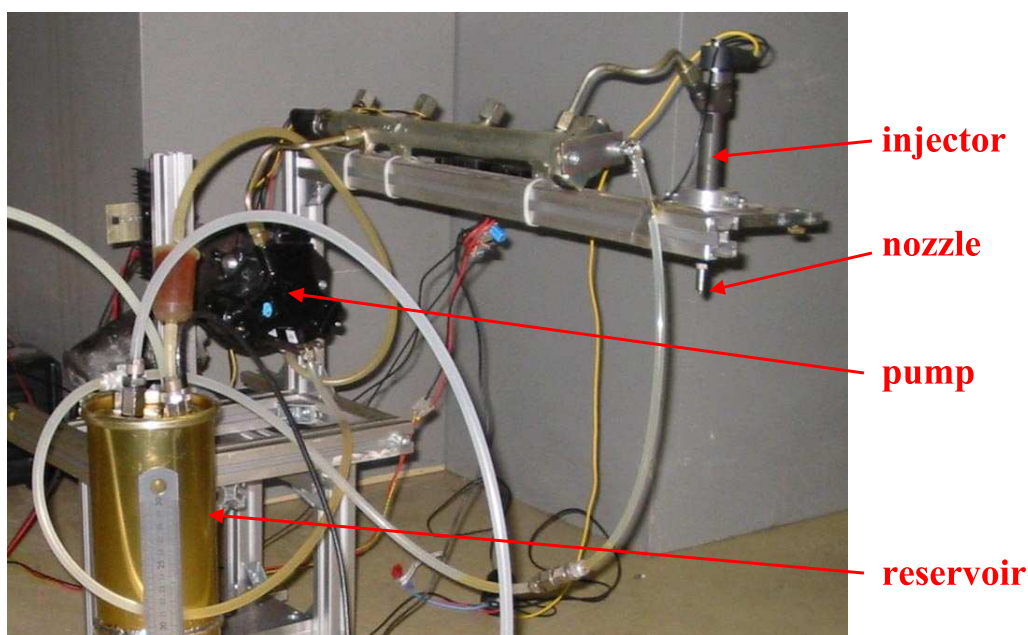


Figure 6.1: *Common Rail Diesel Injector*

The injector was installed inside a box with aluminium walls of 5 mm thickness. The box was 400 mm wide and large and 600 mm high. In the first experimental run the injector was positioned in the middle of the top wall that is in a distance of 200 mm to the detector which was placed directly behind the box (Fig. 6.2). This was done to prevent the creation of droplets on the wall due to the injection. In order to increase the spatial resolution and to have comparable results to the last experiments described in

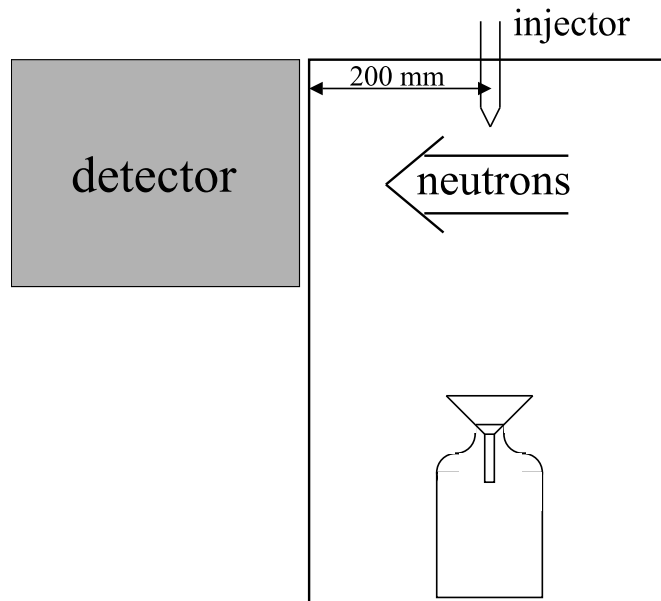


Figure 6.2: *Experimental Set-Up*

A TTL signal triggered a simple electronic to create a pulse of 80 V for about $800\text{ }\mu\text{s}$, which forced a piezo to open the injector nozzle. The same TTL signal triggered with a variable delay the camera. From preliminary optical tests at [NEUTRA] it was already known that the delay between the trigger signal and the oil injection was about 1 ms . Due to the very low light level at less than 1 ms and the extremely weak attenuation signal, stroboscopic radiography had to be applied.

Experiment 1

The aim of this first experiment was to show the feasibility of visualizing the injection process with a time resolution of $100\text{ }\mu\text{s}$. This is approximately the upper limit for the time resolution, since the light emission of the scintillator decays in $85\text{ }\mu\text{s}$ to 10% (3.4.1, ??). In order to optimize the light efficiency of the detector system, a short optical path of 700 mm was chosen and a 2×2 binning of the pixels applied.

where x is the number of the delay, n the block number and

$$i_n = \sum_{k=1}^{1000} image_{k,n} \quad \text{and} \quad o_n = \sum_{k=1}^{1000} open_{k,n} \quad (6.7)$$

The result are shown in Fig. 6.3.

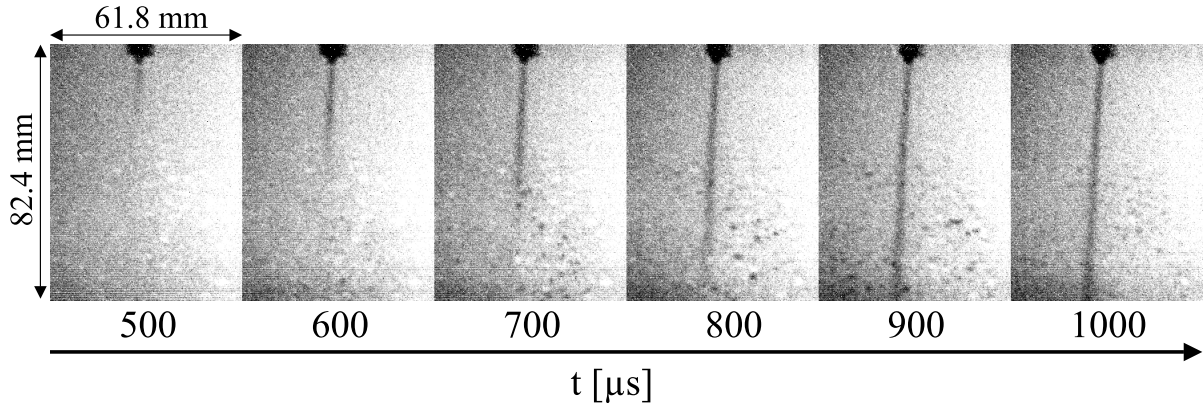


Figure 6.3: Diesel injection at 6 different time steps: The grey values are rescaled to a small band of about 1.5%

Clearly visible is the nozzle on top of the images and the jet. Even though each image is the sum of 5000 exposures, the image quality is very low and noisy. Furthermore the images show droplets on the box wall and an inhomogeneous background. The inhomogeneity comes from the linear interpolation of the open beam images, while in the time of 20 min in between two sets of open beam images the exponential behavior of the scintillator degradation is clearly visible (see 4.3.1. All these systematic errors can be minimized as it was done in the following experiment.

The attenuation signal of the oil jet is estimated to typically 0.25 ‰ and 0.5 ‰ in the maximum. To determine the noise in the images, small areas from the background were extracted and the standard deviation calculated, which leads to a relative error of $r_{t,exp} \approx 2.8 \%$.

Regarding the errors it is clear, where all the noise comes from. With an integrated exposure time of $t_{exp} = 5000 \times 100 \mu s = 0.5 s$, an area of $257 \times 257 \mu m^2$ viewed by one pixel (with the 2×2 binning already taken into account) and a detected flux of approximately $7.5 \times 10^8 n s^{-1} cm^{-2}$, one pixel sees the number of neutrons $N \approx 2.5 \times 10^5$ with the statistical error $\sigma_N = \sqrt{N} = 500$ corresponding to the relative error $r_N = 2 \%$. In every single image the neutrons are represented by a grey value of about 8 with an read out error of $\sigma_{gv} = 1.73 gv \Rightarrow r_{gv} = 22 \%$. In respect to the number of images of 5000, the theoretical relative error is

$$r_{t,theor} = \sqrt{\frac{2 \cdot r_{gv}^2}{5 \times 10^3} + r_N^2} = 4.8 \% \quad (6.8)$$

Experiment 2

With the experience from the first measurement the second one was done. The first modification to mention is the new distance between the injector and the detector. The distance was reduced to 70 mm in order to make this experiment comparable to a new experiment on a diesel engine (see 6.1.4). Then the repetition rate of the injection was increased to 20 Hz . Certainly the oil pressure dropped down to approximately 350 bars , but the high frequency and with it the possibility of applying on chip integration was considered to be more important.

Next the number of images was increased from 5000 up to 51200, which corresponds to a total exposer time $t_{exp} = 5.12\text{ s}$. Instead of reading out after each exposure, 32 exposures were integrated on chip and then read out. This reduces the relative read out error by the same factor. New electronics, a multifunction data acquisition card *NI 6032 E* from [NI], allowed the instantaneous and automatic shift of the trigger delay for the camera. The acquisition card was controlled by a LabView VI. Now the following measurement procedure was applied:

- **delay 1:** 32 exposures on chip integrated, read out (corresponds to 1.6 s)
- **delay ob:** 32 expos. oci, read out (no injection, used for normalization)
- **delay 2:** same as with delay 1
- **delay ob:** same as before
- \vdots
- **until delay 8 + delay ob**, then restart with delay 1

After the subtraction of the dark image, every image was normalized by the next open beam image. Then for each time step all the images were integrated.

This procedure is a big improvement. The fact that each image was directly followed by an open beam image eliminates the artifacts of scintillator degradation completely, because the time of 1.6 s in between the two acquisitions is much shorter than the time scale of scintillator degradation. Also disturbing droplets on the wall are completely normalized out. Furthermore the cyclic changing of the camera delay ensures that for all time steps the scintillator has the same brightness. Otherwise the statistics would be much lower for the time step acquired as last compared to the first one. The results are shown in Fig. 6.4.

The relative error was determined in the same way as in the first experiment. Now, $r_{t,exp} = 2\text{ ‰}$. With the area of $128.5 \times 128.5\ \mu\text{m}^2$ regarded by one pixel and the integrated exposure time $t_{exp} = 5.12\text{ s}$, one pixel sees $N \approx 6.4 \times 10^5$ neutrons with the relative error $r_N = 1.3\text{ ‰}$. Due

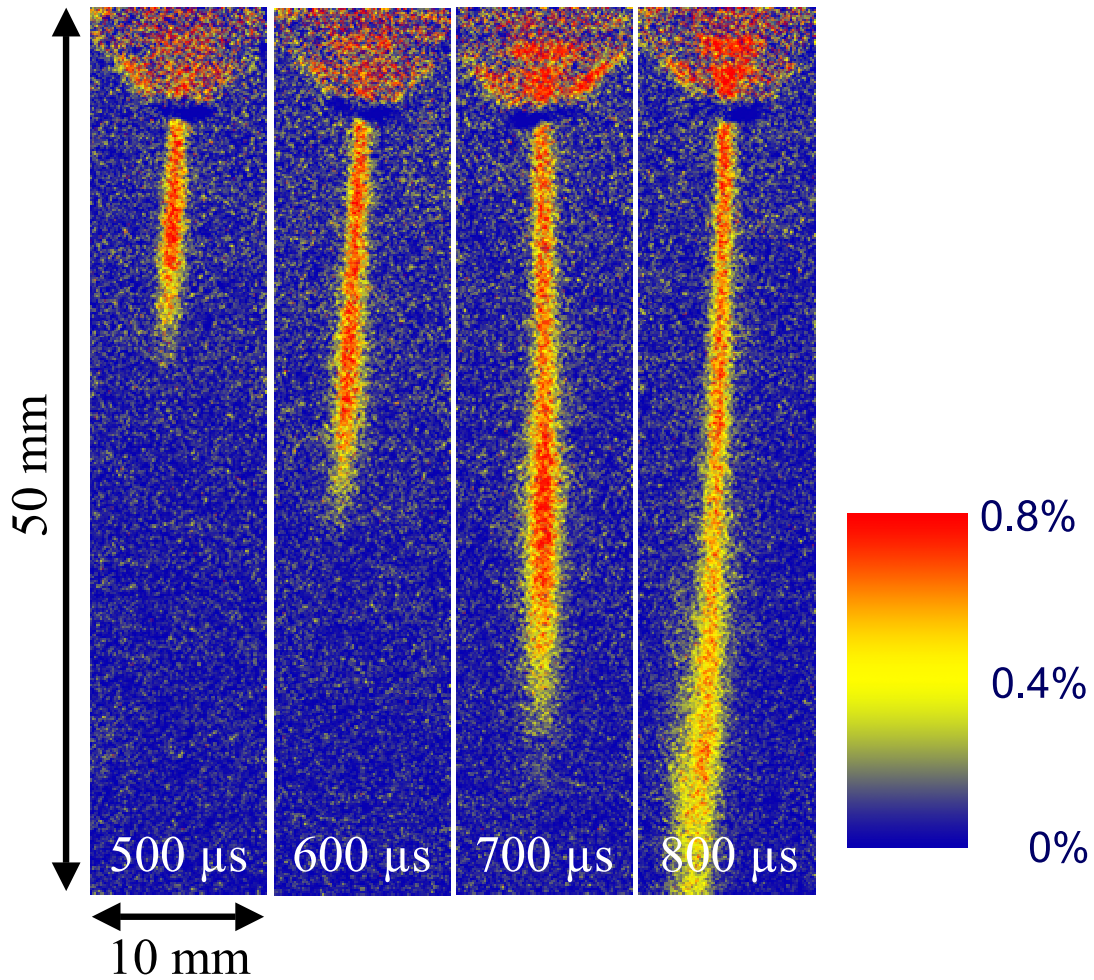


Figure 6.4: Diesel injection at 4 different time steps

to the on chip integration the relative readout error $r_{gv} = 7\%$. With these values the total relative error calculates to:

$$r_{t,theor} = \sqrt{\frac{2 \cdot r_{gv}^2}{1.6 \times 10^3} + r_N^2} = 1.3\% \quad (6.9)$$

The measured attenuation due to the jet is 0.4 – 0.8% and has almost doubled in magnitude. This is considered to be due to the lower smearing by the beam divergence due to the shorter distance.

6.1.3 Petrol Engine

As mentioned above, one crucial point for the efficiency of combustion engines is the distribution of the fuel inside the combustion chamber at the time of ignition. A first experiment on a small

6 Experiment Highlights

engine should proof this. A power generator with a small carburetor engine was acquired (Fig. 6.5). The generator itself was not of importance but very useful, because:

- the rotating speed of the system was stabilized to 3000 rpm (50 Hz)
- the engine could easily be loaded by connecting an electric heater to the generator
- the mass of the generator damped the vibrations of the engine

The engine (Fig. 6.5) had the following properties:

- 1 cylinder
- most parts around the combustion chamber were made out of aluminum (transparent to neutrons), only the inner wall was made out of steel
- power of approximately 2 kW
- 156 cm^3 cubic capacity
- 65 mm diameter
- compression rate of approximately 10
- consumption of $0.8 - 1.1\text{ l h}^{-1}$ depending on the load

The engine was set up inside the casemate directly in front of the beam window with the crankshaft parallel to the beam. A standard KF-flange was soldered to the exhaust for a simple connection to the reactors waste air system via a tombac tube of 5 m . This metal tube was sufficient for cooling the exhaust gases down. A pressure sensor controlled that the running engine was not pumping too much gas into the waste air system. In cases where this happened a simple relay closed a short circuit bypassing the spark plug, which stopped quickly the motor. The same could be done manually by a switch from outside the casemate.

The running motor was investigated with stroboscopic radiography. A light barrier and a small wing mounted to a ventilator, which was directly connected to the crankshaft, triggered the camera with a variable delay. After each exposure of 1 ms the image was read out. From each time step a number of images was taken and after the dark correction integrated. In this way a whole cycle was imaged and a movie created out of this data. The same electronics which was used for the injector experiment controlled the delay of the camera trigger and shifted it after each exposure by 1 ms to the next time step.



Figure 6.5: Power generator with carburetor engine

With the properties above the gasoline was expected to attenuate the beam intensity by 0.25 % when expanded and by 2.5 % when compressed. As first step the idea was not to visualize the 10 % variance of the attenuation signal within 1 cm^3 (an effect of 0.7 ‰), but to make the difference of 2.25 % between the phases of compression and expansion visible.

For these measurements 30 exposures of 1 ms exposure time were acquired from each time step and no on chip integration applied. This long single exposure times but the low integrated exposure time were preferred in order to keep the measuring time and with it the scintillator degradation low. To overcome the relative error of $r = 3 \%$ of each pixel, the signal from 100 pixels were added, which decreased the relative error down to $r = 0.3 \%$. A comparison of the integrated grey values inside the box (Fig. 6.7) from each time step should reveal the effect from the gasoline.

During these experiments it was recognized that the beam intensity and the light level of the camera fluctuate by 1 – 2 % (chapter 4). To suppress these fluctuations, small regions where the intensity was considered to be constant were monitored. Here the fluctuations should be measurable and the signal be used to normalize the images. Unfortunately it became clear that the piston scatters neutrons to these regions depending on it's position and the curves are not

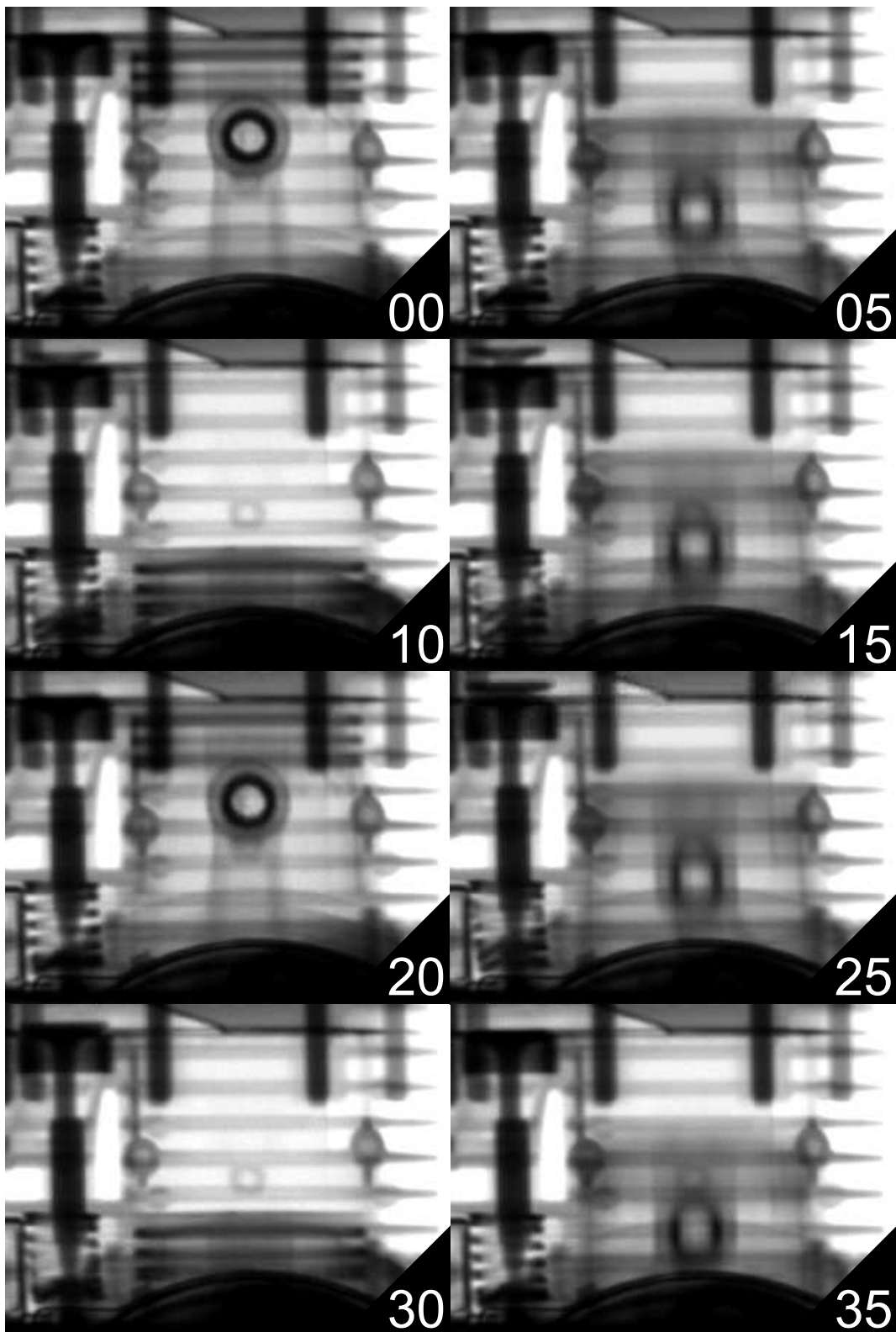


Figure 6.6: Radiographs of carburetor engine at different time steps [ms]: 0 ms: ignition, 5-10 ms: expansion, 15-20 ms: ejection, 25-30 ms: refilling, 35-0 ms: compression

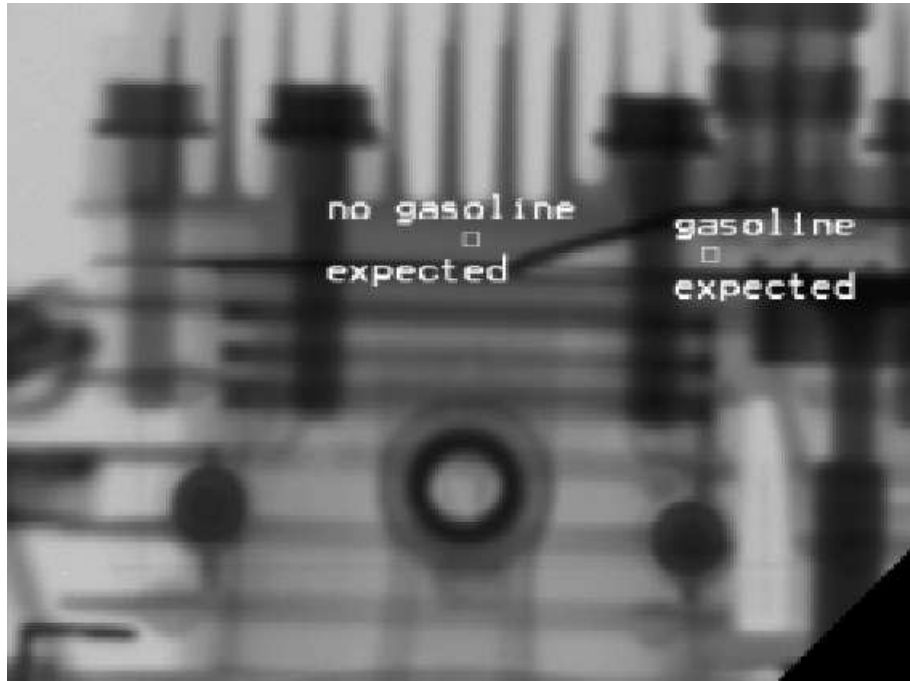


Figure 6.7: The grey values in the white boxes were integrated and compared

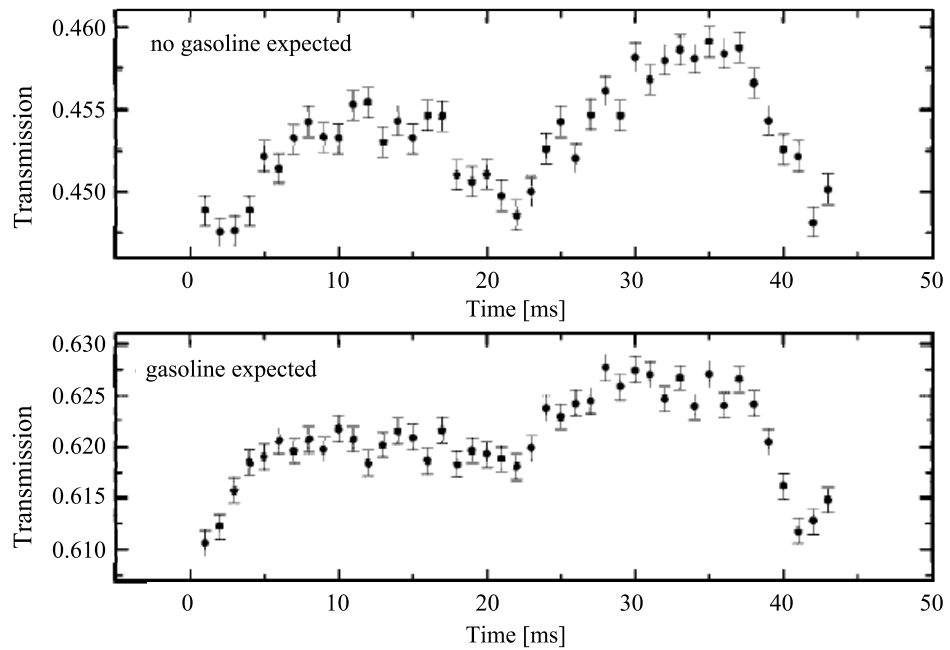


Figure 6.8: Integrated grey values from the boxes shown in Fig. 6.7

independent from the motor cycle. Fig. 6.8 displays typical results.

Much effort was put into installations which were dedicated to reduce the influence by the piston's position to these regions, all without success. The fuel was not detected. Encouraged by the excellent results from the injector experiments, it was decided to launch a new experiment on a diesel engine instead (6.1.4).

6.1.4 Diesel Engine

The reason for this experiment was the problem with the detection of variances over time and the consideration that the structure of a fuel injection (a structure in space) should be better detectable. For the same reasons as in (6.1.3), the new diesel motor was bought together with a power generator (Fig. 6.9). The motor had the following properties:

- 1 cylinder
- most parts around the combustion chamber were made out of aluminum
- power of 6.9 kW
- 412 cm^3 cubic capacity
- $\sim 80\text{ mm}$ diameter
- consumption of $0.5 - 1.7\text{ l h}^{-1}$ depending on the load
- $5.6 - 18.9\text{ mm}^3$ per injection depending on the load
- injector nozzle with 4 channels

For mechanical reasons the system was placed inside the casemate with the crankshaft perpendicular to the neutron beam. The air filter at the inlet and its plastic box were removed since they were in a direct line with the injector nozzle and would hide them. Also the exhaust was replaced by new tube and a KF-flange was soldered to it. Again the exhaust gases went via a tombac tube to the reactor's air waste system and the same pressure sensor monitored the pressure of the incoming gases. In case of a high pressure or an emergency an electric valve could be closed from outside the casemate which interrupted the fuel supply. It took then about 10 s to switch off the engine.

As in the experiment on the petrol engine the camera was synchronized to the engine. The electrical current created by the power generator induced a signal in a simple wire loop. This signal was used for the trigger. Since 2 trigger pulses were created during one motor cycle, a small electronic suppressed every 2^{nd} pulse [Eng04].

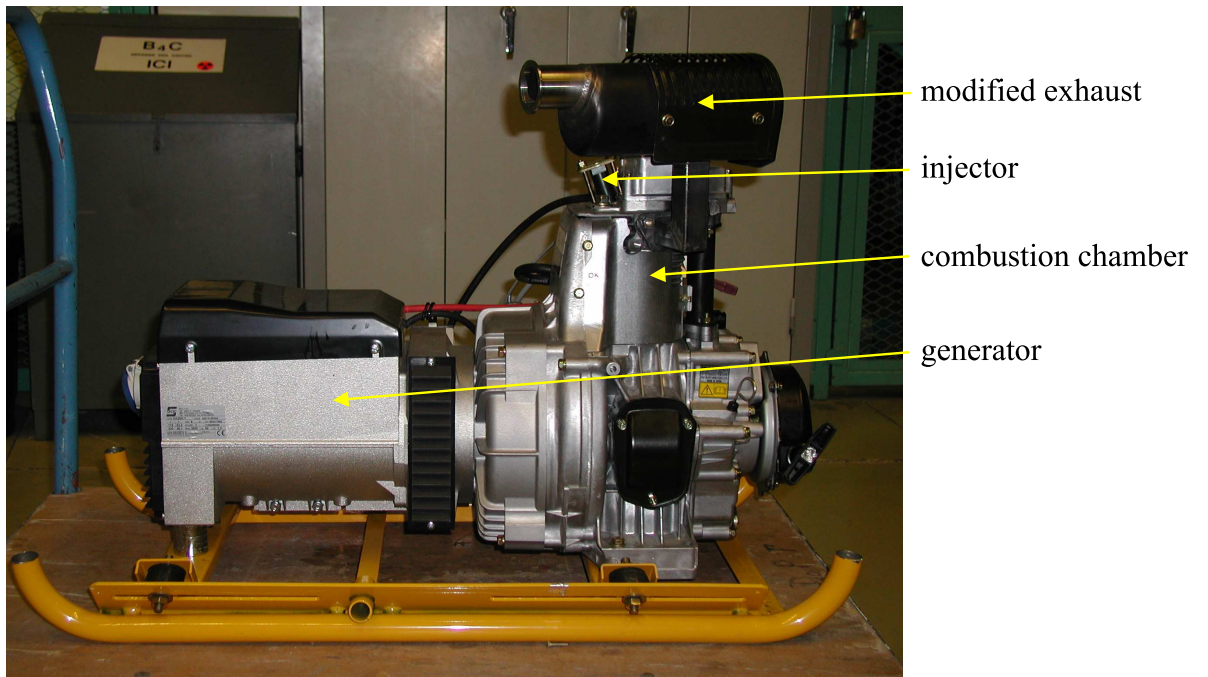


Figure 6.9: Power generator with diesel engine

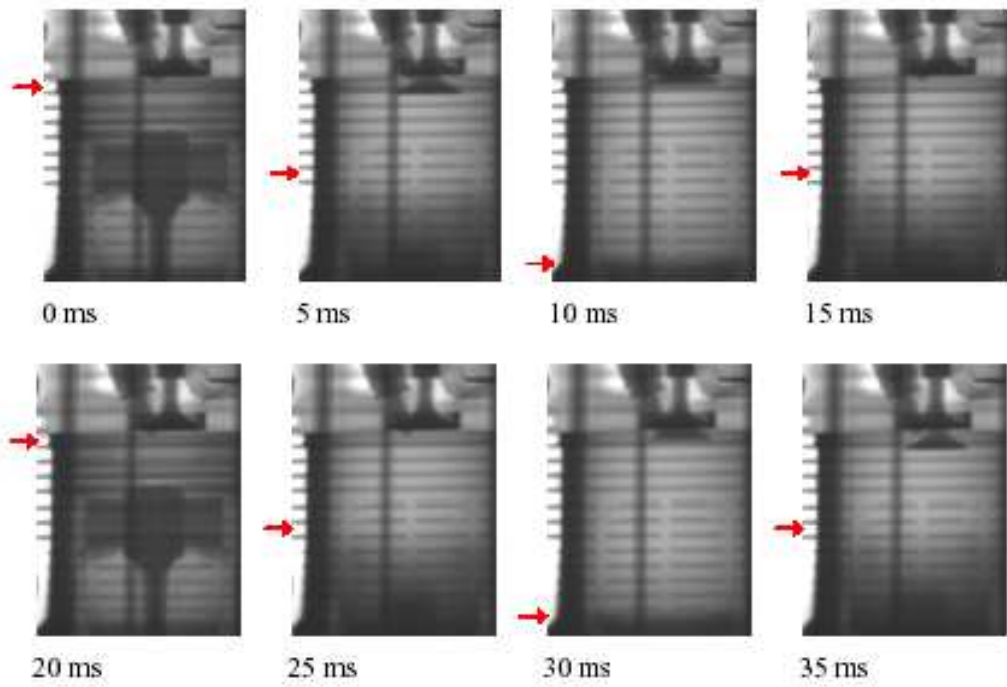


Figure 6.10: Radiographs of diesel engine at different time steps:

Measurement 1

In a first measurement the complete cycle was imaged (Fig. 6.10). The aim was not to detect the fuel injection but to show the system was running. The images show the motor structure with differences in beam attenuation of typically 30 % and a neutron transmission of about 25 % around the injector nozzle, where the diesel jets should be detected.

Measurement 2

In the next experiment the injection was searched at several time steps around the estimated time of injection. In diesel engines the injection typically takes place at an crank angle of $23^\circ \pm 1^\circ$ before the top dead center (TDC), where the piston is in the top position [Eng04]. It was assumed to be true also for this engine. All efforts to get detailed information from the manufacturer failed. Under load the engine worked unstable and produced a lot of vibrations. It was decided not to load the engine in order to prevent a blurring of the images, even though the injected volume and with it the expected attenuation signal became much lower

For each time step a number of 10^4 exposures of $500 \mu s$ single exposure time yielded an integrated exposure time of $5 s$ compared to $0.5 s$ in the first injector experiment 6.1.2. However the injection could not be detected. Since the nozzle produces 4 jets instead of 1 with a total injected volume of only $0.5 mm^3$, these jets were considered to be very fine compared to the jet in the injector experiments. The acquired images were still too blurry to detect a small structure. A next effort was done to increase the spatial resolution (next section).

Measurement 3

In order to reduce the image blurring due to the beam divergence, the scintillator was now mounted directly on the motor instead of being mounted to the front of the detector box (Fig. 6.11). This reduced the distance between the injection and the scintillator from $200 mm$ down to $70 mm$ and with it the spatial resolution of the beam geometry by a factor of 3. To prevent the image created on the scintillator from being disturbed by surrounding light, the light inside the casemate had to be switched off.

With 25600 exposures of $250 \mu s$ per time step the time resolution was doubled and the motion blurring reduced as well as the integrated exposure time increased to $6.4 s$ compared to $5 s$ in the previous measurement. With the typical neutron transmission of 25 %, each pixel detected now a number of about 5.8×10^5 neutrons on a square of $190 \times 190 \mu m^2$ which results in a relative error of $r_N = 1.3 \%$. In order to reduce the read out noise of the camera, 64 exposures were integrated on chip before the image was read out. In this experiment on chip integration

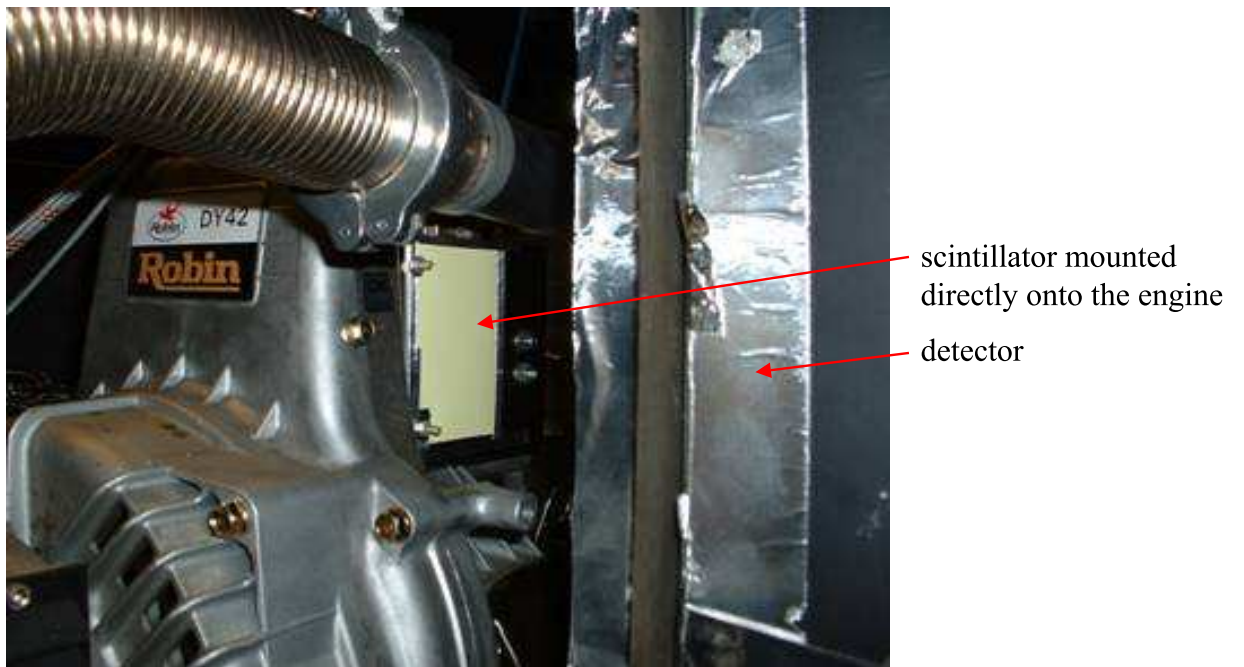


Figure 6.11: Modified set-up:

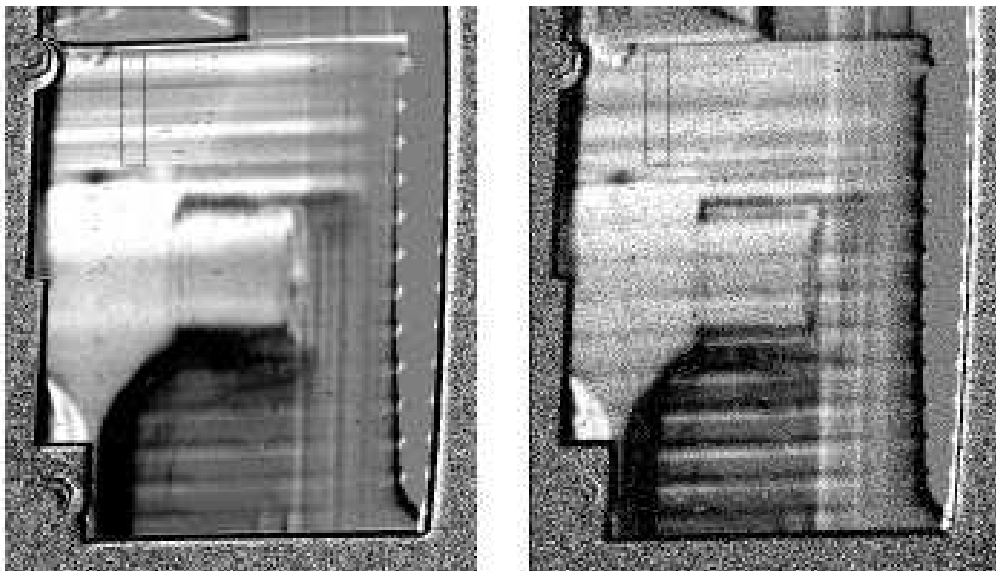


Figure 6.12: Image normalization

6 Experiment Highlights

was possible, because the ratio of the exposure time and the time the camera had to wait for the next exposure was 160 : 1. With the on chip integration of 64 exposures the relative readout error $r_{gv} = 6\%$. The total error is:

$$r_{t,theor} = \sqrt{\frac{2 \cdot r_{gv}^2}{400} + r_N^2} = 1.4\% \quad (6.10)$$

Not the complete motor cycle was investigated but a few time steps around the time of injection, 23° crank angle before TDC, a few time steps at 23° behind TDC and a few time steps half a motor cycle after the time of injection. At all these three crank angles the piston is in the same position.

The structure of the cooling ribs and other parts of the motor were considered to make the fuel jet undetectable. While in the experiments on the fuel injector the contrast of the images was increased by rescaling the grey values on a small band of a few percent, this is not possible with the inhomogeneous background in the motor experiments. Therefore it was tried to eliminate the structure. To suppress the motor structure, the images at the time of fuel injection were divided by images of same piston position but where no injection took place (see paragraph above). Fig. 6.12 displays one typical result. The variances in the structure became much lower (Fig. 6.13), but they are still a few percent high. They could not be further suppressed because the images does not overlap perfectly. The piston at the same position in the injection image and the normalization image does not automatically mean that the motor is at the same position due to its vibrations. Shifting and rotating the images can only eliminate the motor vibrations perpendicular to the neutron beam. Vibrations parallel to the beam result in a tilt of the motor and can not be eliminated. Unfortunately these vibrations are the biggest ones. Also this effort was unrewarded and the fuel not detected.

Measurement 4

In a next try 6 wt% of Carboranes were dissolved in the diesel. Boron and in particular the isotope ^{10}B has a high absorption cross section and should enhance the contrast (chapter 6.1.5). We expected to gain 27%. Unfortunately the engine worked very unstable after a short time and stopped then completely. Fuel could not be found but the measurement was too short to know, if the contrast enhancement would have been sufficient or not. Therefore on can see sediments at the valves and when the combustion chamber was opened, also at the injector nozzle sediments were found (Fig. 6.14 , Fig. 6.15).

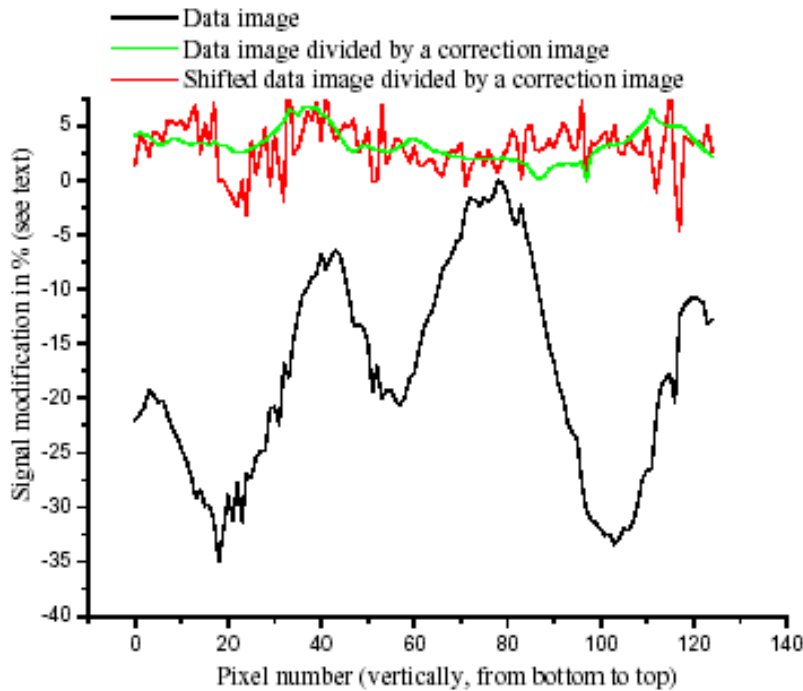


Figure 6.13: Variances of grey values along a line (graph from [Eng04])

6.1.5 Contrast agents

Since the signals to detect are extremely small and since the experiments failed so far, the application of contrast agents was considered in order to increase the contrast. The aim was to investigate combustion engines under normal conditions and the application of contrast agents would only be a compromise. But to keep the influence on the combustion process low, only a low concentration could be accepted.

As contrast agents the isotopes ^{10}B and ^{157}Gd with their absorption cross sections for thermal neutrons of 3835 barns for the boron and 2.6×10^5 barns for the gadolinium were regarded. Unfortunately they are not soluble in hydrocarbons but have to be part of a molecule which can be solved in fuel. To keep the number density of the boron / gadolinium nuclei high at a small mass concentration of the additive in the fuel, the nuclei of the contrast agents must be element of small and light molecules.

It was found that carboranes, gadolinium oxide and gadolinium(III)2-ethylhexanoate are the optimal compounds. The following table shows the factors by which the neutron attenuation increases depending on the concentration of the additive in fuel:

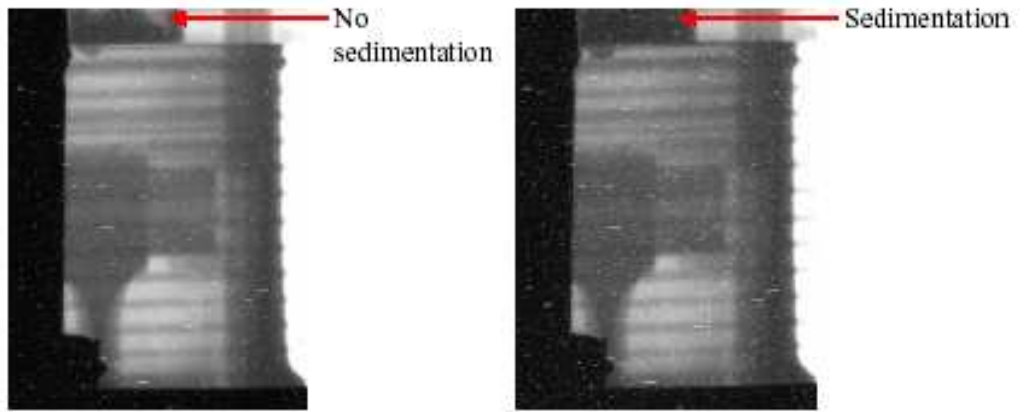


Figure 6.14: *left:* image acquired at the beginning of the experiment. *right:* image from the end of the experiment

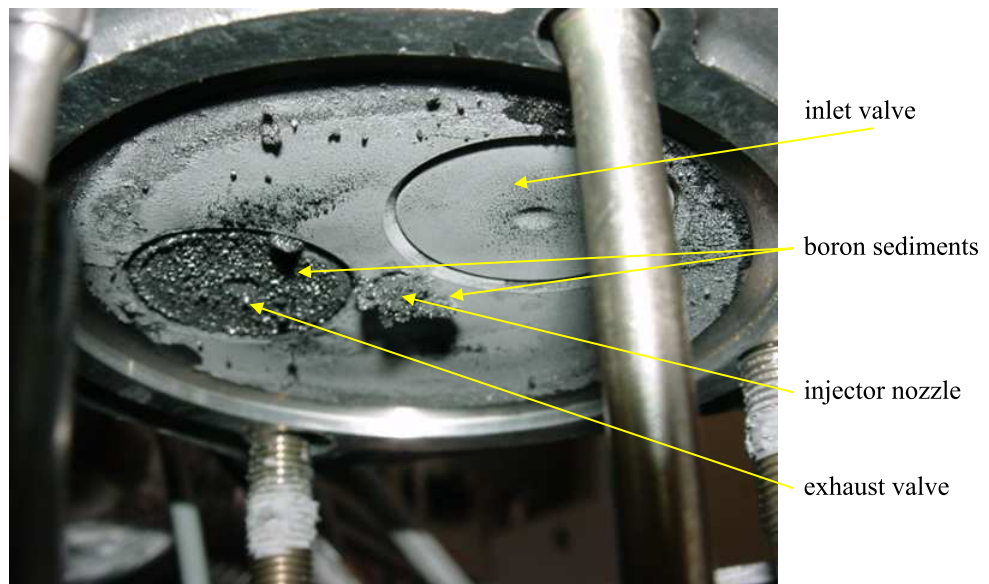


Figure 6.15: *Sediments inside the combustion chamber*

name	formula	10wt%	1wt%	0.1wt%
Carborane (^{10}B enriched)	$\text{C}_2^{10}\text{B}_{10}\text{H}_{12}$	3.2	1.2	1.02
Carborane	$\text{C}_2\text{B}_{10}\text{H}_{12}$	1.45	1.05	1.005
Gd 2-ethylhexanoate (^{157}Gd enriched)	$^{157}\text{Gd}[\text{OOCCH}(\text{C}_2\text{H}_5)\text{C}_4\text{H}_9]_3$	4.3	1.3	1.03
Gd 2-ethylhexanoate	$\text{Gd}[\text{OOCCH}(\text{C}_2\text{H}_5)\text{C}_4\text{H}_9]_3$	1.7	1.07	1.007
Gd-oxide nanopowder (^{157}Gd enriched)	$^{157}\text{Gd}_2\text{O}_3$	11.7	2.07	1.11
Gd-oxide nanopowder	Gd_2O_3	3.1	1.21	1.02

Unfortunately the improvement is only small except for the gadolinium oxide. The tracers which are applied in experiments with laser fluorescence methods are added with concentrations of a few *ppm*, here we would need 1% or more. While the carborane and the Gd 2-ethylhexanoate dissolve in hydrocarbons, the gadolinium oxide does not. But the gadolinium oxide is available from [SigmaA] as a nanopowder with a particle size of less than 80 *nm* and can be brought into the fuel as a suspension. We hoped that the suspension would be stable but we observed a deposition on the ground already after a few minutes. We had no possibility to create the suspension directly before the injection of the diesel into the motor. Therefore the Gd-oxide nanopowder was not applied in motor experiments.

In two tests we wanted to see, if the engines would run with the carboranes or the Gd 2-ethylhexanoate. In both cases a few wt% were dissolved. The petrol engine stopped after a short time as well as the diesel engine. The boron even formed sediments after a short time at the valves and the injector nozzle (chapter 6.1.4, Measurement 4).

6.1.6 Why was the fuel not detected?

The question is now, why the fuel not was detected. Here the two experiments on the petrol and the diesel engines have to be regarded separately.

Petrol Engine

The relative error $r = 0.3\%$ due to neutron and grey value statistics is sufficiently low and ten times better than necessary for the detection of an effect of 2.25%. Due to the short experiment run time of about 80 s, the scintillator degrades by only 0.6% (3.4.1), but the effect on the images are the same for every time step due to the cyclic acquisition of the images. The real problem was the fluctuations of about 2% of the neutron beam intensity and of the

camera. The measures which were taken to eliminate these fluctuations were not sufficient. The intensity in the reference points were not independent from the motor cycle as they were considered to be.

Even with a success in the experiment of chapter 6.1.3, the fuel density distribution would still not be detectable with the resolution which was aimed at due to the background structure created by the motor. All tries to normalize the motor structure out by dividing the images by other images at a different time step but same piston position failed due to the engine's vibrations (chapter 6.1.4, Measurement 3). Delocalizations of the engine can be corrected by image translation and rotation only in the two dimensions transversal to the beam axis but not longitudinal.

Diesel Engine

The experiment on the diesel engine differs from that on the petrol engine. We searched for a variance not in time but in space. It is difficult to estimate the contrast of the fuel injection since there are too many unknowns about it. It is not known if the injection is more like a jet or more like a spray. It is also not known how long the diesel is injected and how quickly it evaporates. A comparison with the injector experiment is more useful.

The diesel engine was running without load and therefore approximately 5.6 mm^3 of diesel were injected per cycle. This is about a factor 7 less than in a car engine. But it is unclear if the smaller volume is realized either by a lower flux or a shorter injection time. Then the injected volume is distributed to 4 jets instead of 1. In chapter 6.1.2 the jet attenuated the signal by $4 - 8 \%$. In the motor experiment one can assume the contrast of the jets to be at least a factor of 4 lower (number of jets) and with the smaller volume taken into account a factor of up to 28. This makes the contrast smaller than 1% , which is smaller than the theoretical relative error $r_{t,theor} = 1.4 \%$ in the last experiment without contrast agent (chapter 6.1.4, Measurement 3). To make the injection detectable the signal to noise ratio has to be multiplied at least by a factor 2, more probably a factor 10. Since the application of contrast agents can not realize this (chapter 6.1.5), the only possibility is to increase the statistics by multiplying the measurement time by 4 or 100 respectively. In chapter 6.1.4, Measurement 3 the measurement time for one single time step was 20 min . Multiplied with the factor 4(100) it is 1h20(33h30).

This is only an estimation where we assumed clear jets. Only the most dense parts of the jet would be visible with the increased statistics, no other structure. At least one jet hits the piston after a short distance of only a few mm. It can be assumed that it splashes back and adds a certain background structure to the image, which further minimizes the detectability of the jets.

A last problem is the structure of the background created by the motor structure. While in the injector experiment the background was homogenous and the contrast could be improved for a small band of grey values, this is not possible with the available data from the motor experiments due to the large variance of 25 – 30% (Fig. 6.13). The motor structure can not be eliminated by image treatment due to the reasons given in the previous section.

6.1.7 Conclusion

There is no reason why the fuel should not be detectable. Besides the injector experiments the experiment described in chapter 6.2.1 is a clue for the realizability. However, several improvements have to be done for a successful experiment.

- In order to lower the camera noise, on chip integration of the exposures has to be applied as it was already done a few times. But to prevent the collection of light while the camera is waiting for the next exposure, an additional optical shutter has to be installed. All available shutters out of the shelf are either not fast enough (iris), they can not run with 25 Hz (slit) or they do not have appropriate optical properties (electrooptical shutters).
- Also the dark current which is collected during the long period of on chip integration must be minimized by additional cooling of the camera.
- The neutron statistics has to be increased by an extension of the measuring time.
- For the visualization of the fuel's density distribution the inhomogeneous background in the images must be eliminated. Therefore all structures outside the combustion chamber have to be removed (e.g. the cooling ribs).
- The intensity fluctuations have to be normalized out. This can be done by monitoring the beam intensity independently (a beam monitor is already ordered). The intensity fluctuations of the camera can either be monitored by monitoring the camera's temperature or the cooling control electronics can be replaced and the temperature be stabilized (chapter 4.3.3).
- During the long measuring time the scintillator degrades quickly, which causes two problems: the loss of statistics due to lower light emission and the inhomogeneity of the degradation, which introduces new errors to the measurement. To prevent the loss of statistics the automatic replacement of the degraded scintillator should be considered.

The inhomogeneity of the degradation can be eliminated by the application of the interpolation algorithm described in chapter 4.3.1. A further improvement can be applied or

even has to be applied when the scintillators are replaced during the experiment: the precision of the interpolation goes up with the decrease of the time in between the acquisition of two open beam images. Unfortunately it is not possible to acquire open beam images during the measurement. Instead images can be recorded with an exposure time which is a multiple of the engine's cycle period. These images will show the engine with a lot of motion blurring. But the recorded image represents exactly the structure which causes the inhomogeneity of the scintillator degradation. The quotient of two images represents the degradation during the time in between the acquisition of these images.

6.2 Dynamic Radiography - More Experiments

6.2.1 Car engine

Fuel is not the only hydrocarbon inside a combustion engine which is interesting for a visualization. Also the behavior of lubricants and of oil which is used for the cooling of the piston is not fully understood and can be investigated with neutron radiography.

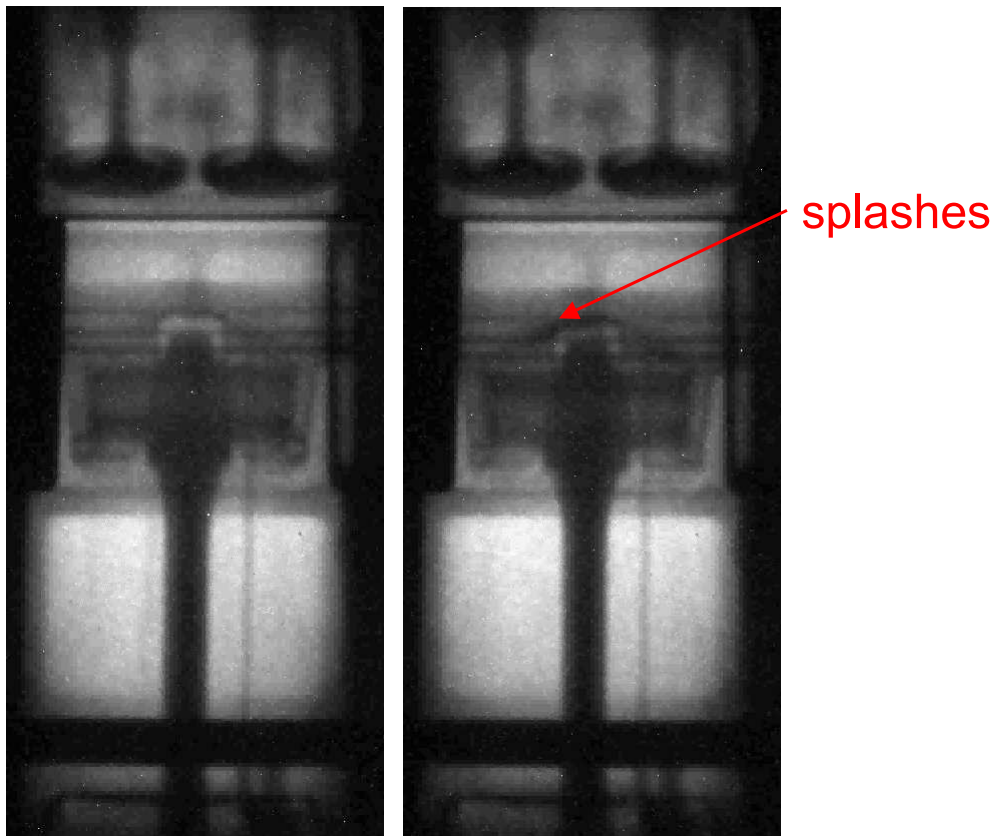


Figure 6.16: *BMW car engine: The engine was driven externally by an electric motor with 1000 rpm.*

In collaboration with the teams from [Antares] and [NEUTRA], we investigated a car engine from [BMW]. This engine did not run by combustion but was driven by an external electric motor and ran with 1000 rpm. In this engine a jet of oil is created, which hits the piston near its center. This jet is dedicated to support the cooling of the piston, which takes place where the piston is in contact with the cylinder walls and which is not sufficient in powerful motors. Fig. 6.16 shows the jet and also some splashes. Fig. 6.17 shows the whole working cycle.

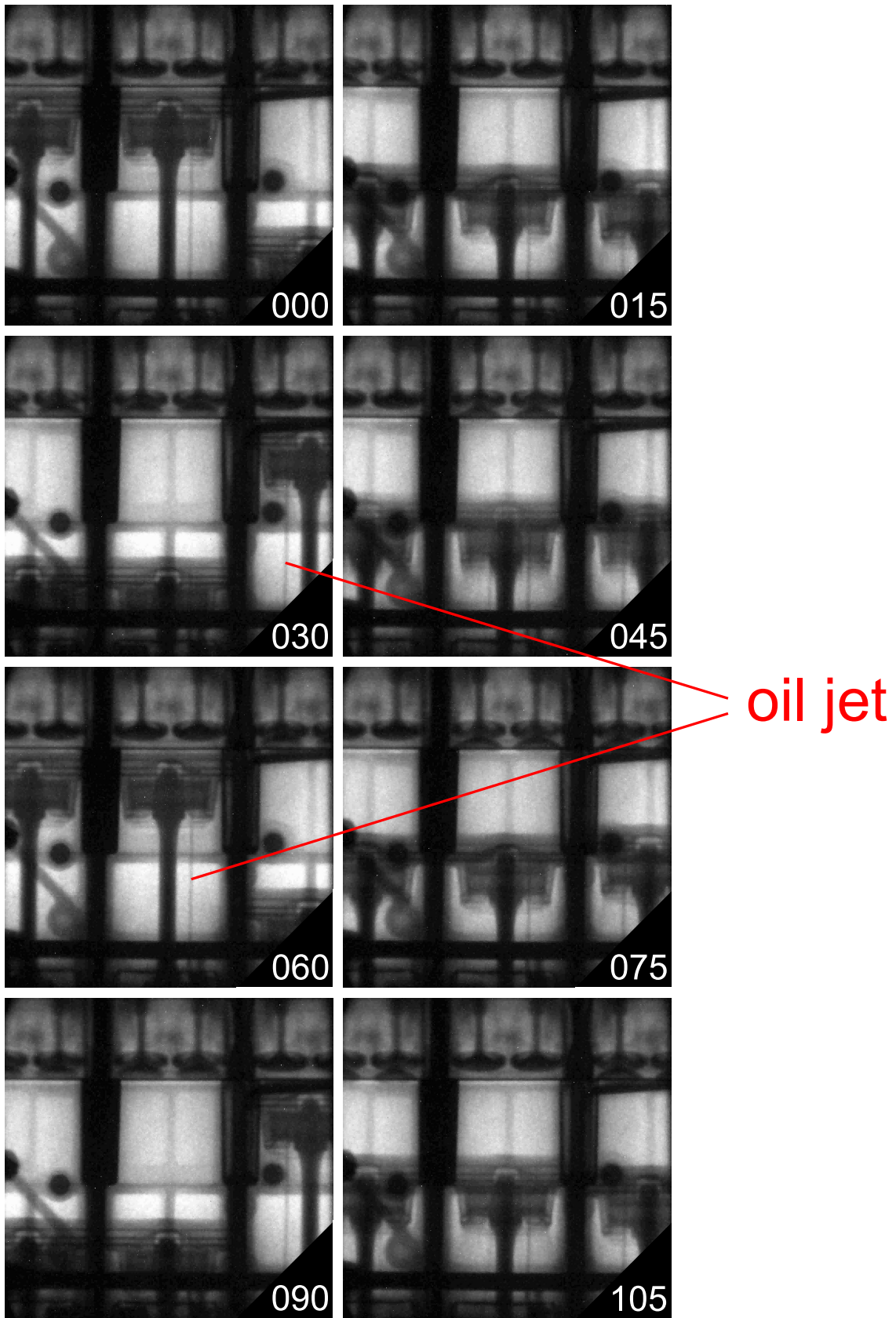


Figure 6.17: BMW car engine: The engine was driven externally by an electric motor with 1000 rpm.

6.2.2 Minichannel Heat Exchanger

With the advent of increasingly compact microchips, combined with the greater push for energy efficiency, the field of heat exchange in minichannels has been gaining in importance. Minichannels and microchannels offer not only increased compactness, but also improved heat transfer. However, a great deal of controversy still exists particularly regarding the physics of two-phase flow: heat transfer coefficient, pressure drop, critical heat flux, flow regime, and critical vapor quality.

Many previous authors have observed flow instabilities in minichannels and microchannels, particularly in low heat and low flux situations. Brutin and Tadrist [BrTa04] observed symmetric and asymmetric pressure variations in boiling pentane ($D_h=889 \mu\text{m}$). These variations were more pronounced with compressible inlet conditions and had a frequency between 4 and 40 Hz. Wen and Kenning [WenKen04] noted a similar instability-compressibility link. Peles [Pel03] observed both high and low frequency oscillations in channels of various sizes, with periods of 50 ms and 40 s respectively. The oscillations decreased with increasing inlet rigidity. Wu and Cheng [WuCh03], studied parallel silicon microchannels with a hydraulic diameter $D_h=186 \mu\text{m}$. For low heat flux, regular oscillations between liquid and bubbly flow with a period of 23 s were observed; for high heat flux, the oscillations extend the full range from liquid to superheated vapor and have a period of 53 s.

Liquid superheat is sparsely documented in minichannel heat transfer literature, however Yen et al. [Yen03], observed liquid superheats of up to 70 C over the saturation temperature before the onset of boiling. This effect was dependent on the mass flow rate and the boiling number. At NEUTROGRAPH we aimed at the visualization of the flow of liquid and vapor in a steel pipe during liquid and two-phase flow. The experiments [Os04] have been performed in a collaboration with the Commissariat à l'Énergie Atomique [CEA].

The flow apparatus consisted of a vertically mounted stainless steel pipe and is sketched in Fig. 6.18. The pipe had an inner diameter of 1.2 mm and an outer diameter of 2.0 mm. The length of the pipe was 240 mm and 174 mm of it was electrically heated by Joule heating. The outer wall temperature of the un-insulated pipe was measured by three type J thermocouples welded to the pipe wall. The ambient temperature was measured with a type K thermocouple to verify that it remains constant. The temperature of the thermocouples were recorded at 1 Hz by a logger. Pentane was forced upwards through the pipe with a syringe pump providing a constant flow rate. The pentane was subcooled at the inlet, having entered at ambient temperature. The pipe was not insulated in order to minimize the obstruction of the flux of neutrons through the test section.

The processes were investigated with high-speed radiography. In order to maximize the frame

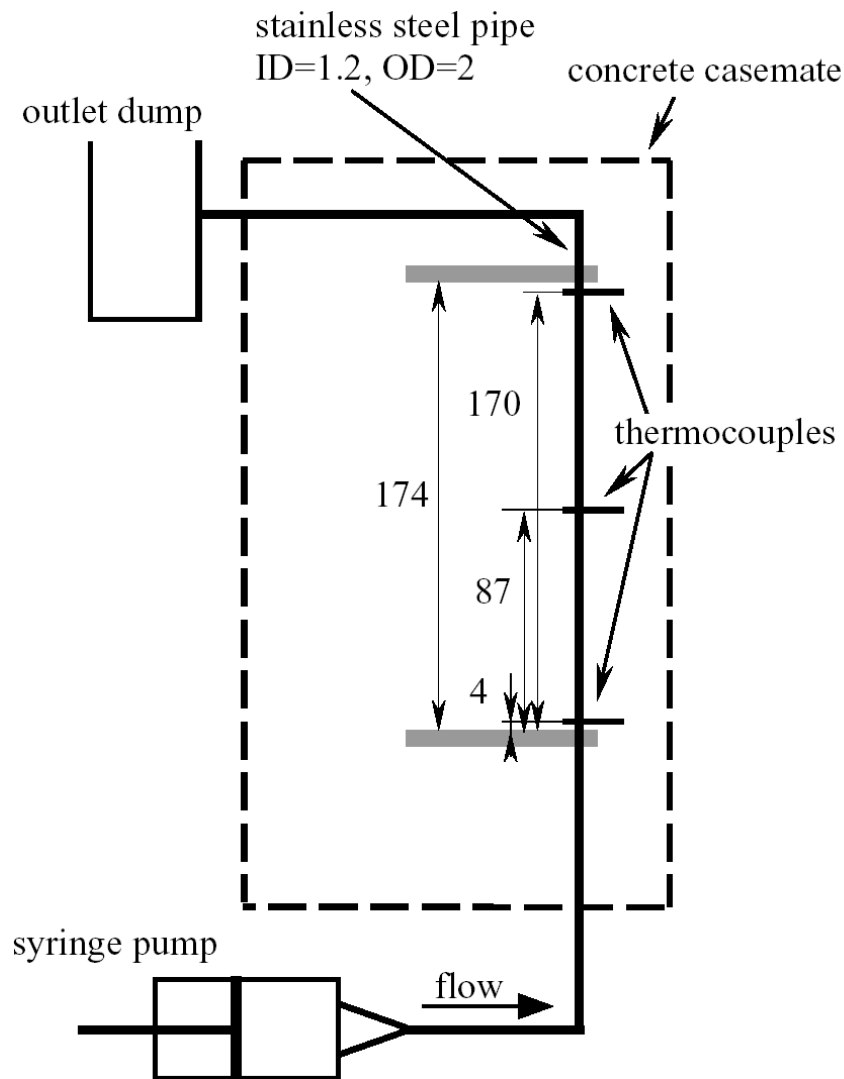


Figure 6.18: Flow apparatus

rate of the camera, only a small region of interest of the chip of 32 lines was read out. Different exposure times and frame rates have been applied:

exposure time [ms]	1	5	10
frame rate [Hz]	154	95	64

The experiments were carried out for different settings of heating power and mass flow. The variation of these settings had a strong effect on the behavior of the boiling. We observed stable boiling as well as chaotic behavior. Sometimes the liquid was superheated and evaporated then spontaneously. All the radiographies were correlated with the temperature measurement.

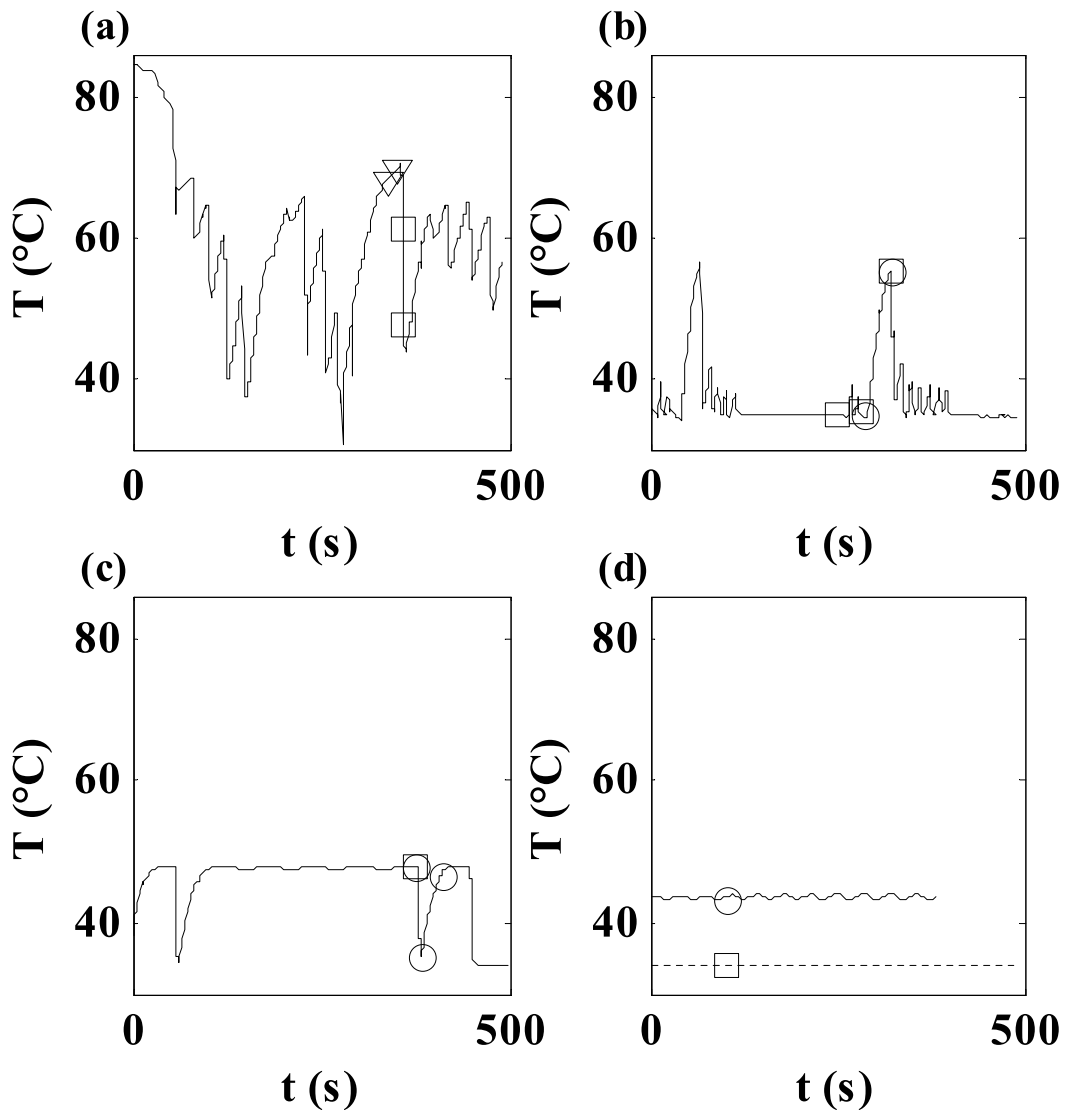


Figure 6.19: Temperature variations for the center thermocouple at various flow rates: a) $1.5 \text{ kg/m}^2 \text{ s}$ - superheated gas with intermittent liquid slugs; b) $6.0 \text{ kg/m}^2 \text{ s}$ - saturated boiling with intermittent liquid superheat; c) $15.4 \text{ kg/m}^2 \text{ s}$ - liquid superheat with intermittent boiling; d) $21.4 \text{ kg/m}^2 \text{ s}$ - both liquid superheat and saturated boiling.

Fig.6.19 shows the temperature measurements of four typical results. Fig. 6.20 and 6.21 display the radiographic images from the time steps marked in Fig. 6.19.

This preliminary test on only one tube demonstrated the capability of high-speed neutron radiography. In future projects we will investigate larger systems of communicating channels. However, for such experiments a new high-speed camera has to be acquired in order to record the process with high speed at full field of view.

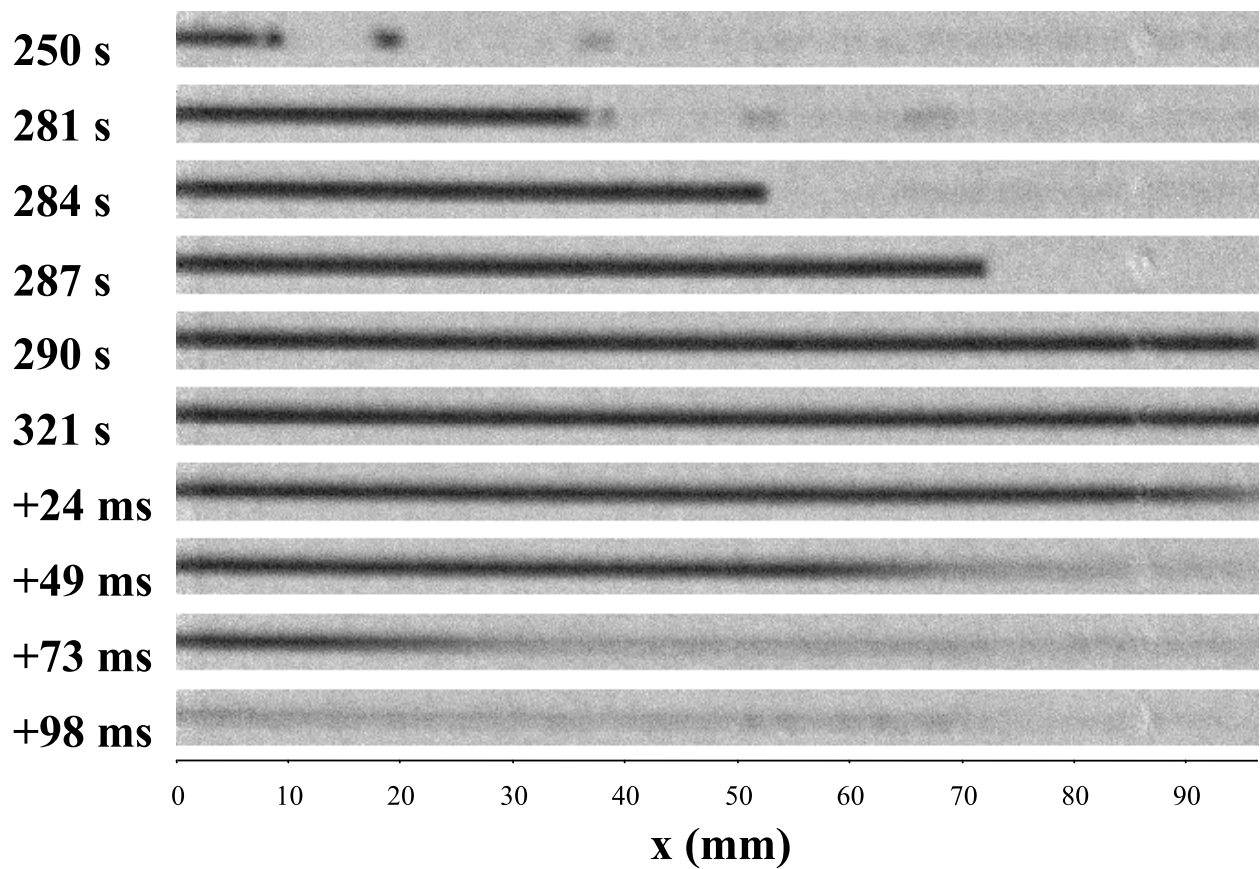


Figure 6.20: Images from the instants marked with circles in Fig. 6.19b: slow fill followed by rapid vaporization.

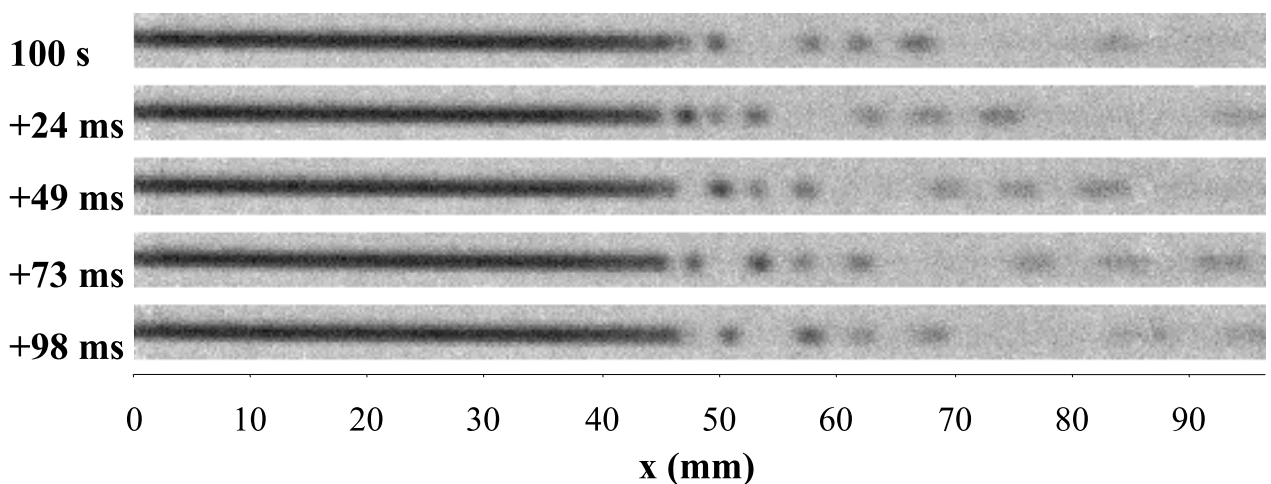


Figure 6.21: Images corresponding to the square in Fig. 6.19d: steady boiling.

6.2.3 $^3\text{He}/^4\text{He}$ phase transition

The dynamic radiography on the phase transition of ^3He and ^4He is an example for the capability of neutrons to differentiate between isotopes of the same element. In this experiment the dissolution of ^3He in ^4He in a cryostat was visualized. The motivation of the experiment was to complete the understanding of how the cryostat works. The experiment was carried out in collaboration with the ILL's cryogenic group. A new experiment which investigates the phase transition and diffusion coefficients quantitatively is in preparation.

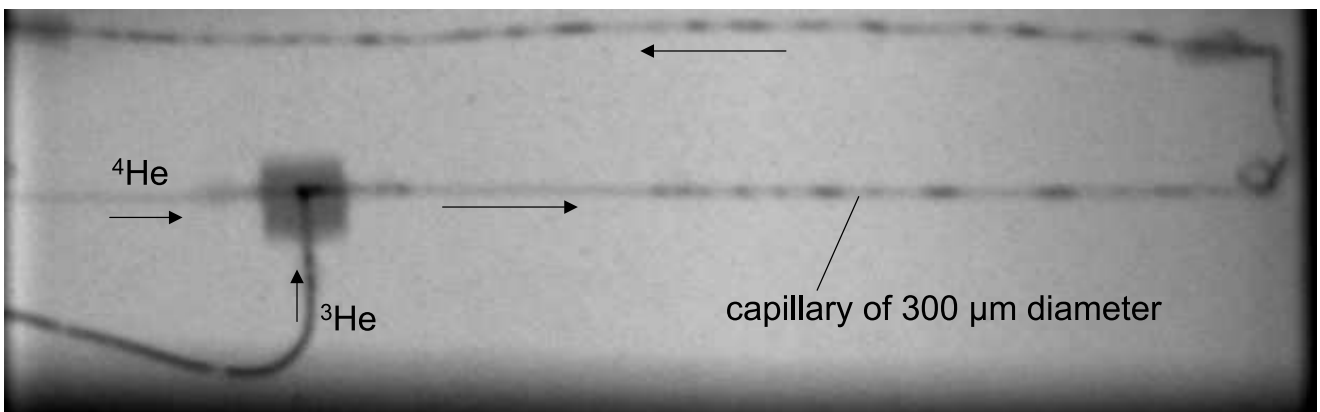


Figure 6.22: *Capillaries in a cryostat*

Fig. 6.22 shows the capillary system of the cryostat. The low image quality has two reasons: First the capillaries have an diameter of $300\ \mu\text{m}$, which is not far from the spatial resolution of NEUTROGRAPH. Second we had no possibilities to acquire an open beam image for the normalization of the images. However for the differentiation of the two isotopes the image quality is more than sufficient.

The helium was cooled down and liquified. The dark grey values represent the ^3He isotope, which has a high attenuation cross section of 5339 barns. The ^4He with it's low attenuation cross section of 1.34 barns is represented by light grey values.

6.3 Static Tomography - More Experiments

6.3.1 Antarctic Fossils

In Antarctica one can find rock specimen containing plant fossils. They originate from a time when Antarctica was covered with woods instead of glaciers. However, since Antarctica is covered by thick layers of ice, only a few fossils are found, which makes them very precious for science. The standard method of investigating the fossils inside the rock samples by cutting the specimen into slices destroys these samples. A non-destructive testing method is required. Neutrons have the capability of penetrating even thick objects, but the contrast below one percent due to the differences in density and material composition of the stone matrix and the fossils, is extremely low. In order to resolve the variances, sufficiently statistics have to be collected. The high intensity beam of NEUTROGRAPH helps to do this in a reasonable time. In collaboration with the Leeds University [ULeeds], we investigated samples which have an age of 50 - 56 million years. In order to visualize the small material differences, we acquired 800 projections, where each projection was the sum of 100 single exposures. After each set of 20 projections, the sample was moved out of the beam and open beam images were recorded. Then the tomography continued. With this procedure and a frame rate of about 12 *Hz*, the time in-between two open beam images was only about 3 *min*. This minimized the effect of scintillator degradation and made a very precise interpolation possible.

Fig. 6.23 shows the reconstructed volume with the fossil in green and the stone as transparent grey object. The fossil is a piece of monkey-puzzle tree (*Araucaria araucana*). It features a small branch and leaves. This kind of tree exists also today. Fig. 6.24 shows a photograph of a contemporary tree.



Figure 6.23: *Fossil of a monkey-puzzle tree inside a rock sample*



Figure 6.24: *Branch of a contemporary monkey-puzzle tree*

7. Conclusion and Outlook

In the framework of this thesis, the neutron imaging facility NEUTROGRAPH was put into operation, its properties were investigated and it was developed to a powerful tool for neutron imaging. The development has been done on the detection system, the measuring procedures and the evaluation methods in order to optimize the image quality. Also the sample environment and the infrastructure of the experimental zone have been improved for a higher flexibility in the experimental work.

With its imaging properties, NEUTROGRAPH belongs now to the leading instruments in this field of research and in the case of time resolution it is unrivalled. It will hold this position also in the near future since all existing neutron sources and the neutron sources under construction can not provide comparable parameters.

During the last years many experiments have been done at NEUTROGRAPH for the first time in world, e.g. the fuel injection and the tomography of a friction stir weld. With the broad spectrum of projects, neutron imaging techniques have now been introduced to new fields of applications, where new nondestructive testing methods are urgently needed.

The development work on the facility will continue during the next years. In the case of the detector system new specialized cameras will complement the existing set-up. One camera of higher sensitivity for a high contrast visualization of small material variances and one high-speed camera, which is dedicated to speed up the dynamic tomography and to minimize the interframing time in a realtime radiography. These modifications will improve the quality of many of the experiments (e.g. high contrast tomography in archaeology and material sciences) and other applications will become realizable only then (e.g. dynamic tomography of transport mechanisms in channel systems with a time resolution of 1 s, realtime radiography of impacts in energy absorbers from the automotive industry with 100 μm time resolution).

A further modification is the installation of an optional pair of soller collimators. A new beam divergence of $L/D = 660$ is projected. With the new collimation either the spatial resolution can be increased or the effect of scattered neutrons be decreased by enlarging the distance in-between the sample and the detector. It will put NEUTROGRAPH among the top-ranking

7 Conclusion and Outlook

instruments also in this domain.

Bibliography

- [ANLW] George R. Imel, ASTM E7.05.04 "Educational/Editorial Activities", Argonne National Laboratory - West, P.O. Box 2528, Idaho Falls, Idaho 83403-2528, USA, <http://anlw.inel.gov/nr/>
- [Antares] Advanced Neutron Tomography and Radiography Experimental System, <http://www1.physik.tu-muenchen.de/antares>
- [AST] Applied Scintillation Technologies, <http://www.appscintech.com>
- [BMW] BMW, <http://www.bmw.com>
- [BOSCH] Robert Bosch GmbH, <http://www.bosch.com>
- [BrTa04] D. Brutin, L. Tadriss, *Pressure drop and heat transfer analysis of flow boiling in a minichannel: influence of the inlet condition on two-phase flow stability*, International Journal of Heat and Mass Transfer, 2004, Vol. 47(10-11), pp. 2365-2377
- [CEA] Commissariat à l'Énergie Atomique, 17 Rue des Martyrs, 38054 Grenoble, France
- [Eng04] M. Engelhardt, *Imaging of dynamic processes with a time scale of microseconds at a thermal neutron beam*, diploma thesis, Technical University Munich, 2004
- [Ferg03] T. Ferger, *Aufbau einer dynamischen Radiografie- und Tomografiestation mit thermischen Neutronen*, diploma thesis, Heidelberg University, 2003
- [Gild03] A.E. Gildemeister, *Fast dynamic radiography at a high-lux thermal neutron beam*, diploma thesis, Heidelberg University, 2003
- [Her80] G.T. Herman, *Image Reconstruction From Projections, The Fundamentals of Computerized Tomography*, Academic Press, 1980
- [HMI] Dr. Nikolay Kardjilov, Hahn-Meitner-Institut Berlin, Abteilung Werkstoffe (SF3), Glienicke Str. 100, D-14109 Berlin, http://www.hmi.de/bereiche/SF/SF3/methods/ntomo/index_en.html

- [Hug57] D.J. Hughes, *Neutron Cross Sections*, Pergamon Press, 1957
- [Isel] ISELautomation KG, <http://www.isel.com>
- [Isis] ISIS Pulsed Neutron & Muon Source, <http://www.isis.rl.ac.uk>
- [Kob90] H. Kobayashi, H. Wakao, *Accurate measurement of L, D and L/D for divergent Collimators*, Neutron Radiography, Proc. 3rd World Conf. Neutron Radiography Osaka 1989, printed 1990, pp. 889-892
- [Micos] Micos GmbH, <http://www.micos.ws>
- [NEUTRA] Neutron Transmission Radiography, <http://neutra.web.psi.ch>
- [NI] National Instruments, <http://www.ni.com>
- [Os04] K.M. Oseen-Senda, F. Lundell, A. Hillenbach, J. Pauchet, *Visualisation of Low Heat and Mass Flux Boiling in a Small Metal Pipe Using Neutron Radiography*, Proc. ICMM2004, Rochester (New York), 2004
- [Pel03] Y. Peles, *Two-phase boiling flow in microchannels - instabilities issues and flow regime mapping*, ASME First International Conference on Microchannels and Minichannels, 2003, pp. 559-566
- [PCO] PCO Computer Optics GmbH, Donaupark 11, 93309 Kelheim, Germany, <http://www.pco.de>
- [Schill99] B. Schillinger, *Neue Entwicklungen zu Radiographie und Tomographie mit thermischen Neutronen und zu deren routinemäßigem Einsatz*, dissertation, TU Munich, 1999, Mensch & Buch Verlag, Berlin
- [Schneid01] M. Schneider, *Studies for neutron tomography at the Institut Laue-Langevin*, diploma thesis, Heidelberg University, 2001
- [SigmaA] Sigma Aldrich, <http://www.sigmaaldrich.com>
- [UGhent] Ghent University, <http://www.ugent.be>
- [ULeeds] School of Earth and Environment, University of Leeds, Leeds LS2 9JT, UK
- [WenKen04] D.S. Wen, D.B.R. Kenning, *Two-phase pressure drop of water during flow boiling in a vertical narrow channel*, Experimental Thermal and Fluid Science, 2004, Vol. 28(2-3), pp. 131-138

[Will] Willecke Hebe- und Fördergeräte GmbH, <http://www.willecke.de>

[WuCh03] H.Y. Wu, P. Cheng, *Liquid/Two-Phase/Vapor alternating flow during boiling in microchannels at high heat flux*, Int. Communications in Heat and Mass Transfer, 2003, Vol. 30(3), pp. 295-302

[Yen03] T-H. Yen, N. Kasagi, Y. Suzuki, *Forced convective boiling heat transfer in microtubes at low mass and heat fluxes*, Int. J. Multiph Flow, 2003, Vol. 29(12), pp.1771-1792

8. Acknowledgements

I am very grateful to the people who supported me and my work on this thesis. In particular:

- My supervisors Prof. Dr. Hartmut Abele and Dr. Roland Gähler for their support and encouragement.
- All the members and former members of the NEUTROGRAPH-team for the fruitful collaboration: Hendrik Ballhausen, Martin Engelhardt, Arnd Gildemeister, Benjamin Lamboul, Thomas Ferger, Michael Schneider.
- The teams from abroad I collaborated with: ANTARES [Antares] (Dr. B. Schillinger, J. Brunner), NEUTRA [NEUTRA] (Dr. E. Lehmann, Gabriel Frei), CEA [CEA] (K. Oseen-Senda, F. Lundell, C. Gondrand), Prof. J. Francis, Prof. R. Cywinski, R. Stephens, M. Dawson from the Leeds University [ULeeds], Dr. B. Masschaele and M. Dierick from Ghent University [UGhent], ISIS [Isis] Dr. D. Visser and many others.
- The staff of the Institut Laue-Langevin, in particular: P. Thomas, F. Fihman, C. Brisse, S. Million.

Special thanks to my family for all their encouragement and patience.

9. Declaration

I

confirm that this work submitted for assessment is my own and expressed in my own words. Any use made within it of works of other authors in any form (e.g. ideas, figures, text, tables) are properly acknowledged at their point of use. A list of the references employed is included.

Signed

Date

